INFORMATION TO USERS

The most advanced technology has been used to photograph and reproduce this manuscript from the microfilm master. UMI films the text directly from the original or copy submitted. Thus, some thesis and dissertation copies are in typewriter face, while others may be from any type of computer printer.

The quality of this reproduction is dependent upon the quality of the copy submitted. Broken or indistinct print, colored or poor quality illustrations and photographs, print bleedthrough, substandard margins, and improper alignment can adversely affect reproduction.

In the unlikely event that the author did not send UMI a complete manuscript and there are missing pages, these will be noted. Also, if unauthorized copyright material had to be removed, a note will indicate the deletion.

Oversize materials (e.g., maps, drawings, charts) are reproduced by sectioning the original, beginning at the upper left-hand corner and continuing from left to right in equal sections with small overlaps. Each original is also photographed in one exposure and is included in reduced form at the back of the book.

Photographs included in the original manuscript have been reproduced xerographically in this copy. Higher quality 6" x 9" black and white photographic prints are available for any photographs or illustrations appearing in this copy for an additional charge. Contact UMI directly to order.

U·M·I

University Microfilms International
A Bell & Howell Information Company
300 North Zeeb Road. Ann Arbor. MI 48106-1346 USA
313 761-4700 800 521-0600

Order Number 9029940

Sputter synthesis of RE-TM 2–17 type magnetic films with strong alignment of easy axes of grains

Hedge, Hari S., Ph.D.

City University of New York, 1990

U·M·I
300 N. Zeeb Rd.
Ann Arbor, MI 48106

A

SPUTTER SYNTHESIS OF RE-TM 2-17 TYPE MAGNETIC FILMS WITH STRONG ALIGNMENT OF EASY AXES OF GRAINS

by

HARI S. HEGDE

A dissertation submitted to the Graduate Faculty in Physics in partial fulfillment of the requirements for the degree of Doctor of Philosophy, The City University of New York

1990

This manuscript has been read and accepted for the Graduate Faculty in Physics in satisfaction of the dissertation requirement for the degree of Doctor of Philosophy.

April 19, 1990
date

Fred J. Cadieu
Chair of Examining Committee

April 24, 1990
date

Executive Officer

Prof. F.J.Cadieu

Prof. J.Neuberger

Prof. M.P.Sarachik

Dr. E.Potenziani

Dr. S.M.Rossnagel

Supervisory Committee

The City University of New York

ACKNOWLEDGEMENTS

I am grateful to my mentor Prof. Fred J. Cadieu for his support and encouragement throughout the course of this work. Without his gentle prodding this thesis work would have been impossible. His work ethics and attention to details have made an indelible impression on me. I am thankful to former Research Associates Dr. Tak D. Cheung and Dr. Lee Wickramasekara who helped me through numerous seemingly insoluble problems and difficult situations. I am also thankful to former Research Associates Dr. N. C. Liu and Dr. X. R. Qian and to my fellow researchers Mr. K. Chen and Mr. N. Kamprath and all the other members of our research group.

I am thankful to all the members of the Queens College faculty, in particular to Prof. Jacob Neuberger for the encouragement he gave me during the last five years. I would also like to thank the department staff, especially the secretaries, Mrs. Shirley Allen and Mrs. Susan Wasserman for their wholehearted assistance. I feel deeply indebted to Mr. Paul Schaedler and Mr. Grigory German for their timely and thoroughly professional technical help. I am grateful to my friend and former colleague Mr. Dimitrios Thomokos for the commendable work he did in digital electronics and computer software in our laboratory and thus making data collection and analysis that much easier and less time consuming.

I am grateful to my lovely wife Vijaya for the patience she has shown and for having stood by me through difficult times and to my charming little daughter Nischit for understanding that "Dad is busy". I am also thankful to my friends Mr. Charles McMahon and Mr. AlKarim Gangji for all the support they have shown.

I would like to thank Prof. J. Neuberger, Prof. M. P. Sarachik, Dr. E. Potenziani and Dr. S. M. Rossnagel for having served in my thesis Supervisory Committee. In particular, I would like to acknowledge the invaluable suggestions made by Dr. Rossnagel on the thermalization calculations.

The part of the thesis work involving the systematic study of the sputter synthesis and characterization of the 2-17 type permanent magnet thick and thin films was supported by grants to Prof. Cadieu from RADC/EEAC, Deputy for Electronic Tech., Hanscom AFB, MA-01731 (Contract No.F19628-88-K-0021). The thermalization modeling part of the thesis work was supported by grants to Prof. Cadieu from Dept. of Energy (Grant No. DE-FG02-86ER45265)

TABLE OF CONTENTS

LIST OF TABLES

LIST OF FIGURES

CHAPTER 1

INTRODUCTION

Extensive work on bulk Rare Earth-Transition Metal alloys carried out by several groups of researchers since the discovery of extremely high uniaxial magnetocrystalline anisotropy of YCo_5 by Hoffer and Strnat(1) in 1966 has resulted in the discovery of several new classes of high performance permanent magnets of Light RE-TM(Fe,Co,Ni), in the form of bulk magnets. The best known among these are the Samarium-Cobalt based hexagonal 1-5 and 2-17 compounds which are crystallographically related and the Iron based tetragonal $Nd_2Fe_{14}B$. In the bulk fabrication of these magnets, several metallurgical methods such as sintering, hot isostatic pressing, melt spinning etc. have been well established(2). These methods allow the fabrication of the magnets in the form of dense aggregates of single domain grains with good alignment of their magnetic easy axes. As a result, the hysteresis loops of these magnets are flat topped and their energy products approach the theoretical values.

Prof.Cadieu and coworkers have synthesized several types of these RE-TM permanent magnets in thin film form, through RF glow discharge sputter deposition on single crystal and polycrystalline Al_2O_3 substrates. Two distinct methods of sputter deposition were employed(3): (1) Subsequent Crystallization: Magnet material was first deposited in amorphous form and subsequently crystallized through proper heat treatment. (2) Direct Crystallization: Magnet material was crystallized as it was being deposited, by carrying out the deposition on a properly preheated substrate. In magnet films of $SmCo_5$(4) and Ti stabilized SmFe(5),(54), synthesis by the first method allowed achieving record high values of coercivities. This was attributed to the formation of the polycrystalline film in defect free, fine grain form. However, this method was unsuccessful in achieving strong alignment of the easy axes of the crystallites. As a result, the hysteresis loop squareness was much lower than unity and the energy products were significantly lower than the theoretical values. The second method, direct crystallization, was successful in achieving larger values of loop squareness and energy products when the ferromagnetic ordering temperature of the film material was higher than the deposition temperature. So, in spite of the extremely high room temperature energy products exhibited by $Nd_2Fe_{14}B$ in bulk form, it showed only moderate values in film form since it was not possible to crystallize the film below its Curie Point (T_C=600K). However, in all cases of direct crystallization, it was necessary that the sputtering be carried out at high pressures of the sputtering gas in "thermalized" mode(11). The thermalization of the sputtered atoms as they arrive at the substrate, was necessary to preserve loop squareness and to avoid drastic reductions in coercivity values, possibly due to high concentration of reversed domain nucleation sites arising from bombardment by energetic particles. The energy products in films of $SmCo_5$ and $Sm_2(CoFeCuZr)_{17}$, synthesized by this method(3) compared favorably with those of their bulk counterparts(6). That the 2-17 type film magnets exhibited energy products in excess of 20MGOe and that their ferromagnetic ordering temperatures were very high, make these films most suited for magnetic bias circuits with electronic applications as well as in fine scale geometry permanent magnet structures(7).

The early syntheses of these film magnets were carried out in Argon. In the direct crystallization of these film magnets, since the thermalization of the sputtered atoms plays an important role, and since the RE and TM components differ widely in atomic masses and radii, the investigation of sputter synthesis of these RE-TM magnet films using different sputtering gas species seemed necessary. Such an investigation has been attempted by this thesis work. For sputtering using different gas species, the rate of energy loss of the RE and TM components of sputtered atoms and so their thermalization, and the loss of flux of one component relative to the other due to the differences in their masses and atomic radii, would make the film properties differ accordingly. This thesis work has attempted a systematic study of the film property variation with sputtering gas species and other sputter deposition conditions.

In the earlier works, cosputtering was used as a means of gaining control over film composition. However, cosputtering causes the film composition to be inhomogeneous which is a disadvantage under most circumstances and it is also considerably more time consuming in terms of target preparation. For this reason, this thesis work has explored the sputter synthesis of film magnets from bulk target magnets with homogeneous composition. Throughout this work, the 2-17 type film magnets were sputter synthesized from commercially available TDK $Sm_2(CoFeCuZr)_{17}$ bulk target magnets. This bulk target exhibited a $(BH)_{max}$ of about 27MGOe and had a Sm content of about 14.2%. It was found that the Sm content of the film magnet could be varied from 12 atomic percent to at least 18 atomic percent by varying the substrate preheating temperature and sputtering gas species and pressures. This kind of elemental composition change can be expected for films of some other RE-TM systems too.

Through optimized thermalized sputtering very strong crystal texturing was achieved, wherein all the crystallites in the film had their c-axes, that is, their magnetic easy axes, aligned in the film plane(9). This was indicated by a very narrow hysteresis loop measured perpendicular to the film plane and was confirmed by the X-Ray diffraction trace which showed a total absence of reflections from crystallographic planes with nonzero l indices. To a lesser extent, anisotropy within the film plane was also achieved by the application of a magnetic field along a particular direction in the substrate plane. The effect of this H_s was quite significant in films synthesized under optimum conditions of thermalized sputtering. For such films, the energy products for magnetization along H_s was higher than that for magnetization within the film plane in the perpendicular direction, by up to 20%. Along H_s, loop squareness ($4\pi Mr/4\pi Ms$) of up to 0.75 and an estimated anisotropy energy, for magnetization along H_s versus magnetization perpendicular to film plane, of 5×10^7 erg/cc were thus achieved. The sputtering parameters were also adjusted to make the films to be sufficiently space filling to the extent that their densities were around 93.5% of their X-Ray density. Thermalized sputtering using 50%Ar50%Xe allowed us achieve sufficient anisotropy along the H_s for Sm contents lesser than in films synthesized using Ar that showed similar anisotropies. The remanent induction increases resulting from the decrease of Sm content caused the energy products of these films to be higher than those of films synthesized using Ar by up to 20%. For films synthesized through optimized thermalized sputtering in 50%Ar50%Xe, the $(BH)_{max}$ were in the vicinity of 20MGOe.

An attempt has been made to explain some of the observed effects, such as crystal texturing, loop squareness and coercivity variation, in terms of a model dealing with the sputtered atom kinematics(10).

Originally, Prof.Cadieu had used such a model to explain the observed high T_c of superconducting Nb_3Ge films, synthesized through RF glow discharge sputter deposition(11). The model calculates the change in the energy of the sputtered atoms as they undergo collisions with the sputtering gas neutrals and ultimately arrive at the substrate. The calculations of this model differ from the original model of Prof.Cadieu, in that, it uses an energy dependent energy transfer cross-section. In addition, this model calculates the change in the energy spectrum of the sputtered atoms as they traverse from the target to the substrate. The observed changes in the properties of the films have been correlated to the sputter deposition conditions through this model. The model confirms the experimental finding that thermalized sputtering can be carried out either at 60μ of 50%Ar50%Xe or at 130μ of Ar. According to the model, at these pressures, atoms sputter ejected with even 100eV of energy would have energies around 1eV as they arrive at the substrate. This is in conformity with the experimental evidence that such films showed no indication of disruptions caused by energetic massive particles that result in nonlinear demagnetization behavior and that in such films the c-axes of the grains were all aligned in the film plane..

CHAPTER 2

RARE EARTH - TRANSITION METAL INTERMETALLIC COMPOUNDS

2.1 Introduction

A great many number of stable RE-TM binary compound systems which contain several intermetallic compounds, where each of which is characterized by a different composition and crystal structure, are known to exist(12). This is attributable to vast differences in two important physical properties of the RE's and the TM's. The large differences between the electronegativities of REs and other metals makes it likely that the compound exists and the large differences between the metallic radii of the REs and TMs makes several atomic arrangements of sufficiently high space filling possible. For TM rich RE-TM compounds, in cases where TM is represented by Fe, Co or Ni, magnetic coupling between the magnetic moments is likely to exist. Neutron diffraction experiments and magnetic measurements have shown that the TM moments are oriented antiparallel to the RE spin moment. Unlike in the transition metals, in the case of rare earths, the spatial extent of the incomplete shell (4f) electron wave functions is quite small, making the crystal field splitting small compared to the spin-orbit interaction. So, the total angular momentum J is a good quantum number(13). Since J = L-S for light REs and J = L+S for heavy REs, one can expect ferromagnetism in the case of compounds involving light REs and antiferromagnetism in the case of compounds involving heavy RE's.

2.2 Crystal Structures of RE-TM Compounds

A survey of the various structure types observed in binary RE-TM compounds is given in table 1. A majority of the crystal types listed are related and are derived from the hexagonal lattice of the $CaCu_5$ type(14),(15). The unit cell of the $CaCu_5$ type is given in the extreme left side of Fig.2. In the lowest layer both RE and TM atoms are found whereas in the next layer only the TM atoms are found. The RE_2TM_{17} structure is obtained by the ordered substitution of a third of the RE atoms by a pair of TM atoms("dumb-bell" atoms). As a result, the new basal plane lattice parameter a' becomes $\sqrt{3}$ times basal plane lattice parameter a of the 1-5 compound. When the substitutions proceed according to the sequence ababab, the Th_2Ni_{17} type hexagonal structure with the c-axis lattice parameter c' equal to twice the lattice parameter of the 1-5 compound would result. If on the other hand, the substitutions proceed according to the sequence abcabc, the rhombohedral Th_2Zn_{17} type structure with the c-axis lattice parameter c' being equal to 3 times the c-axis lattice parameter of the 1-5 compound would result. These two stacking arrangements along the c-axis are schematically shown in the lower part of Fig.1. The simplified relation between the 1-5 and hexagonal form of 2-17 structures can be given as follows:

3*(1-5) = 3-15 = (2-1)-15 ≡ 2-2-15 = 2-(2-15) = 2-17.

The 2-17 unit cells of the Hexagonal and Rhombohedral types are shown respectively in the center and extreme left of Fig.2.

As is schematically indicated in the upper part of Fig.1, the structures of compounds of the type 2-7, 1-3 and 1-2 are also derived from the structure of the 1-5 compound. The 1-3 structure is obtained by the substitution of one of the two RE atoms in the basal plane of every two 1-5 unit cells and a layer shift followed by a minor rearrangement of the atoms. This leads to a hexagonal unit cell with an unchanged basal plane lattice parameter, and c-axis lattice parameter which is four times as long. As in the 2-17 compounds, a rhombohedral form is also possible. The relation between 1-5 and hexagonal form of 1-3 compounds can be summarized as follows:

2*(1-5) = 2-10 = 2-(1-9) ≡ 2-1-9 = (2-1)-9 = 3*(1-3) ≡ 1-3.

In all these compounds, the difference in the stability between the hexagonal and rhombohedral forms is believed to be very small. In the case of some 2-17 compounds, where RE = Sm or Gd, the substitutions at the dumb-bell sites can proceed without it being ordered and one obtains the disordered 2-17 compound of the $TbCu_7$ type. As a result, in these RE-TM systems, broad homogeneity ranges are observed on the RE side of 2-17 compound and the TM side of 1-5 compound(16).

2.3 Magnetism in RE-TM Systems

2.3.1 Magnetism in RE Metals

In the RE's, since the incomplete 4f shell electrons are not entirely shielded by the $5s^2 5p^6$ shells, they suffer some crystal field effects which results in the partial or complete lifting of the (2J+1) fold degeneracy of the ground state. In the case of Pr where the lifting of degeneracy is complete, no ordering of spins is seen at any temperatures. In the case of heavy RE's, where the 4f's are less extended, the crystalline anisotropy is weak leading to a variety of spin structures like helices, cones etc. Of all the RE's, only Gd exhibits a ferromagnetic ordering temperature higher than room temperature. Because of the highly localized nature of the 4f's, the magnetic interaction is the indirect RKKY (Rudderman-Kittel-Kasuya-Yosida)(17) type. According to the RKKY type calculations, the conduction electron polarization due to the localized 4f's would be proportional to,

$(\sin 2k_f r - 2k_f r \cos 2k_f r) / (k_f r)^4$.

This function is spatially nonuniform. For each localized moment, the net interaction with the other moments is obtained by summing the contributions from the conduction electron spin polarization produced at that particular site by all other moments. The sign of this sum would determine the sense of the 4f spin moment coupling. Thus, the magnetic coupling would be dependant on the structure as well as the on the density of the conduction electrons. Generally, the strength of these indirect couplings are very weak leading to very low ordering temperatures.

2.3.2 The Exchange Interaction in Systems Containing 3d-electrons:

Magnetic interactions in RE-TM systems comprise of the following three types:

(1) R-R interaction
(2) R-M interaction
(3) M-M interaction:

(1) R-R interaction:

An impression of the strength of the R-R interaction is obtained by the very low ordering temperatures in RE-TM compounds in which the TM is nonmagnetic. The R-R interaction is the weakest of the three types of interaction mentioned. In fact, it is similar to the indirect RKKY interaction in RE metals, with the difference that due to the diluted concentrations of RE's in TM rich RE-TM's the coupling could be even weaker. For this reason, there have been arguments made, wherein the interaction proceeds through the polarization of the 5d electrons.

(2) R-M interaction:

Through Neutron diffraction and thermomagnetic measurements, it has been found that the 3d-4f spin coupling is antiparallel(18). Several schemes have been proposed to explain the observed coupling(19),(20). If the RE-TM interaction were to be of the RKKY type involving the 4f-s and 3d-s, the net coupling would be strongly influenced by the crystal structure and conduction electron concentration. Since this would contradict the observed coupling which is always antiparallel, it has been argued that 4f-3d coupling proceeds through polarization of the RE 5d electrons(21).

(3) M-M interaction:

As result of the substantially larger spatial extent of the 3d electrons of the TM's, the M-M interaction is the strongest of the above mentioned three interactions. M-M interaction can be studied in compounds where the RE component is nonmagnetic as when the RE is represented by La or Y. Magnetic properties of these compounds are presented in fig 3. As a result of the close crystallographic relationships between the different compounds, their magnetic properties show smooth variations. It is seen that the magnetic moment monotonically decreases with increasing dilution and in cases of Ni and Co the T_c values decrease too, whereas T_c of Fe increases with dilution. While most of the observed properties have been explained through the itinerant electron model, some of the properties have been explained through localized electron model(22). The sudden loss of net magnetic moment in RNi_2 compounds and the strong drop in the RCo_2 and RFe_2 compounds have been attributed to reduction in the effective Coulomb repulsion between 3d electron due to considerable electron transfer from the RE's to the TM's. However, there has been no satisfactory explanation for the anomalous behavior of T_c of RE-Fe compounds.

It follows from the above discussion that any permanent magnet of the RE-TM type should be TM rich and should have either Fe or Co as the major TM component.

2.4 Anisotropy in RE-TM Compounds

For uniaxial systems such as hexagonal and tetragonal, the magnetocrystalline anisotropy energy can be given by

$E = K_1\sin^2\theta+K_2\sin^4\theta$,

where θ is the angle between the magnetization vector and the c-axis. The easy direction of magnetization as obtained by minimizing anisotropy energy, E, with respect to angle θ(23). The anisotropy in

RE-TM systems can be thought of as the result of the sum of the contributions from the RE and TM sublattices. The contribution from the RE sublattice in the form of single ion anisotropy of the RE's would be dominant at lower temperatures. At temperatures high compared to the overall crystal field splitting, the single ion anisotropy of the RE's is relatively unimportant and the contribution of the TM sublattice would be dominant(24). These temperature dependent sublattice dominations can lead to strong temperature dependance of the anisotropy constants K_1 and K_2 which could result in anisotropy changing from easy axis to easy basal plane or easy cone. This kind of temperature dependence is seen in $NdCo_5$(25) where the high temperature easy axis anisotropy changes into easy basal plane anisotropy at lower temperatures. In $PrCo_5$(26), with lowering of the temperature easy axis anisotropy changes into easy cone anisotropy.

In 1-5 compounds, even when RE is represented by nonmagnetic elements such as Y, La or Ce, it was found that if the TM is represented by Co, extremely high uniaxial anisotropies are obtained, pointing to the very strong contribution of the Co sublattice to the total magnetocrystalline anisotropy even in compounds where the RE component is moment bearing. The strong contribution of the RE sublattice to the total magnetocrystalline anisotropy can be understood by the study of RE_2-Co_{17} compounds. In these systems, when RE was represented by Y, easy basal plane anisotropy was observed(17) and when RE was represented by Sm, easy axis anisotropy was observed. From this, we can conclude that Sm sublattice is the major contributor to the observed extreme anisotropies in $SmCo_5$ and Sm_2Co_{17} compounds. One can also conclude that the dumb-bell Co atoms in the 2-17 compound weaken uniaxial anisotropy. In $SmCo_5$ anisotropy fields up to 400KOe were observed whereas for Sm_2Co_{17} only 65KOe anisotropy fields were observed.

2.5 Effect of Substitutions on 2-17 Anisotropy and Magnetization

Since the magnetization is primarily determined by the TM sublattice, TM richer compounds are required to be able to obtain higher remanent induction values. Though an increased magnetization is observed in Sm_2Co_{17}, the drastically reduced anisotropy energy renders it unsuitable to be a permanent magnet. Efforts directed at preferential substitution of the dumb-bell Co atoms with other TM atoms, resulted in increased anisotropy in the compound. It was found that this effect varied from element to element as follows: Zr > V > Hf > Ti > Cr > Mn > Fe. The following explanation was given for this increase in the anisotropy: For Co, to be able to preserve easy axis anisotropy, a certain minimum Co-Co spacing is required which is unavailable at the dumb-bell site. So, preferential replacement of dumb-bell Co atoms results in increased anisotropy. It was also found that substitution of some Co atoms with Fe leads to substantial increases in the magnetization value. For nonmagnetic RE's, such as Y and Ce substitution of 5% to 45% of all the Co atoms with Fe was possible such that the easy basal plane anisotropy of the pure RE-Co binary compound changes into easy axis anisotropy in the ternary compound(28). The increased magnetization was easily explained with the help of the rigid band approximation.

Even with improved anisotropy fields with preferential substitutions, in a single phase 2-17 compound, it was not possible to achieve high intrinsic coercive force. It was found that with some addition of Cu, from a homogenized single phase precursor of the $TbCu_7$ type, a majority phase containing hexagonal and rhombohedral 2-17 phases and a Cu rich 1-5 phase can be precipitated. The Cu rich 1-5 phase facilitates increases in the intrinsic coercivities by providing attractive domain wall pinning sites(29). With these improvements, 2-17 type permanent magnets with room temperature $(BH)_{max}$ in excess of 30MGOe were produced(57),(58). The composition of the TDK 2-17 type target used for the deposition of our 2-17 magnetic films is given in table 6.

CHAPTER 3

EXPERIMENT

3.1 Synthesis of Film

The magnetic films were synthesized by RF glow discharge sputter deposition from a TDK 2-17 type bulk target. RF Sputter deposition is extensively used in the synthesis of semiconductor, superconductor, insulating as well as metallic films(30),(31). RF sputter deposition has distinct advantages over other methods of film synthesis, in terms of control over depositing atom energy, crystal texturing, film composition, etc.. In addition, it provides a cleaner environ and offers the capability to synthesize conducting as well as insulating films. In Fig.4, a schematic of the RF glow discharge circuit is given. The depositions of our films were carried out in a stainless steel high vacuum chamber. The gas species used in the sputtering were Ar,Xe and an admixture of 50%Ar and 50%Xe. The base pressure in the sputtering chamber was normally in the low 10^{-7} Torr. The base pressure was brought down to this range using a CTI Cryogenics "Cryo-torr8" cryopump aided by a Varian "Noble VacIon ion pump". The Sm-Co type sputtered magnetic films show extremely high sensitivity to the presence of Oxygen in the sputtering environment due to possible virtual leaks from the several Viton O-Ring seals and other porous surfaces in the chamber. Contamination from Oxygen manifests itself in the form of a shoulder in the hysteresis loop of the film, as the second quadrant is entered, much like the drop seen in the case of soft magnets, causing a great reduction in the $(BH)_{max}$ of the film. For this reason, the system purity was further enhanced by cycling the sputtering inert gases at a rate of about 3 sccm. With the aid of an MKS Mass Flow Controller, the inert gases were injected into the sputtering chamber at any desired ratio and the total pressure was maintained at any desired level with the aid of an MKS Exhaust Valve and controller.

In this thesis work, the 2-17 magnetic films were deposited on either polycrystalline Al_2O_3 corundum substrates or single crystal sapphire substrates. With the help of a quartz heater lamp powered by a Kepco Power Supply, the substrates were preheated to desired temperatures. Unlike in the depositions of most pure metals, if sputter depositions were carried out without heating the substrate, the multicomponent film came out in an amorphous state. The preheating temperatures ranged from 280C to 580C. The watercooled target had a surface area of 15 cm^2 while the substrate had a surface area of 6 cm^2. The larger surface area of the target and the high sputtering gas pressures were helpful in keeping the thickness profile throughout the substrate uniform within ±3% of the average thickness. Throughout the whole series of experiments, the target to substrate distance was maintained around 50±1 mm.

The depositions were carried out in the presence of a magnetic field of 1.5KOe applied along the width of the substrate. The beneficial effects of this magnetic field which we will call H_s, will be discussed in detail in a later chapter.

The film deposition rates were generally around 4.5Ang/sec. In view of the magnetic property variation of $Nd_2Fe_{14}B$ with deposition rates, as found by Prof.Cadieu and coworkers(36), the possibility of the 2-17 film magnetic property variation with deposition rate was also explored, for rates ranging from 1.5Ang/sec to 7.5Ang/sec. Most of the films synthesized were around 5μ thick, while some films with thickness in excess of 40μ were also synthesized.

3.2 Magnetic Measurements

The magnetic measurements were made using a Foner Vibrating Sample Magnetometer, PAR VSM Model 155. Magnetic fields up to 20KOe were provided by an iron core, water cooled magnet. A schematic of the VSM is given in the lower part of Fig.4. Details of the null method of measuring the magnetic moment with a VSM can be found elsewhere(34). Through proper interfacing with a computer, the measurements were done in automated mode. Corrections for the isotropic diamagnetic contribution from the substrate (susceptibility $\approx 0.45 \times 10^{-6}$ emu/gm) were made. In measurements made perpendicular to the film plane, free magnetic pole formation at the film surfaces caused strong demagnetization fields which were given by $\delta * M$ where δ was(23),

$4\pi r^2 * [1-\{\sqrt{(1/(r^2-1))} * \sin^{-1}(\sqrt{((r^2-1)/r^2)})\}]$,

where r = film width / film thickness.

In our case $r \approx 500$ so that the demagnetization field became $4\pi M$. Thus, the true field experienced by the film was given by,

true field = (applied field - demagnetization field),

= applied field - $4\pi M$.

For measurements done perpendicular to the film plane in three different types of films, the hysteresis loops, as measured and after demagnetization correction, are given in Fig.6, Fig.7, Fig.8. It could be seen that in cases where the perpendicular loop is wide and in cases where the anisotropy field and coercivities are relatively small, the corrections are substantial, while in cases where the anisotropy field is large and the loop is narrow, the corrections are insignificant. Since, in the 2-17 type permanent magnets, the origin of the anisotropy is the strong uniaxial magnetocrystalline anisotropy, the relative widths of the inplane and perpendicular to plane hysteresis loops give us an excellent idea of the relative amount of grains oriented with c-axes away from the film plane. However, the loops compared should be for the same effective magnetic field. In other words, for the perpendicular to film plane hysteresis loops, demagnetization field corrections should be made before comparison. Accordingly, throughout this document, such corrections have been made to the perpendicular to film plane hysteresis loops.

3.3 Film Morphology, Film Thickness and Film Density Determination: Scanning Electron Microscopy

A Hitachi SEM model S-570 was used to study the film morphology. A spatial resolution, as determined by the size of the electron beam, of 50 Ang. was obtainable through this apparatus. The grain sizes which in our films were of the order of several thousand angstroms were thus easily determined. Details of scanning electron microscopy can be found elsewhere. For an accurate determination of the film thickness, the film was mounted edge on. Since the surface area of the film was known, the volume of the film could be calculated. The true density of the film was obtained by deviding the mass of the film by its volume. Comparing this value with the X-Ray density, the packing density of the grains in the film was obtained.

3.4 Study of Microstructure

The crystal structure, lattice parameters a and c and film X-Ray density are determined using a GE diffractometer coupled to a liquid Nitrogen cooled Si(Li) detector and a Canberra-Series 35 Plus MCA. A simplified block diagram of the diffraction unit is presented in Fig.9. After proper interfacing with a computer driven centroid, the data collection was fully automated. The diffraction analysis was done using Cu $K\alpha_1$ radiation. Discrimination against the fluorescence from the film was achieved using proper setting of the upper and lower discriminators. Details of X-Ray diffraction can be found elsewhere(33),(35),(36). The lattice parameters a and c were determined by minimizing an error function F for pairs of a and c obtained by varying them in steps of 0.001 Ang. The error function F was given by the following,

$\{\sqrt{[\Sigma_{a=0 \mathrm{to} N}\{(\theta_{exp}-\theta_{cal})*(\sin\theta_{exp})*(\tan\theta_{exp})\}^2]}\}/(N*K)$,

where K was equal to $[\sin(\pi/8)*\tan(\pi/8)]$ and N was the total number of diffraction lines observed and θ_{cal} was the calculated diffraction angle for that particular a and c pair. In essence, we were looking for the vortex point in the 3-Dimensional F, a, c space. This can seen from Fig.10 and Fig.11.

3.5 Quantitative Analysis of Elemental Composition of the Film

Our Hitachi Scanning Electron Microscope was fitted with an Energy Dispersive X-Ray Spectrometer. The analyzer included a liquid Nitrogen cooled Si(Li) detector, an MCA and a dedicated computer for data analysis, PGT "System 4 Plus". A schematic of the system is given in Fig.9. The advantage of coupling the system with the SEM was that the composition of any desired region could be obtained. Generally, the compositional variation from one end of the film to the other did not exceed 1%. In short, the quantitative analysis was carried out in the following fashion:

Our 2-17 film contained the elements Sm, Co, Fe, Cu and Zr. The pure elemental x-ray spectra of these elements were collected under identical conditions such as electron beam current (of the order of a hundred nanoamperes), takeoff angle and focussed area etc. The background as defined by the intensity at the analyte line energy in the absence of the analyte were subtracted from each of the above spectra and the reference standards thus obtained were stored. The spectrum of the film whose composition was to be determined was collected and after background correction, the relative intensity of the analyte line in the sample to its reference standard was calculated. To this intensity the ZAF (Atomic Number, Absorption and Fluorescence) corrections were made. In the case of our films, the Absorption corrections to the Cu relative intensities were substantial. By normalizing the sum total of all relative intensities to 100, the atomic percentage of individual elements was obtained. In the PGT System Four Plus, the analyses were based on the program FRAME C written at the U.S. National Bureau of Standards(37). Detailed descriptions of quantitative analysis can be found elsewhere(38),(39). In table 6, we have listed the composition of the TDK 2-17 target and that of one of our films. In Fig.12, the fluorescence spectrum of one of our films after background subtraction is given. The Kα lines of Co, Fe, Cu and the Lα lines of Sm, Zr have been labelled.

CHAPTER 4

THERMALIZATION OF SPUTTERED ATOMS

4.1 Introduction

In the sputtering process, the as sputtered atoms would have an asymmetric energy distribution about a peak of a few eV's with the maximum energy going up to a few hundred eV's. In general, the energy of the depositing atoms and back reflected neutral atoms could strongly influence the physical properties of the film(42). However, in the synthesis of permanent magnet films, the large momenta carried by such massive energetic particles could cause a high concentration of defects, that could lead to drastic lowering in the coercivity and hysteresis loop squareness of the film. So, in the synthesis of such films, it is important to lower the energy of the sputtered atoms, as they arrive at the substrate, to reasonably low levels of a few tenths of an eV. This could be achieved by two methods: (1) Increasing the sputtering gas pressure so that the sputtered atoms undergo increasing number of energy transferring collisions with the gas atoms (2) Sputtering with a much heavier gas species so that the high scattering angle could enhance the number of energy transferring collisions of the forward moving target atoms with the heavy gas atoms. The concept of thermalization was first quantified by Prof.Cadieu in 1974, to explain the sputter synthesis of metastable superconducting compounds(11). Since then, several authors have studied the thermalization process from theoretical as well as experimental point of view(43),(44),(45). In many of these calculations, the classical atomic scattering cross-sections were used. R.S.Robinson's analytical calculations have shown that in the binary collisions of atoms, the energy transfer cross-section is strongly energy dependent(46), that the cross-sections can decrease by as much as six times when the energy changes from 1eV to 1000eV. Through Monte Carlo techniques, Somekh has carried out thermalization calculations using these energy dependent cross-sections, for the case of single component target(47). While several authors have studied the sputtered atom energy distribution for the case of single component targets(48), not much information seems to be available as far as energy distributions in multicomponent targets is concerned. For this reason, in our calculations, for each component of the target, a reasonable sputter ejection energy distribution, which is gaussian below and exponential above a certain value, was assumed. The energy peaks of the individual components were assumed to be so placed as to make the momentum with which they are sputter ejected equal. For each sputter ejection energy of the atoms, their energy on arrival at the substrate was analytically calculated and thus the energy spectrum of the depositing atoms was reconstructed.

4.2 The Calculation

For simplicity, let us consider sputtering from a target of atomic mass m_t, in a single component gas species at pressure p, atomic mass m_g and energy transfer scattering cross-section s for collisions with the sputtered atoms. Let n be the number of collisions made by the target atom with gas atoms while travelling a total distance l. Let f be the fractional energy remaining after one collision. The energy of the gas atom after travelling distance l can be given by,

$E_d=E_0*f^n$

So, n is given by, $\{\ln [E_d/E_0]\}/\{\ln f\}$.

For convenience, it was assumed that the distance d travelled normal to the target plane, i.e., in the direction of the substrate while undergoing n collisions, can be given by,

$d = l*\langle\cos\theta\rangle = [(n*kT)/(p*s)]*\langle\cos\theta\rangle$, where $\langle\cos\theta\rangle$ is the average of the cosine of angle of scattering. In reality, this distance could be much lesser than that given by the above relation.

By assuming that the gas atom was at rest before collision, the following relations were assigned to f and $\langle\cos\theta\rangle$(40),

$\langle\ln f\rangle = 1-[\{(1-M)^2/2M\} * \{\ln|(1+M)/(1-M)|\}]$

$\langle \cos\theta \rangle = 1-M^2/3 \quad \text{for } M < 1$

$\langle \cos\theta \rangle = 2/(3M) \quad \text{for } M > 1$

where $M = m_g/m_t$.

So, the energy vs distance relation can be written as,

$\ln|E_d/E_0| = d*p*s*(\ln f)/(kT*\cos\theta)$

Now, considering the thermal energy kT of the gas atoms due to which, in the diffusion limit, the final energy of the target atoms can only become equal to kT, E_d can be given as,

$E_d = E_g + (E_0-E_g) * [\mathrm{Exp}(d*p*s*(\ln f) / (E_g*\cos\theta))]$

This formulation can be extended to more than one gas to get the following result:

$E_d = E_g + (E_0-E_g) * [\mathrm{Exp}\{ (d/E_g)*\Sigma_i(p_i*s_i*\ln f_i/\cos\theta_i)\}]$

To account for the variation of the energy transfer scattering cross-section with change in energy, E_d was calculated for a d=1mm and through iteration the energy at various distances was obtained. To obtain the energy distribution at various distances, the following approach was taken: The Sm and Co atoms were assumed to be sputter ejected with their energy peaks so placed as to correspond to equal momenta sputter ejection. So, if the energy peak of Sm were to be at 6eV, that of Co would be at 15.32eV. It was also assumed that for energies upto 6eV above the assumed peak energy, the distributions were gaussian and smoothly changing into exponential with decay constant of 13eV for higher energies. The energy spectra so constructed closely resemble the energy spectra of sputter ejected atoms from single component targets. For an energy range of 0 to 100eV, this initial distribution was devided into uniformly spaced windows of width 0.1eV. We shall call these our original windows. For the type of initial distribution described above, the initial probability for each of these original windows could be computed. Following the procedure outlined earlier, the locations of new energy windows, at various distances, corresponding to the original energy windows were calculated. The probability that atoms in these new windows were on course to the substrate was assumed to decrease by $\theta/(\pi/2)$ where θ was the total angle through which the atoms were scattered in travelling these distances. Now the probability corresponding to each of these new energy windows could be given by initial probability for the corresponding original window devided by $\theta/(\pi/2)$. However, unlike our original energy windows, these new windows were much more closely and nonuniformly spaced. Through summing up of probabilities of the new energy windows that were within the original uniform window spacing of 0.1eV, and by normalizing the overall sum of probabilities to unity, the new probability for each of our original energy windows were obtained. A representative renormalization procedure is given in Fig.23.

At this point, it has to be noted that Robinson's energy transfer scattering cross-sections were calculated using like particle inert gas atom pair potentials, that were in good agreement with experimental data on specific heat, viscosity, etc.. No data on cross-sections for non-inert gas atom collision with inert gas atoms, seems to be readily available. This unlike atom pair potential can be expected to differ from the potential assumed by Robinson, in shape as well as strength, for large impact parameter collisions. However, for low impact parameters, these potentials are likely to differ only in strength. It is the low impact parameter collisions, that are effective in the transfer of energy. In our calculations, it was assumed that the collisions of all the TM's with a particular gas species were alike. It was also assumed that the Ar-Co collisions were similar to Ar-Ar collisions, Ar-Sm and Xe-Co collisions were similar to Kr-Kr collisions and finally Xe-Sm collisions were similar to Xe-Xe collisions. It is possible that the real cross-sections are somewhat larger than the assumed cross-sections, due to the larger atomic radii of our TM's compared to Ar and of Sm compared to Xe. However, we could reasonably expect this effect to be offset by our earlier assumption that, after every two successive collisions, the sputtered atoms are sent back along the direction of the substrate.

In the 0.1 to 100 eV energy range, in which these calculations were carried out, Robinson's cross-sections were approximated by the following relation:

$$s = s_0 - c*(\ln E)$$

where s_0 is the cross-section at 1eV

For the various collisions the following values of s_0 and c were assumed:

colliding species	s_0 (sq.Ang)	c
Ar-Co	11	1.7370
Ar-Sm, Xe-Co	14	1.5200
Xe-Sm	17.5	1.8458

The initial energy peaks were assumed to be at 6eV for Sm and 15.32eV for Co, so that these atoms were sputter ejected with equal momentum. The initial energy distribution of Co was assumed to be a gaussian for energies below 21.32eV and exponential for higher energies whereas the initial energy distribution of Sm was assumed to be gaussian for energies below 12eV and exponential for higher energies. The calculations were easily carried out numerically, with the aid of a small computer.

It has to be noted that the gas density reduction effects(50), recently reported by Dr.Rossnagel, were not taken into account in the above calculations because of the complexities of system and distance dependent empirical expression. Moreover, unlike the magnetron modes for which the expression was developed, the current densities in our experiments were below twenty milliamp/cm^2. However, these gas density reduction effects could be quite significant in sputter depositions carried out at low pressures like 15μ, and could result in the sputtered atoms having significantly higher energies than what our calculations indicate. In our calculations, the gas temperature was assumed to be higher than the substrate temperature which is reasonable in view of the fact that the sputtered atoms on their way to the substrate transfer most of their energies to the gas atoms. This assumption implicitly incorporates into our calculations, a uniform reduction in gas density in the region between the target and the substrate, the density being inversely proportional to the temperature. The calculations have not considered film bombardment by the energetic neutrals, separately. Results published by Dr.Rossnagel show that in magnetron sputtering, there is significant bombardment of the substrate from energetic reflected neutrals and negative ions, even at 30μ of Ar pressure(51). From the results of that particular study, it can be inferred that the energy spectrum of the sputtered atoms would become weaker on the low energy end as they reach the substrate. This is reasonable in view of the larger collision cross-sections of low energy atoms. Thus, low energy atoms would suffer considerably more collisions than the high energy atoms and the probability that a sputtered atom reaches the substrate would decrease as the number of collisions it undergoes increases. This kind of modification to the energy spectrum of the sputtered atoms as they propagate away from the target was explicitly taken into account in our calculations. In addition, our "Energy vs. Distance" calculations can be easily extended to the high energy back reflected neutrals, even though we have not treated these neutrals separately.

4.3 Results and Discussion

The calculations lead to universally shaped energy versus normal distance curves as seen from Fig.16, Fig.17 and Fig.19 for various gas species at various gas pressures. As can be seen from the curves, the rate of energy loss is slower at regions near the substrate due to lower scattering cross-sections at higher energies. For the gas species considered, both the target components are found to be thermalized around the same normal distance. This is because, while the efficiency of energy transfer is the greatest when the sputtered atom and the target atom have comparable masses, the scattering cross-section and average scattering angle increase as the mass of the gas atom increases, giving rise to more number of collisions. The necessity to use energy dependent collision cross-section is easily understood by comparing Fig.22(a) and Fig.16. In Fig.22(a), the energy independent, thermal scattering cross-sections have been used. The energy spectra of Co atoms in 60μ of Ar for energy independent thermal scattering cross-section is given in Fig.22(b). For achieving total thermalization in Ar, while the energy dependent scattering model gives pressure values around 130μ (Fig.20(a), Fig.21(a)), the energy independent model gives pressure values less than 60μ (Fig.22(b)). From Fig.19, it could be seen that from the point of sputtered Co and Sm atom energetics, for initial energies corresponding to peaks of their respective energy distributions, 60μ of 50%Ar50%Xe admixture would be equivalent to

130μ of Ar and 40μ of Xe. In Fig.21(a), Fig.21(b) and Fig.21(c), the energy spectra of the sputtered Co atoms as they are being ejected at the target, after covering a third, two thirds and full distance to the substrate are given for 60μ Ar, 60μ 50%Ar50%Xe and 60μ Xe, respectively. For the mixture of ArXe, even the atoms ejected with 100eV energy are nearly thermalized when they arrive at the substrate, whereas for Ar, those atoms still carry energy in excess of 20eV. If instead, 130μ of Ar were used (fig 20(a)), the high energy Co would be thermalized to the same extent as in 60μ ArXe, again demonstrating the pressure equivalence, from the energy distribution consideration. However, the high energy Sm atoms would be thermalized to a somewhat lesser extent (Fig.20(b)), more so in Ar than in ArXe. An important thing to remember is that, for a given gas species, the product p*d determines the energy of the sputtered atom. In other words, if we reduced the gas pressure by half, then the same kind of energy distribution would be obtained at twice the previous distance. For example in Fig.21(b), the energy distribution for two thirds of the target to substrate distance covered would be the energy distribution at the substrate if the pressure were reduced to two thirds of the 60μ, that is for p=40μ. However, in cases such as low pressure sputtering, where there could be strong distance dependance of gas densities, the product p*d would be less relevant.

In our calculations, the gas temperature was assumed to be 800K. However, in case of low pressure sputtering using a gas of low effective mass, the gas temperature could be significantly higher than assumed and so the energy of the depositing atoms could be much higher than what our calculations indicate. Since the depositing atom energy depends on $p/E_g = p/kT$, on knowing the energy distribution of the depositing atoms for various pressures at a given gas temperature, the energy distribution for any desired pressure for different gas temperatures can be easily visualized. The effect of gas temperature on the energy-distance relation is demonstrated in Fig.17. The curves in Fig.17 are for Co atoms sputtered in 60μ of 50%Ar50%Xe. It could be easily seen that if the gas temperature were to be 500K, even the high energy Co atoms would be thermalized on travelling about two thirds of target to substrate distance, whereas if the temperature were to be 1100K, then even the Co atoms corresponding to the peak of energy distribution would not be fully thermalized on reaching the substrate, thus demonstrating the gas density reduction effects very vividly.

CHAPTER 5

CRYSTAL STRUCTURE OF THE SPUTTER DEPOSITED 2-17 FILM MAGNET

The X-Ray powder diffraction pattern of the target is given in Fig.13. The indexing given is that of the Hexagonal transformation of Rhombohedral Th_2Zn_{17} structure. The diffraction trace of one of our films is given in Fig.14. Due to the possibility of texturing and lattice parameter shifts on composition changes, it is expected that the X-Ray pattern of the film would differ from that of the powder pattern of the target. The inplane and perpendicular to the plane hysteresis loops of the film are given in Fig.15. Since in these magnets, the magnetic easy axis is along the crystalline c-axis, from the magnetic loops it could be said that, in the film there exist crystallites with their c-axes pointing out of the film plane; in other words, the film is not strongly textured. If the differences between the two traces were due to lattice parameter shifts, then , many intense lines in the target trace would remain unaccounted for. So, we can conclude that the film has differed from the target in the crystal structure.

In Table 2, Table 3 and Table 4, listings of the important diffraction lines with their spacing d, relative intensity and the (hkl) indexing of the reflecting planes of the three forms of the 2-17 compound, i.e., Th_2Ni_{17}, Th_2Zn_{17} and disordered $TbCu_7$ and that of pure 1-5 compound of the $CaCu_5$ type, are given(40). Again, it has to be noted that the given indexing of Rhombohedral Th_2Zn_{17} structure is for its Hexagonal transformation. A close study of the table reveals that every line observed in the cases of 1-5 and $TbCu_7$ type 2-17 is also observed in the cases of the Th_2Ni_{17} and Th_2Zn_{17} type 2-17 with slight shifts in d spacing.

For Hexagonal indexing, the spacing d is given by,

$$1/d^2=(4/3)*[(h^2+k^2+l^2)/a^2]+(l^2/c^2)$$

From this relation and the relations between a's and c's of the $CaCu_5$ derived structures stated in Section 2.2, it follows that the h,k and l's of the 2-17 Rhombohedral, 2-17 Hexagonal, 2-17 Disordered and the 1-5 Hexagonal are related.

These relations can be stated as follows:

$l_{1-5}=l_{dis.2-17}$, $l_{2-17(R)}=3*l_{dis.2-17}$,

$(h,k)_{2-17(R)}=(h,k)_{2-17(H)}$, $(h,k)_{dis.2-17}=(h,k)_{1-5}$,

$(h^2+k^2)_{2-17(R)}=3*(h^2+k^2)_{dis.2-17}$.

In view of these relations, the similarities between the X-Ray diffraction patterns of the above stated four structures can be easily understood.

In Table 5, a listing of the 2θ values of the diffraction lines of our film in Fig.14, is given. Using our error function F_{dis} routine, described in Section 3.4, these lines were fitted to the above four structure types. In table 5, the fitted 2θ values, with the (hkl) indexing for the four different structures along with their lattice parameters a and c, are given. It is seen that the diffraction pattern fits very well to all four structures. So, to find the right structure, a process of elimination was adopted.

For every (hkl) of the 1-5 and disordered 2-17 structures, a corresponding (hkl) of the hexagonal and rhombohedral 2-17 structures can be found. In other words, the lines observed for the disordered 2-17 and 1-5 structures are only a small subset of the lines observed for Hexagonal and Rhombohedral 2-17 structures. Since, in the case of our film, no lines beyond this small subset are observed, we have to eliminate the possibility that the structure is of the 2-17 Hexagonal or Rhombohedral type. With this, we have now reduced our choices to the pure 1-5 and the disordered 2-17 structures. On calculating the X-Ray density of the film for these two structures, the following values are found:

d_{1-5} = (8.61±0.09)gms/cc, $d_{dis.2-17}$ = (9.09±0.09)gms/cc.

The experimentally found density was (8.53 ± 0.15) gms/cc. So, if the structure were to be the pure 1-5 type, an improbable packing density of (99.0 ± 2.7)% is obtained whereas if the structure were to be of the disordered 2-17 type, a reasonable packing density of (93.5

± 2.7)% is obtained. So, we can conclude that the structure is the $TbCu_7$ type disordered 2-17(10). The disorder in this structure is limited to the "dumb-bell" site. In the bulk Rhombohedral 2-17 form, the dumb-bell site is preferentially occupied by Zr atoms which prevent the reduction in easy axis anisotropy resulting from the inplane anisotropy tendency of the "dumb-bell" Co(41). However, in these sputtered films of the disordered 2-17 form, the dumb-bell site would be occupied by Sm or Zr or Fe.

CHAPTER 6

VARIATION IN FILM COMPOSITION WITH SPUTTER DEPOSITION CONDITIONS

6.1 Introduction

As discussed in Chapter 4, the Samarium atoms and transition metal atoms, on their way to the substrate, would undergo different number of collisions and at each collision, they would suffer different average scattering angle, resulting in the relative flux of these elements at the substrate being different from that at the target. The incorporation of the arriving atoms at the substrate into the film would again be a complex function of several parameters such as the energy of the arriving species, the vapor pressure of the species, the binding energy of the species to the film surface, the temperature of the substrate surface, etc. All these complex parameter together are called the sticking coefficient. In general, the sticking coefficients of the rare earth atoms will be different from that of the transition atoms. As a result, one can expect the composition of the film to vary from that of the target. In this particular work, we studied the compositional changes with type of sputtering gas used, gas pressure and substrate preheating temperature. Generally, by raising the substrate temperature, the Sm content of the film decreased. For a given gas pressure, the Sm content increased in going from Ar to ArXe to Xe. For a given gas species, the Sm content increased with increase in gas pressure.

6.2 Samarium Content Variation with Substrate Temperature

For each gas species, holding the pressure a constant, the sputter depositions were carried out at substrate preheating temperatures varying from 250C to 465C. For sputter depositions carried out in Ar, 50%Ar50%Xe and Xe at 60μ pressure, the variation in the Sm content of the film versus the substrate preheating temperature is given Fig.25. For each gas species, the Sm content was found to decrease monotonically with substrate temperature. It could be said that, for the most part, the large differences in the vapor pressures of the RE's and TM's were responsible for this behavior. For any given temperature, the Sm content increased in going from Ar to 50%Ar50%Xe to Xe.

6.3 Samarium Content Variation with Sputtering Gas Species and Pressure

The variation in Sm content of the film for sputter depositions on substrates preheated to 345C, in different gas species, is given in Fig.24. In general, as the pressure was increased, the film Sm content increased too(9). For a given gas pressure, the Sm content increased in going from Ar to 50%Ar50%Xe to Xe. The increase in Sm content with increasing pressure was more rapid in going from Ar to 50%Ar50%Xe to Xe. For Xe, the film Sm content changed from around 12 atomic percent at 15μ to 18 atomic percent at 110μ, showing no sign of saturation. The Sm content did not exhibit saturation tendency, for any gas species, in the pressure ranges tested in this work.

At very low pressures, there would be no collisions between gas atoms and sputtered atoms, so that the film composition would simply be a function of the sputter ejection profile for the various components of the target and their sticking coefficients at the substrate. By assuming respectively, an overcosine and cosine angular distributions for sputter ejection of TM's and RE's, and taking into account the curvature of the target due to sputter erosion and assuming a sticking coefficient of unity for both TM's and RE's, the film Sm content was numerically calculated. For target Sm atomic percent of 14.2, film Sm atomic percent of 11.8 was thus expected. If we take into account, differences in sticking coefficients owing to vapor pressure differences, the actual Sm content of the film for low pressure sputtering could be even lower. For sputtering gas pressures of 15µ, the Sm atomic percent in the films were around 12.2, a value which is higher than the calculated value for very low pressures. This is partly due to the few collisions taking place as shown in Fig.18 and partly due to the possibility of large variation in the sputter ejection angular profile from one gas species to another. It has to be noted that at such low pressures, the gas density reduction effects could become important and so the actual number of collisions could be significantly lower than the calculated values. Generally, Sm content in films sputter synthesized at low pressures, was too low to give rise to strong magnetocrystalline anisotropy in the film. The coercivities observed in such films were less than 2KOe. Hysteresis loops of one such film is shown in Fig.34.

6.4 Conclusions

There is a significant depletion of the RE component in the film, at elevated temperatures. The most important reason for this, seems to be the extreme differences in the vapor pressures of the RE and TM components of the magnet. In arc-melting of sputter targets from pure elements, similar depletion of RE's were observed too. This behavior is expected in almost all the RE-TM sputter deposited films.

In RE-TM type permanent magnet films, this could cause drastic reductions in the magnetocrystalline anisotropy and coercivity. By increasing the sputtering gas pressure or by sputtering in heavier gas species, not only can RE depletion be compensated for, but it can also be enriched. The reason for this enrichment of the film in its RE component is the great differences in the masses and the atomic radii between the RE's and the TM's which gives rise to greatly different collision cross-sections and average scattering angles for these components, as discussed in Chapter 4. Film RE contents higher than in the target, can thus be easily achieved.

CHAPTER 7

FILM PROPERTY DEPENDENCE ON SPUTTERING CONDITIONS

7.1 Crystal Structure Dependence on Pressure and Gas Species

In Chapter 5, we saw that the crystal structure of our sputter deposited 2-17 magnetic film was the disordered 2-17, $TbCu_7$ type. However, the film composition dependence on substrate preheating temperature, gas pressure and gas species has implications on the phase of the deposited film. From Fig.24 and Fig.25, we can see that under some deposition conditions, the film composition can approach that of stoichiometric 1-5 compound. In fact, under these conditions, the crystal structure of the film was found to change from the disordered 2-17, $TbCu_7$ structure to that of 1-5, $CaCu_5$ structure. The transition from the disordered 2-17 to the 1-5 structure is smooth because of the close relationship between these two crystal structures.

In the disordered 2-17 structure, the "dumb-bell" site would be occupied by either a single Sm or a pair of Zr or Fe atoms, whereas in 1-5, this site is occupied by just one Sm atom. Consequently, for the disordered structure, there would be an expansion of the c-axis and contraction of the a-axis. In textured films where all the crystallites are aligned with their c-axes in the film plane, no reflections from planes with nonzero l indices will be observed. So, for such textured films of disordered 2-17 and 1-5 structures, the X-Ray diffraction traces would look alike, except that the lines due to 1-5 phase would appear at slightly lower angles.

In Fig.26, the high angle diffraction trace of three film specimens are given. All three films were sputter synthesized on substrates preheated to 345C, in gas pressures of 90μ. The figures on extreme left, middle and extreme right correspond to films synthesized in Ar, 50%Ar50%Xe and Xe respectively. The Sm content of these films are 15.2, 16.1 and 16.9 atomic percentages respectively (Fig.24). The exhibited lines correspond to (220) planes of either disordered 2-17 or 1-5 structures with the 1-5 line appearing at slightly lower angle. So, we can say that the crystal structure of film sputtered in 90μ Ar is disordered 2-17, while the film sputtered in 50%Ar50%Xe is rich enough in Sm as to exhibit mixed phases of disordered 2-17 and 1-5 as seen by the splitting of the high angle line. The crystal structure of the film synthesized in 90μ Xe is 1-5 as seen by the shift in the angle. The full X-Ray diffraction trace of the film sputtered in 90μ 50%Ar50%Xe is given in Fig.27. Every line observed shows splitting indicative of the mixed phases in the film. The inplane and perpendicular to the plane hysteresis loops of the film, given in Fig.28, confirm strong texturing from total alignment of the c-axes in the film plane.

7.2 Magnetic Property Dependence on Change in Gas Pressure and Substrate Preheating Temperature

7.2.1 Introduction

For sputter depositions carried out in a given gas species, the sputtered film magnets showed gradual changes in their remanent magnetic moment, the coercivity, energy product, perpendicular to the plane remanent moment, etc., with change in sputtering gas pressure and substrate preheating temperatures. Here, we shall discuss in detail, the film magnetic property variation, for the case of films sputter synthesized in gas species 50%Ar50%Xe, with change in pressure, substrate temperature, etc.. Since the effective mass of 50%Ar50%Xe is intermediate between those of Ar and Xe, it is easier to compare and contrast the properties of films synthesized in those gases with the films synthesized in 50%Ar50%Xe.

For films synthesized in 50%Ar50%Xe, the gas pressures were varied from 15µ to 110µ keeping the substrate preheating temperatures constant. For the same gas species, keeping the pressure a constant, films were sputtered varying the substrate preheating temperature from 250C to 465C. The observed variation in the magnetic properties of the films have been plotted from Fig.29 to Fig.32.

7.2.2 Coercivity Dependence on Pressure and Substrate Preheating Temperature

For films sputter deposited on substrates preheated to 345C, the coercivity increased almost monotonically (Fig.30), until the gas pressure was increased to 110μ. For sputtering carried out at 90μ, the coexistence of the disordered 2-17 and 1-5 phases becomes clear from X-Ray diffraction. Coercivites in excess of 6.5KOe were obtained by 60μ. However, the coercivity seemed to show saturation around 7KOe. The initial increase could be ascribed to the strengthening of the anisotropy with increasing Sm content and also possible existence of small but increasing quantities of the 1-5 phase which could act as domain wall pinning sites. For films sputtered at pressures below 30μ, the Sm content was too low to cause strong enough magnetocrystalline anisotropy and so, coercivities observed were very low. The saturation type behavior in the coercivity in films sputtered in higher pressures was due the predominant phase being 1-5 in such films.

The coercivity showed a broad hump with respect to the change in substrate preheating temperature (Fig.29). Coercivity was very low for films crystallized below temperatures of 300C since these films were for the most part amorphous as confirmed by X-Ray diffraction. Beyond 425C, the Sm content in the film was too low, causing drastic reductions in the coercivity of the film.

7.2.3 Dependence of Perpendicular to Film Plane Remanent Moment on Pressure and Substrate Preheating Temperature

The perpendicular to film plane remanent moment, B_r(perpendicular), showed a slow increase with increasing temperatures (Fig.29). On comparing the X-Ray traces of two films which had substrate temperatures of 345C and 400C (Fig.37 and Fig.39), it becomes clear that this increase is due to increase in the number of crystallites which have their c-axes pointing away from the film plane. As the perpendicular to the film plane hysteresis loops show (Fig.38, Fig.40), the greater number of grains with their c-axes pointing away from film plane results in the widening of the perpendicular to plane hysteresis loop. A qualitative explanation for this behavior will be given in section 7.4.

B_r(perpendicular) showed strong decrease when the pressure was above certain region (Fig.30) which was characteristic of the gas species used in the sputtering. As seen from Fig.33, Fig.35 and Fig.37, an increasing number of grains would have their easy axes pointing away from the film plane for depositions carried out at lower pressures. This behavior will be discussed in a later section, in terms of thermalization of the depositing atoms.

7.2.4 Dependence of Inplane Remanent Moment on Pressure and Substrate Preheating Temperature

The remanent magnetization showed a broad hump with respect to substrate temperature (Fig.31). In accordance with the decrease in the Sm content of the film (Fig.25), the saturation moment showed a slow increase with increasing temperatures. The smooth manner in which the saturation moment changed was the result of the close relationship between the crystal structures of the films. However, this increase in the saturation moment did not translate into a net gain in the remanent moment. The gain in the saturation moment was negated by the increasing number of grains which had their easy axes pointing away from film plane causing widening of the perpendicular to the plane hysteresis loops and sloping of the first quadrant inplane magnetization curve.

With respect to increase in gas pressure, the remanent moment showed a gradual decrease (Fig.32): The increase in the Sm content of the film (Fig.24), with increasing pressure causes reductions in the saturation moment. The pressure increase also reduces the number of c-axes not aligned in the film plane making the first quadrant magnetization curve flat topped (Fig.30). The net result of these two competing processes is a slow decrease in the remanent moment. However, for pressures beyond 60µ of 50%Ar50%Xe, since the B_r(perpendicular) remains very low, the inplane remanent moment shows somewhat faster drop against further pressure increases.

7.2.5 Dependence of Energy Product on Pressure and Substrate Preheating Temperature

The energy product versus pressure curve for films deposited on substrates preheated to 345C, exhibited only a narrow peak around 60µ (Fig.32). At lower pressures, the coercivity was too low to sustain a linear demagnetization behavior (Fig.34), whereas at higher pressures the increasing Sm content resulted in lower remanent moments (Fig.32). With respect to temperature, the energy product exhibited a much broader plateau (Fig.31), resultant of the broad peaked behaviors of coercivity and remanent moment (Fig.29, Fig.31) with respect to temperature.

The hysteresis loops of films deposited on substrates preheated to 345C, at gas pressures of 30µ, 45µ, 60µ and 90µ have been presented in Fig.34, Fig.36, Fig.38 and Fig.28, respectively. The gradual changes in the film magnetic properties are evident from these loops.

The widths of the perpendicular to film plane hysteresis loops can be correlated with the intensity of the X-Ray diffraction peaks from crystallographic planes with non zero l indices (Fig.33, Fig.35, Fig.37 and Fig.27). The extremely narrow perpendicular to the plane hysteresis loop of Fig.38 can be correlated to the total absence of reflections from planes with nonzero indices (Fig.37). Also note that splitting of the diffraction lines in Fig.27, indicating that now the film is a two phase material.

7.3 Film Magnetic Property Dependence on Gas Species and Thermalization Effects

7.3.1 Xe versus 50%Ar50%Xe

The general behavior of magnetic properties of the film for any gas species showed the same pattern as seen in the case of 50%Ar50%Xe, the difference being that, in case of Xe, the optimum film properties were achieved at lower pressures and in case of Ar, the optimum film properties were achieved at higher pressures. In case of Xe, the rate of increase of the film Sm content with increasing pressure was faster than that for 50%Ar50%Xe, for a given substrate preheating temperature (Fig.24). This would imply that the remanent moment versus pressure peak would be much narrower than in the case of 50%Ar50%Xe. Indeed, the experimental results did show this expected behavior. As expected the region over which the energy product had sustained high values, was also quite narrower than in the case of 50%Ar50%Xe.

7.3.2 Sputter Synthesis in Argon and Film Magnetic Properties

In the case of sputter deposition carried out in pure Ar, we encountered an altogether different situation. For films sputter deposited in 50%Ar50%Xe or Xe, where the Sm content was in excess of 15 atomic percents, coercivities in excess of 6.5KOe were obtained. In addition, even at 60μ pressure of 50%Ar50%Xe and 45μ of Xe, it was possible to suppress the growth of grains with c-axes pointing away from the film plane. For the case of Ar, at pressures in excess of 130μ, it was indeed possible to suppress the growth of grains with c-axes pointing away from the film plane (Fig.30). However, the Sm atomic percentage which was sufficient to entail large coercivities and high loop squareness in case of 50%Ar50%Xe or Xe only resulted in somewhat lower coercivities and loop squareness. This could be seen by comparing Fig.30 and Fig.24. It can be seen that while 15 atomic percents of Sm was enough to show coercivities in excess of 6.5KOe, the same amounts of Sm could show only smaller coercivities and the perpendicular to film plane hysteresis loop continued to be wide. The demagnetization curves of films sputter deposited in Ar at pressures below 130μ departed from linearity and the energy products were consistently lower than in the case of 50%Ar50%Xe (Fig.31, fig32). However, as expected from the slower increase in the Sm content against Ar pressure increase (Fig.24), the energy product plateau seen against pressure variation, was wider than for 50%Ar50%Xe.

7.4 Thermalization Effects and Preferential Alignment

7.4.1 Inplane Anisotropy

Comparing the magnetic properties of films sputtered in 50%Ar50%Xe with those sputtered in Ar, we find that the former invariably exhibited superior magnetic properties. From our thermalization modelling in Chapter 4, we saw that, from the point of view of sputtered atom average energies, pressures of 60μ of 50%Ar50%Xe would be equivalent to 130μ of Ar (Fig.19). In addition, according to the calculation, for these pressures, even the energy distributions show remarkable similarities between them (Fig.20(a) and Fig.20(b)). In the sputter deposition process, the film properties would be strongly influenced by the input of energy from the depositing atoms. The high energy sputtered atoms and neutrals could have a particularly disruptive effect on the film growth process. It is possible that, in the case of our magnetic films, the disruptions caused by these high energy particles could result in grain boundary imperfections, lattice defects etc. that could act as domain nucleation sites, whereby the coercivity and loop squareness values could be effected(55). Comparing the energy distribution curves of Co and Sm, sputtered in Ar and 50%Ar50%Xe, it becomes clear that for films synthesized in Ar pressures less than 100µ, there will be considerable bombardment by high energy atoms that could result in disruptions detrimental to grain coercivity. This causes either reduction in coercivity of film or can cause nonlinear demagnetization behavior. Either way, great losses in energy products are suffered.

In section 7.2.3, we saw that perpendicular to plane remanent moment, B_r(perpendicular), exhibited a slow increase with increase in substrate preheating temperature. The increase of B_r(perpendicular) was more rapid against lowering of the gas pressure below the pressure required to thermalize most sputtered atoms.

During the sputter deposition process, through the use of thermocouple probes, an increase in the substrate temperature of about 50C was observed. This was primarily due to film bombardment by the electrons from the discharge region. This increase was more a characteristic of the input RF power than that of gas species or pressure over small ranges. Due to this increase in the temperature, the deposition temperature was generally higher than the substrate preheating temperature by about 50C.

The grain sizes in our 2-17 films deposited on preheated substrates have been of the order of a couple of thousand Angstroms. The deposition temperatures of these films were generally much lower than the Curie temperature of the magnet material, which makes the magnetic alignment energy of the grains, resulting from the demagnetization field of the film, larger than their thermal energy by a few orders of magnitude. For a grain diameter of 1500Ang., the magnetic energy would be around $1\mathrm{x}10^{-8}$ergs, whereas its thermal energy would only be around $1\mathrm{x}10^{-13}$ergs. In that case, the demagnetization field of the film would force the c-axes of the grains to align in the film plane. However, the observed behavior has been quite different, as discussed in the earlier sections. From this, it becomes clear that we should consider energies of only a few freshly depositing monolayers, instead of the whole grain, in which case the thermal energy could become strong enough to cause sufficient number of seed grains to point away from the film plane. Once the seed grains are nucleated, the rest of the deposition process can be roughly considered as a process of duplication of layers. The potential energy of the layers in the presence of demagnetization field $4\pi M$, can be given by $4\pi M^2 *$(volume of the layers), while the thermal energy can be given as kT. So, on raising the substrate temperature, more seed grains can point away from the film plane. However, due to the bombardment by massive particles such as the depositing atoms and high energy neutrals, etc., that can transfer large momentum to the atoms in the growing film surface, the growing film surface could act like it is at a temperature much higher than that of the bulk of the film. This effect would be quite strong in case of low pressure sputtering, due to much greater amount of higher energy atom bombardment. This kind of apparent increase in the surface temperature could determine the orientation of the easy axis of the seed grain in a manner similar to what was discussed in the context of preferential alignment versus temperature. So, if the momenta of the bombarding particles are sufficiently lowered through thermalization of their energies, the growth of grains with c-axes pointing away from film plane can be suppressed. This indeed was the case in films sputter deposited in 60μ and higher pressures of 50%Ar50%Xe at lower temperatures. The effect on the growth of grains with c-axes pointing away from the film plane with lowering the pressure is quite enormous in view of the rapid increase in the demagnetization energy resulting from increases in $4\pi M_s$ on pressure reduction. This could be seen from comparing perpendicular to film plane loops in Fig.38 and Fig.34, where the variable is pressure, as against perpendicular loops in Fig.38 and Fig.40, where the variable is substrate preheating temperature.

7.4.2 Effect of H_s and within the Plane Anisotropy

The demagnetization field of the magnetic film is isotropic within the film plane. While the demagnetization energy was exploited to cause full alignment of the c-axes of the grains in our films synthesized through thermalized sputtering, it was unable to induce anisotropy within the film plane due to its isotropic nature within the film plane. For this reason, a magnetic field of 1.5KOe was applied in the plane of the substrate along its width. Application of a magnetic field to induce anisotropy in RE-TM crystalline as well as amorphous films has been attempted by other groups of researchers too(52). To the most part, the process of sputter deposition on a preheated substrate, should be considered as a process of duplication of layers, once the seed grains are nucleated. In Fig.43 and Fig.44, the inplane hysteresis loops, parallel and perpendicular to H_s, of two films sputter deposited using 60µ of 50%Ar50%Xe for substrate temperatures of 308C and 464C are given, respectively. It could be seen that the higher temperature case does not exhibit even the weak within the film plane anisotropy exhibited by the lower temperature case. This could be understood on the following basis: The magnetocrystalline anisotropy weakens quite rapidly with rise in temperature, allowing the magnetization vector in the grains to point away from the easy axis and along the H_s, without great increase in the magnetocrystalline anisotropy energy. So, in the case of higher temperature depositions, the crystallites need not necessarily grow with their c-axes pointing along the H_s. However, at lower temperatures, due to higher magnetocrystalline anisotropy energies, growth of grains with c-axes pointing along the H_s is preferred instead of the magnetization vector pointing away from the easy axis. The disappearance of anisotropy within the film plane with reductions in gas pressure can be seen from Fig.45 and Fig.46, where loops for films deposited on substrates preheated to 345C in 30μ and 60μ of 50%Ar50%Xe respectively are given. Again, the apparent surface temperature rise due to bombardments by massive energetic particles capable of imparting large momenta to atoms on the growing film surface and the consequent reduction in anisotropy energy can be invoked to explain this behavior. For magnetization along H_s, hysteresis loop squareness was improved, allowing us to realize higher energy product values in that direction.

In Fig.41, the magnetization, when the net field was reduced to zero, versus angle between the applied field and film plane are given for two films deposited on substrates preheated to same temperature, in 50%Ar50%Xe at pressures of 60μ and 45μ are given. At each angle where the measurement was taken, the field was first increased to 18KOe. For the 60μ case, large changes in magnetization are seen whereas in the 45μ case, changes are smaller. This was because of the total alignment of the c-axes of the grains within the film plane, in the 60μ case. In Fig.42, the same kind of measurement for magnetization at 18KOe applied field are given. Again, in the 60μ case, the magnetization changed by nearly 80% indicating anisotropy fields around 70KOe, whereas in the other case only changes of about 40% were obtained. (also see hysteresis loops of the film made in 60μ, in Fig.38). For the film synthesized in 60μ, the anisotropy energy was estimated to be around $5x10^7$ erg/cc. The inplane loop squareness ($B_r/4\pi M_{18KOe}$) was around 83%. If in this polycrystalline film, the c-axes distribution were to be totally isotropic within the film plane, then the loop squareness would be $(2/\pi)=0.628$(53). In our estimation of loop squareness we had taken the value of the saturation magnetization as that at 18KOe, instead of the value at the anisotropy field. From an estimation of the anisotropy field, and thus the saturation moment, the true loop squareness was estimated to be around 0.75, which is higher the 0.628 expected for random c-axes distribution within the film plane. This was the result of the applied magnetic field H_s, which induced a small degree of anisotropy within the film plane.

7.5 Synthesis of Films with Thickness in Excess of 15μ

Generally, due to the disappearance of grain boundaries during the sputter deposition process of the film, stresses which are inhomogeneous in depth are developed(32). While stresses of this nature by themselves did not cause any strong problems in the case of our films, stresses that arise out of the thermal expansion coefficient mismatch between the magnet and substrate material was a problem. The thermal expansion coefficients of our 2-17 magnet film was much higher than that of the substrate. So, on bringing the system down to room temperature, strong tensile stresses were exerted on the film. When the thickness of the film exceeded 15μ, this stress reached the ultimate strength of the film causing it to crack or peel off from the substrate. A transition layer of Aluminium was found to solve this problem. The required thickness of the transition layer increased, as the film thickness and deposition temperatures increased. In any case, a thickness of less than 5% of the film thickness was sufficient. In Fig.5, a Scanning Electron Micrograph of a thick film with its transition layer is shown. The transition layer did not cause any significant changes in the film magnetic properties.

The grain boundary erosion of these thick films as the film was growing can be clearly seen in the scanning electron micrograph shown in Fig.5. This grain boundary erosion was a consequence of the recrystallization process going on in the film as the film was adding on thickness. The consequence of these recrystallization processes have been somewhat disadvantageous to the magnetic properties of the films.

One of the consequences of grain boundary erosion was that the grain sizes in regions closer to the substrate were larger than near the film surface. For these 2-17 type magnets, in the bulk form, estimates of single domain grain sizes are in the several micron range. It is possible that near the substrate, the grain sizes in our extremely thick films could exceed the single domain size. This would give rise to nonlinear demagnetization curves as well as reductions in coercivity. In fact, our extremely thick films did not exhibit linear demagnetization behavior and the coercivities observed were considerably smaller than in thinner films. Another consequence of the grain boundary erosion was the appearance of some grains with c-axes pointing away from the film plane even for depositions carried out through thermalized sputtering. This caused some reductions in the inplane remanent moment. As a result of these two effects, for thermalized sputtering in 60µ of 50%Ar50%Xe, 40µ thick films exhibited only 16.5MGOe energy products. The negative effects of grain boundary erosion could be seen by comparing hysteresis loops of a very thick film with its thin counterpart. In Fig.47, loops of a 23µ thick film is given; Fig.38 is for a 5µ thick film. Both the samples were deposited on substrates preheated to 345C, in 60µ of 50%Ar50%Xe. In the sputter synthesis of these thick films, low gas pressures resulted in dense packing of grains while sputtering at higher pressures resulted in reductions in the packing density of grains. In thick films sputtered in 60µ of 50%Ar50%Xe, grain packing density of around 93% was found, whereas in films sputtered in higher pressures it was found to drop to as low as around 85%. This kind of drop in the packing density would not only cause substantial reduction in the remanent moment and energy product, but also be harmful to the long term chemical stability of the film material.

CHAPTER 8

CONCLUSIONS

A systematic study of the synthesis of thick 2-17 type permanent magnet films, by sputter deposition on preheated substrates has been made. The films were sputter deposited from bulk TDK 2-17 targets. Inert gas species Ar, 50%Ar50%Xe and Xe, at various pressures were used in the glow discharge sputter deposition process. The systematic study helped elucidate the various relations among the magnetic property changes, the film composition changes, the crystal structure changes and sputtering parameters.

By varying the sputtering parameters, it was possible to vary the film elemental composition. The RE-TM type magnets are made of two components whose atomic masses, vapor pressures, electronegativities etc., differ a great deal. Due to these large differences in their physical properties, the angular sputter ejection profile, the transport of the sputtered atoms to the substrate and the sticking coefficient at the substrate for these two components differed too. Consequently, the composition of the film was different from that of the target. This composition change was studied for changes in substrate preheating temperatures, gas pressures and gas species. It was found that the depletion of the RE component with increase in temperature could be reversed either by sputtering with a heavier gas or by increasing the gas pressure. The film compositions so obtained ranged from 12.1 atomic percent to at least 18 atomic percent of Sm, 14.2% being the target Sm content.

In accordance with compositional changes, the crystal structure of the film was also found to differ from that of the target. Until the Sm content reached approximately 16 atomic percentage, the only crystal phase detectable by X-Ray diffraction, was the disordered 2-17, $TbCu_7$ type. Between 16 and 17 atomic percentage Sm, in addition to the disordered 2-17, the film contained detectable amounts of 1-5 phase too. Beyond this range, the film formed in the 1-5 form.

A numerical method of calculating the energy of the sputtered atoms as they traverse towards the substrate was developed. The formulation was quite similar to the original calculation done by Prof.Cadieu in 1974, the difference being, (1)an energy dependent cross-section for energy transfer collisions between the sputtered atoms and gas atoms was considered, (2)the average angle of collision was taken into account in calculating the distance travelled normal to the target. The model was extended to find changes in the energy distribution of the sputtered atoms as they proceed towards the target. According to this model, in 60μ of 50%Ar50%Xe, TM atoms ejected with even 100eV energy would possess no more than half eV energy while reaching the substrate. Through this model, it was possible to explain the preferential c-axis alignment of the crystallites in the film as well as the demagnetization behavior of the film.

In accordance with the close relationship between the crystal structures of disordered 2-17 and 1-5, the magnetic moment also showed a smooth variation with the changes in sputtering parameters. Films sputter deposited using low mass Ar exhibited higher magnetic moment, at 18KOe applied field, than the films sputter deposited using higher effective mass 50%Ar50%Xe and an even higher mass Xe. For a given gas species, films synthesized at lower pressures exhibited larger magnetic moments at 18KOe applied field. This was a direct result of the increase in the TM components of the film.

The B_r(perpendicular) showed a slow increase with respect to substrate temperature. It also showed a rapid increase below certain gas pressure, the value of this pressure was characteristic of the gas species used. The relationship between these values for different gas species could be understood in terms of the pressure equivalence of gas species from the point of view of their effectiveness in thermallizing incoming high energy atoms. These pressure values decreased with increase in the effective mass of the sputtering gas.

The coercivities of the films, synthesized using the heavier gas species 50%Ar50%Xe, showed higher values than those synthesized using the lighter Ar, even when these films contained comparable amounts of Sm. From the thermallization model, this was explained as due to disruptions in the growing film which was subjected to bombardment by high energy particles, while the sputtering gas was Ar.

The films synthesized using 50%Ar50%Xe showed up to 20% higher energy products than films synthesized in Ar. The advantage of using 50%Ar50%Xe was that it would sufficiently thermallize the sputtered atoms over large ranges of sputter ejection energies, while allowing optimum amount of Sm in the film. This was important, because larger amounts Sm, while strengthening the magnetocrystalline anisotropy, reduced the saturation moment. Through the thermallization model, the alignment of the c-axes of grains in the film plane was explained.

The H_s, magnetic field applied during film deposition, was able to induce a small degree of anisotropy within the film plane, which enhanced the hysteresis loop squareness of the film, for magnetization in the direction of the H_s. The influence of H_s was found to be quite significant for thermallized sputter depositions at lower temperatures. In films synthesized under optimum sputtering conditions, the energy products in the direction of H_s were up to

20% higher than in within the film plane, perpendicular to H_s direction.

Energy products in the vicinity of 20MGOe were achieved for thermallized sputtering using 50%Ar50%Xe and Xe. Loop squareness of about 0.75 was achieved. Anisotropy fields in the 70KOe range were achieved. Anisotropy energies, for magnetization in the film plane as opposed to perpendicular to the film plane, exceeded $5x10^7$erg/cc.

In films with thickness exceeding 15µ, the tensile stress on the film from mismatch of thermal expansion coefficients of substrate and the film magnet caused cracks or peeling off from the substrate. This problem was overcome through a transition layer of Al and its oxide. During the prolonged periods of sputtering required for the synthesis of these thick films, some recrystallization effects were observed in the form of small amounts of crystallites with c-axes pointing away from the film plane due to which somewhat lower values of energy products were obtained for these films. The continuous disappearance of grain boundaries was probably responsible for the somewhat poorer magnetic properties of these thick films. In 40µ thick films, even for optimized thermallized sputtering, energy products of only 16.5 MGOe were observed as opposed to about 20MGOe obtained in case of 5µ thick films.

In conclusion, we have demonstrated the sputter synthesis of 2-17 type hard magnetic films from commercially available bulk targets, such that film magnetic properties were comparable to those of the bulk. While some results of the work were applicable to the synthesis of other RE-TM permanent magnet systems, some other aspects were unique to the 2-17 system. As a result of this work, a great degree of control over properties of 2-17 type film magnets was possible through proper choice of sputter deposition conditions. The thermallization model dealing with sputtered atom kinematics was largely successful in explaining the sputter deposition conditions necessary to achieve square hysteresis loops and strong inplane alignment of the c-axes of the crystallites in the polycrystalline film.

TABLE 1

Comp.	*Str.Type*	*Symm.*	*Sp.Group*	*R site*	*M site*	*M* .
RM_2	$MgCu_2$	cub	Fd3m	8(a)	16(d)	Ni,Co Fe
	$MgZn_2$	hex	P63/mmc	4(f)	2(a),6(h)	Mn .
RM_3	$PuNi_3$	Rh	R_3m	3(a),6(c)	3(b),6(c) 18(h)	Ni,Co Fe
	$CeNi_3$	hex	$P6_3/mmc$	2(c),4(f)	2(a),2(b) 2(d),12(k)	Ni,Co .
R_2M_7	Ce_2Ni_7	hex	$P6_3/mmc$	$4(f_1),4(f_2)$	2(a),4(e) 4(f),6(h) 12(k)	Ni,Co
	$GdCo_7$	rh.	R_3m	$6(c_1),6(c_2)$	3(b),6(c) 6(c),9(e) 12(h)	Ni,Co .
R_6M_{23}	Th_6Mn_{23}	tetr	Fm3m	24(e)	4(b),24(d) $32(f_1)$ $32(f_2)$	Fe,Mn .
RM_5	$CaCu_5$	hex	$P6_3/mmc$	1(a)	2(c),3(g)	Co,Ni Zn,Cu
R_2M_{17}	Th_2Ni_{17}	hex	$P6_3/mmc$	2(b),2(d)	6(g),12(j)	Ni,Fe
	Th_2Zn_{17}	rh	R_3m	6(c)	6(c),9(d) 18(f),18(h)	Ni,Co Fe .
RM_{12}	$ThMn_{12}$	tetr	I_4/mmc	2(a)	8(f),8(i) 8(j)	Mn .

Table 2

Powder Diffraction Pattern of

Sm_2Co_{17} (HEXAGONAL) Th_2Ni_{17} Type

d(a)	Intensity	hkl
3.329	20	201
2.928	50	112
2.420	55	300
2.092	80	220
2.081	100	302
2.044	45	004
1.933	20	213
1.864	50	223
1.561	20	304
1.476	40	412
1.462	40	224
1.396	30	330
1.321	35	332
1.209	45	600

Table 3

Powder Diffraction Pattern of
Sm_2Co_{17} (Rhombohedral) Th_2Zn_{17} Type

d(a)	Intensity	hkl
2.916	50	113
2.803	20	104
2.425	60	300
2.317	50	024
2.098	100	220
2.081	100	303
2.041	40	214
2.025	20	006
1.866	60	223
1.825	50	116,125
1.680	20	134
1.555	40	306,315
1.477	40	143
1.466	40	217,324
1.457	60	226,045
1.401	40	330
1.376	20	235
1.322	100	333
1.313	40	137,054
1.290	40	119
1.255	40	407,244
1.212	100	600

Table 4

Powder Diffraction Pattern of Sm_2Co_{17} (DISORDERED) $TbCu_7$ Type		
d(a)	Intensity	hkl
2.929	30	101
2.428	30	110
2.103	45	200
2.087	100	111
2.041	30	002
1.869	20	201
1.481	12	211
1.464	20	202

Powder Diffraction Pattern of $SmCo_5$ (HEXAGONAL) $CaCu_5$ Type		
d(a)	Intensity	hkl
2.926	70	101
2.498	54	110
2.163	54	200
2.115	100	111
1.988	19	002
1.900	16	201
1.513	15	211
1.464	20	202
1.354	21	301
1.248	20	220

Table 5

OBSERVED 2θ	CALCULATED					
	Th_2Ni_{17} a=8.482,c=8.118		Th_2Zn_{17} a=8.482,12.177		$CaCu_5$ and $TbCu_7$ a=4.897,c=4.059	
	2θ	hkl	2θ	hkl	2θ	hkl
30.43	30.43	112	30.43	113	30.43	101
36.73	36.70	300	36.70	300	36.70	110
43.15	43.15	302	43.15	303	43.15	111
48.40	48.43	222	48.43	223	48.43	201
62.33	62.27	142	62.27	143	62.27	211
70.52	70.54	332	70.54	333	70.54	301
78.05	78.06	600	78.06	600	78.06	220

Note:

(a) The tolerance on the values of lattice parameters a and c is ± 0.20%

(b) The lattice parameters are given in Angstrom units

Table 6

ELEMENTAL COMPOSITION OF TDK 2-17 TARGET AND FILM SHOWING STRONG INPLANE ANISOTROPY

ELEMENT	TARGET		FILM (DM215)	
	Percentage		Percentage	
	Weight	Atomic	Weight	Atomic
Sm	29.4	14.2	31.1	15.1
Co	45.3	55.5	44.7	55.7
Fe	15.5	20.1	14.8	19.4
Cu	6.7	7.7	6.5	7.5
Zr	3.1	2.5	2.9	2.3

Note:
The tolerance on the atomic percentage of composition is ± 0.3%

Figure 1

Schematic Representation of Stacking Modes of Various RE-TM Structures

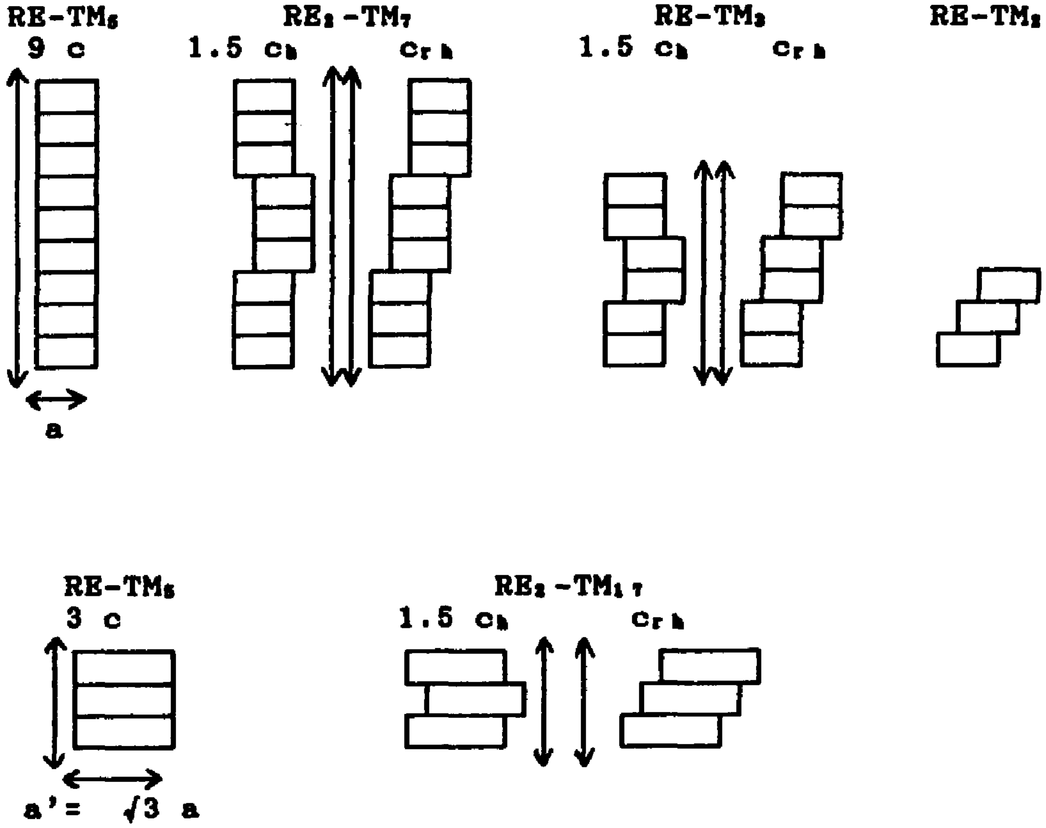

Figure 2

Crystal Structures of RE-Co_5 and RE_2Co_{17} Compounds

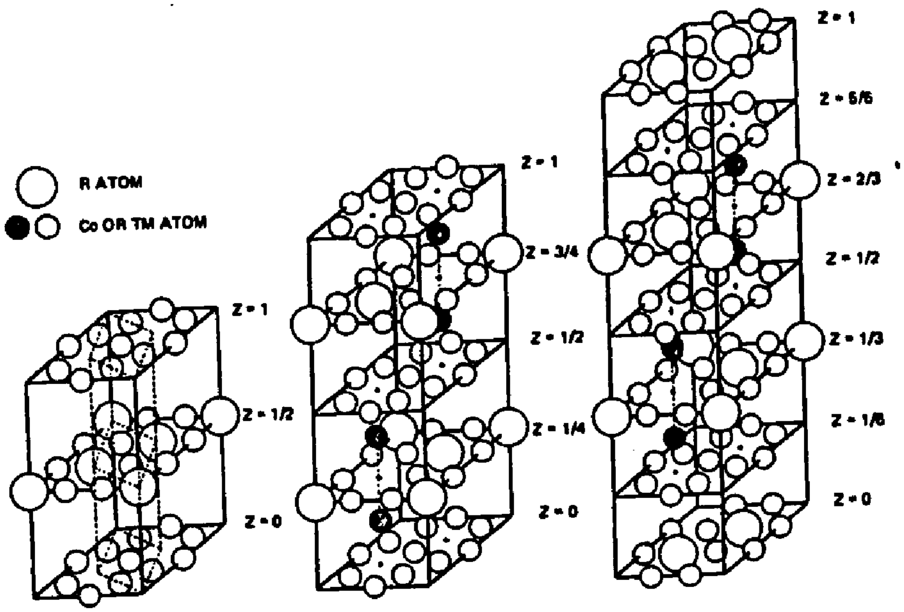

(A) RCo_5 STRUCTURE
($CaCu_5$ TYPE)

(B) R_2Co_{17} STRUCTURE

HEXAGONAL MODIFICATION
(Th_2Ni_{17} TYPE)

RHOMBOHEDRAL MODIFICATION
(Th_2Zn_{17} TYPE)

Figure 3

Curie Point and Magnetic Moment per TM Atom versus Molar Fraction of TM Atoms in Binary RE-TM Magnetic Systems

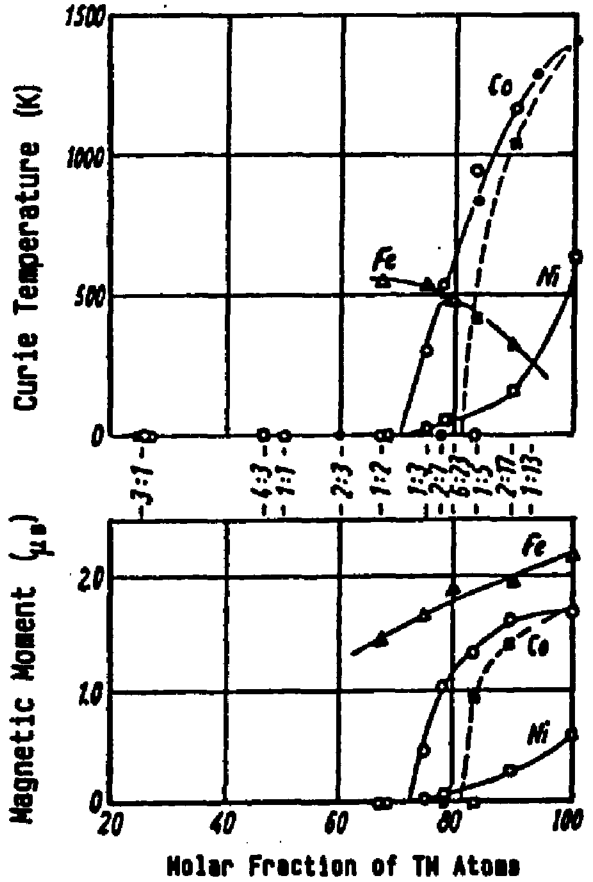

○ Y-Co, ● L-Co, ■ Th-Co, □ Y-Ni, △ Y-Fe

Figure 4

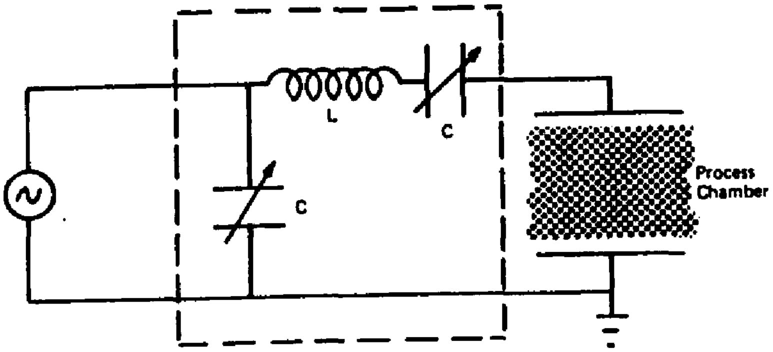

A typical rf matching network

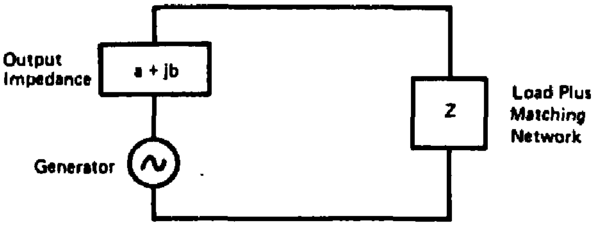

RF circuit with load impedance Z

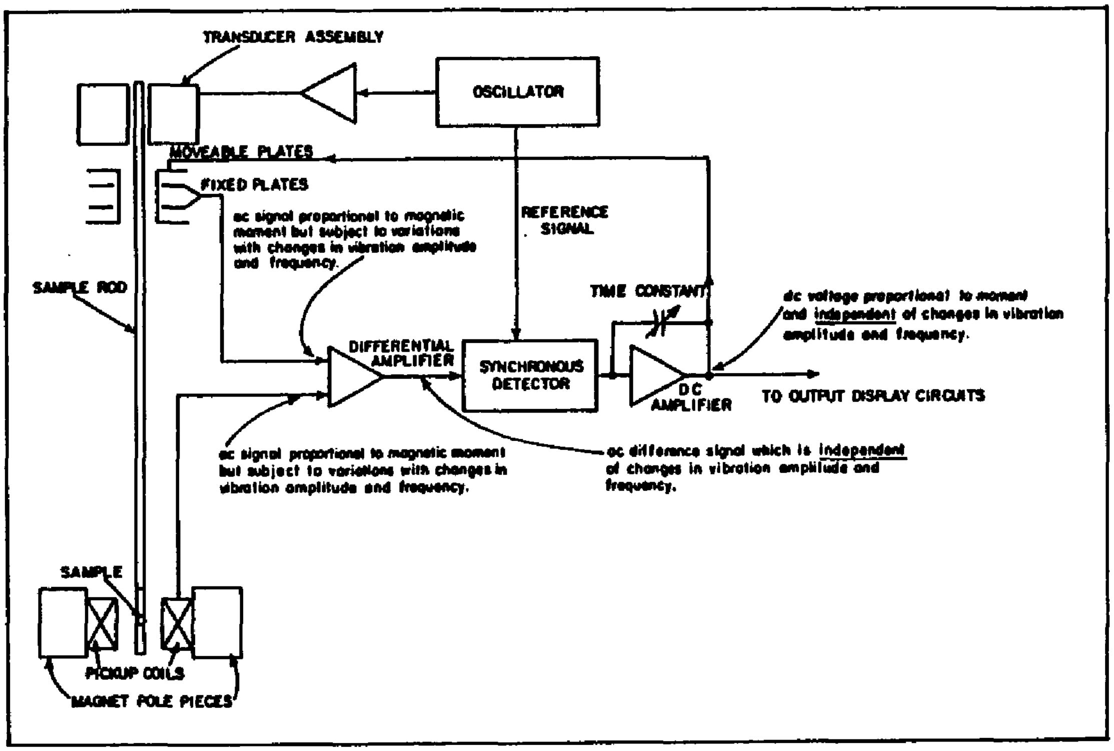

SIMPLIFIED BLOCK DIAGRAM OF THE MODEL 155 MAGNETOMETER

Figure 5

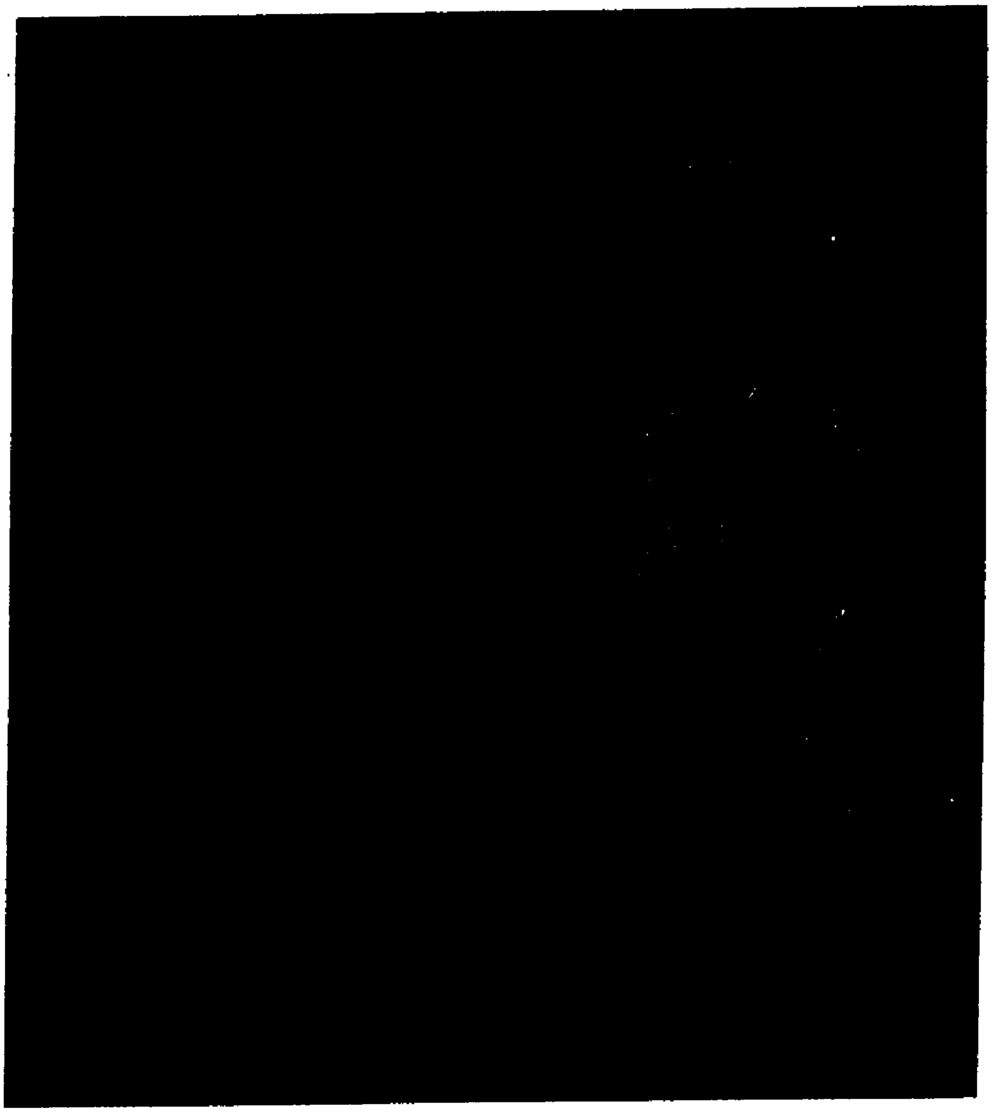

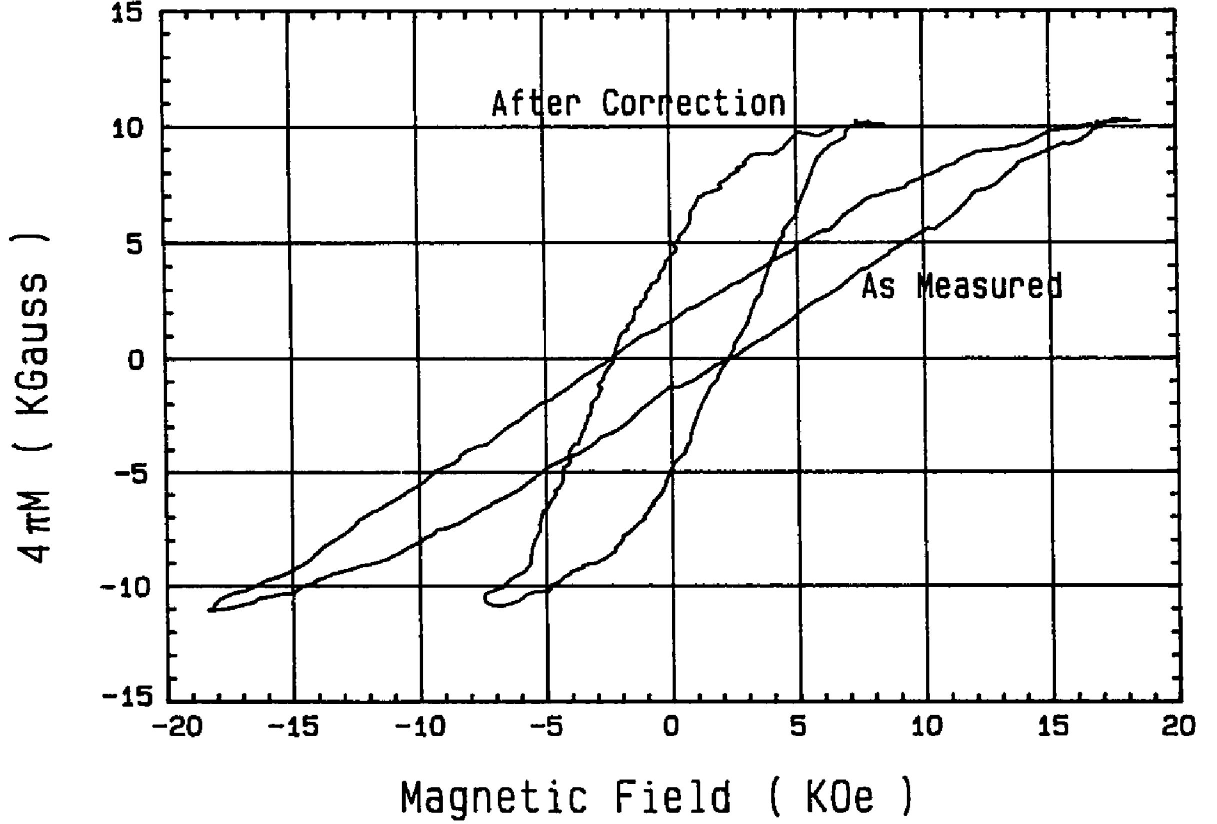

Perpendicular to Plane Hysteresis Loop of Sample DM221

As Measured and after Demagnetization Correction

$P = 15\mu$, 100%Xe, T=345 C

Figure 6

Perpendicular to Plane Hysteresis Loop of Sample DM177
As Measured and after Demagnetization Correction

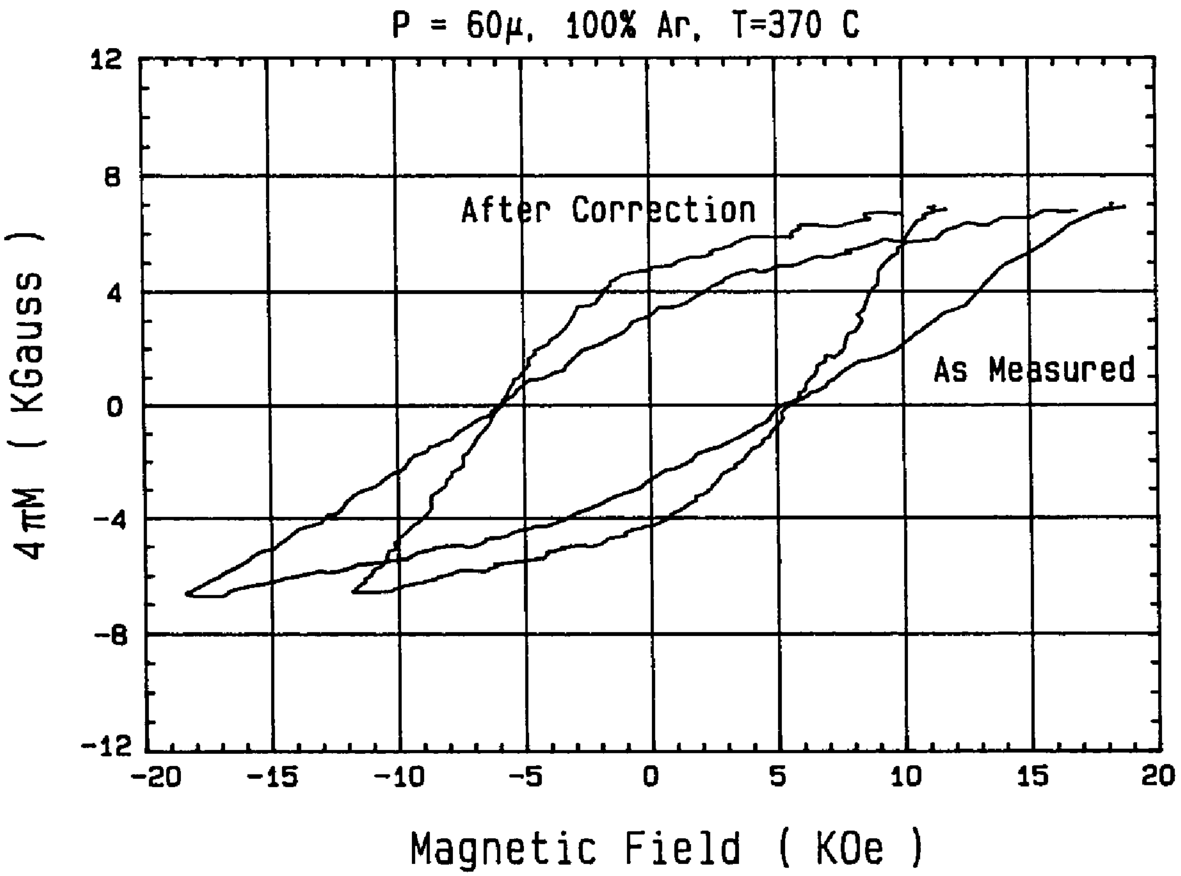

Figure 7

Perpendicular to Plane Hysteresis Loop of Sample DM215
As Measured and after Demagnetization Correction

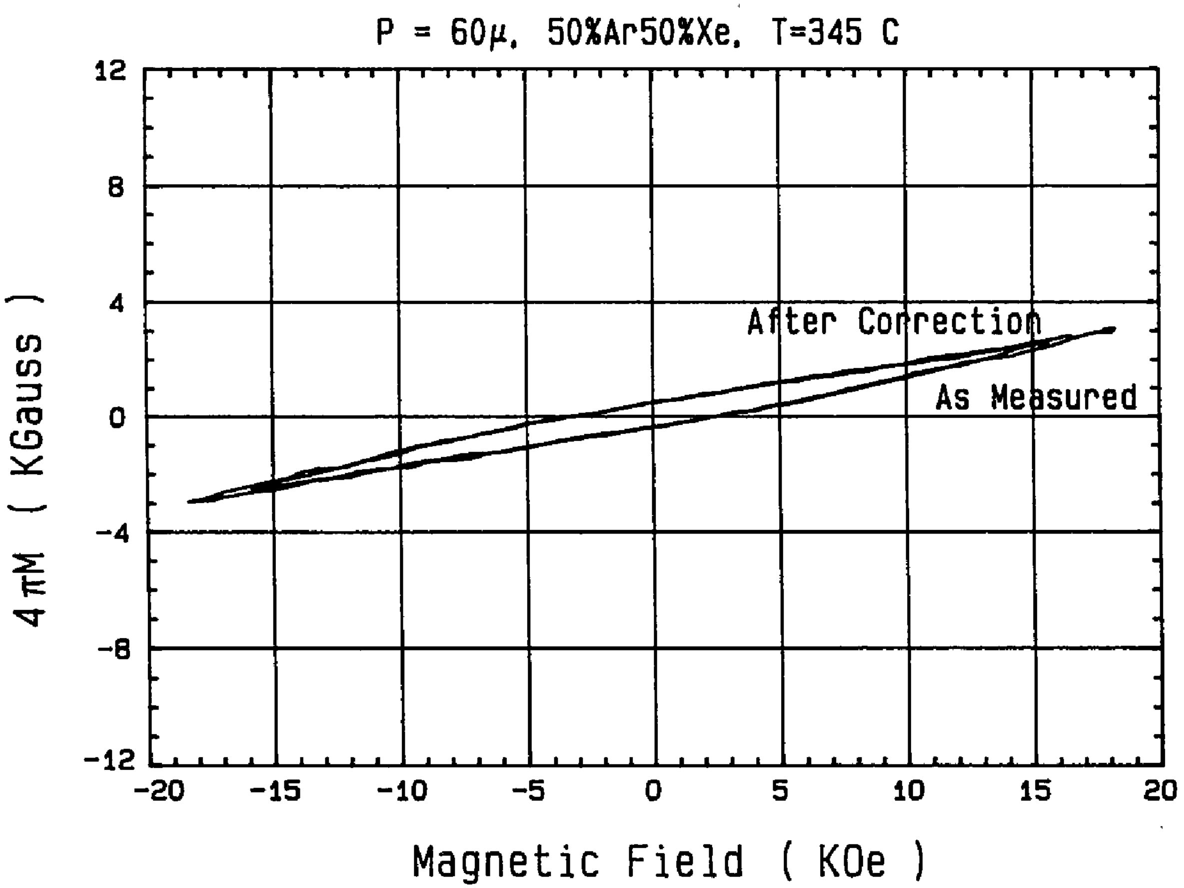

Figure 8

Figure 9

Functional Block Diagram of XES / Diffractometer System

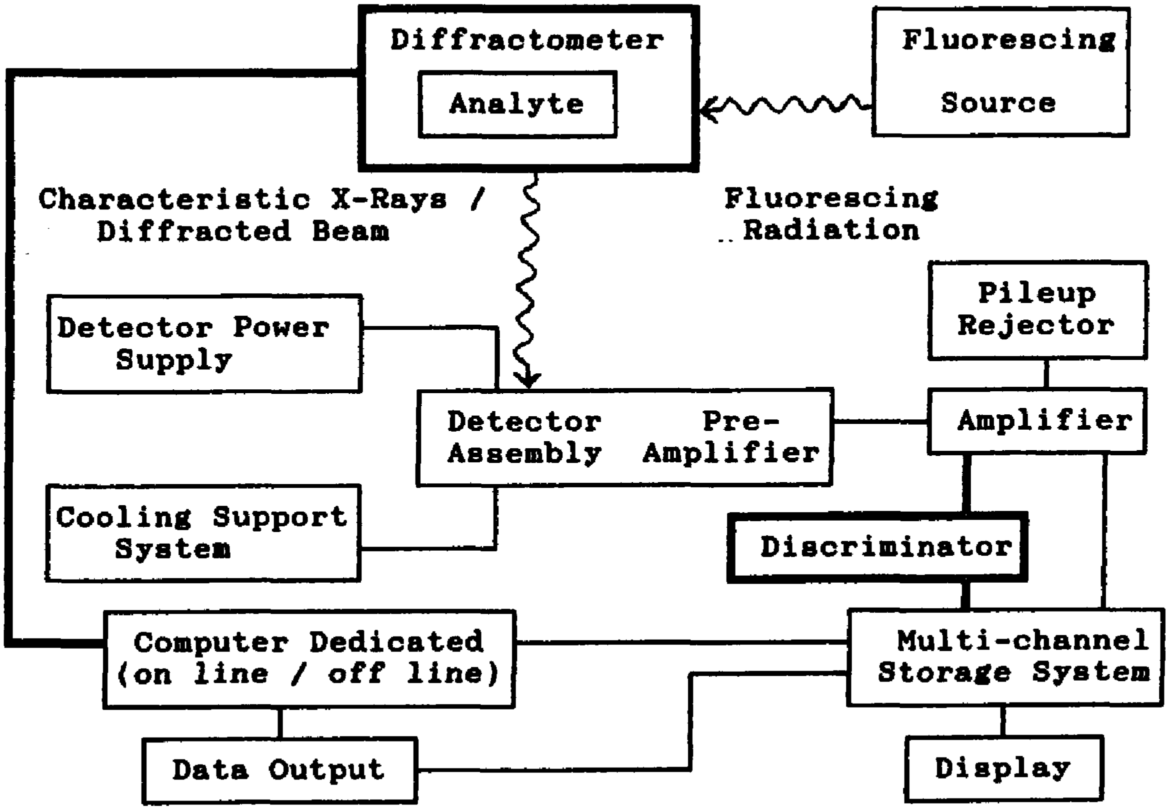

▬ Accessories required for X-Ray Diffraction

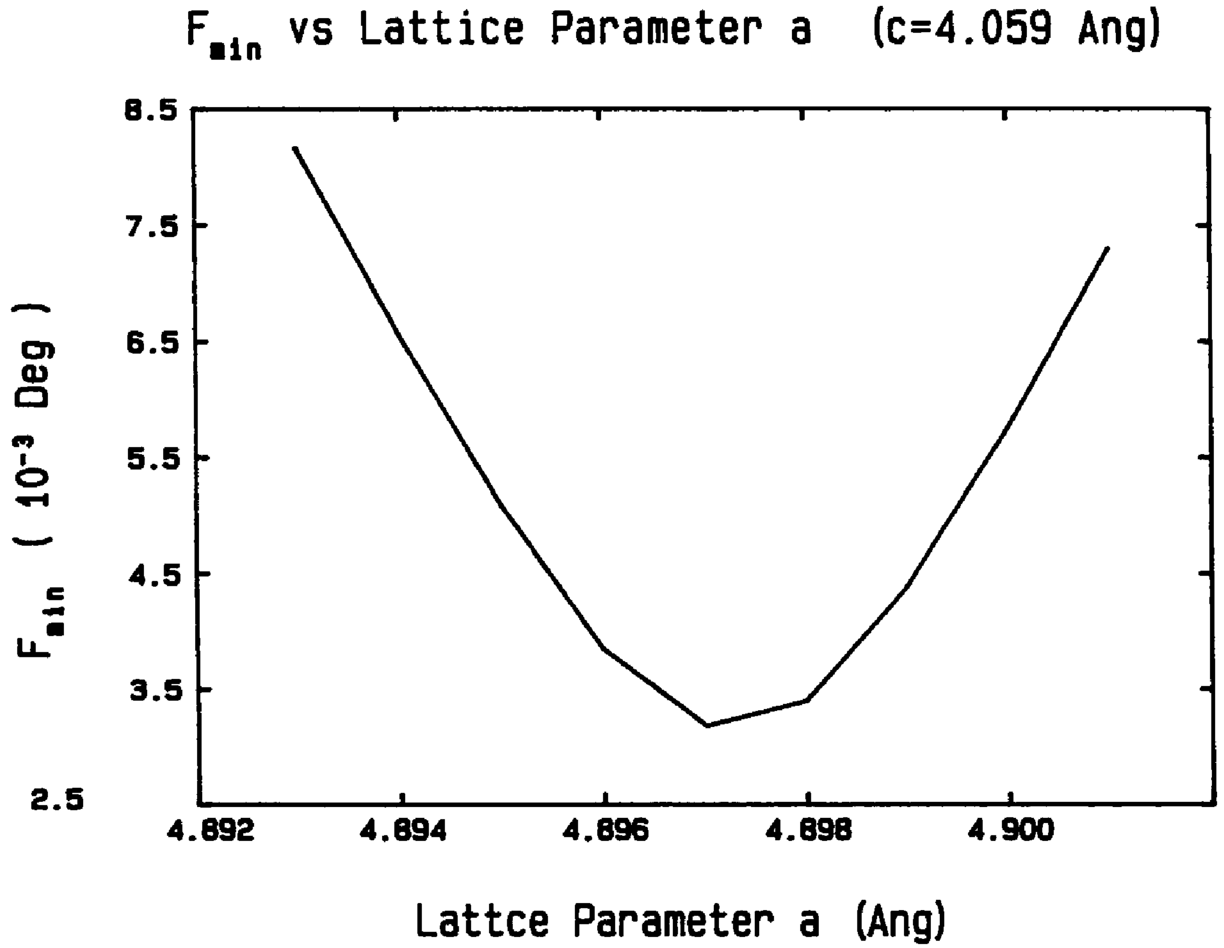

F_min vs Lattice Parameter a (c=4.059 Ang)
8.5
7.5
6.5
5.5
4.5
3.5
2.5
F_min (10^-3 Deg)
4.892
4.894
4.896
4.898
4.900
Lattce Parameter a (Ang)

Figure 10

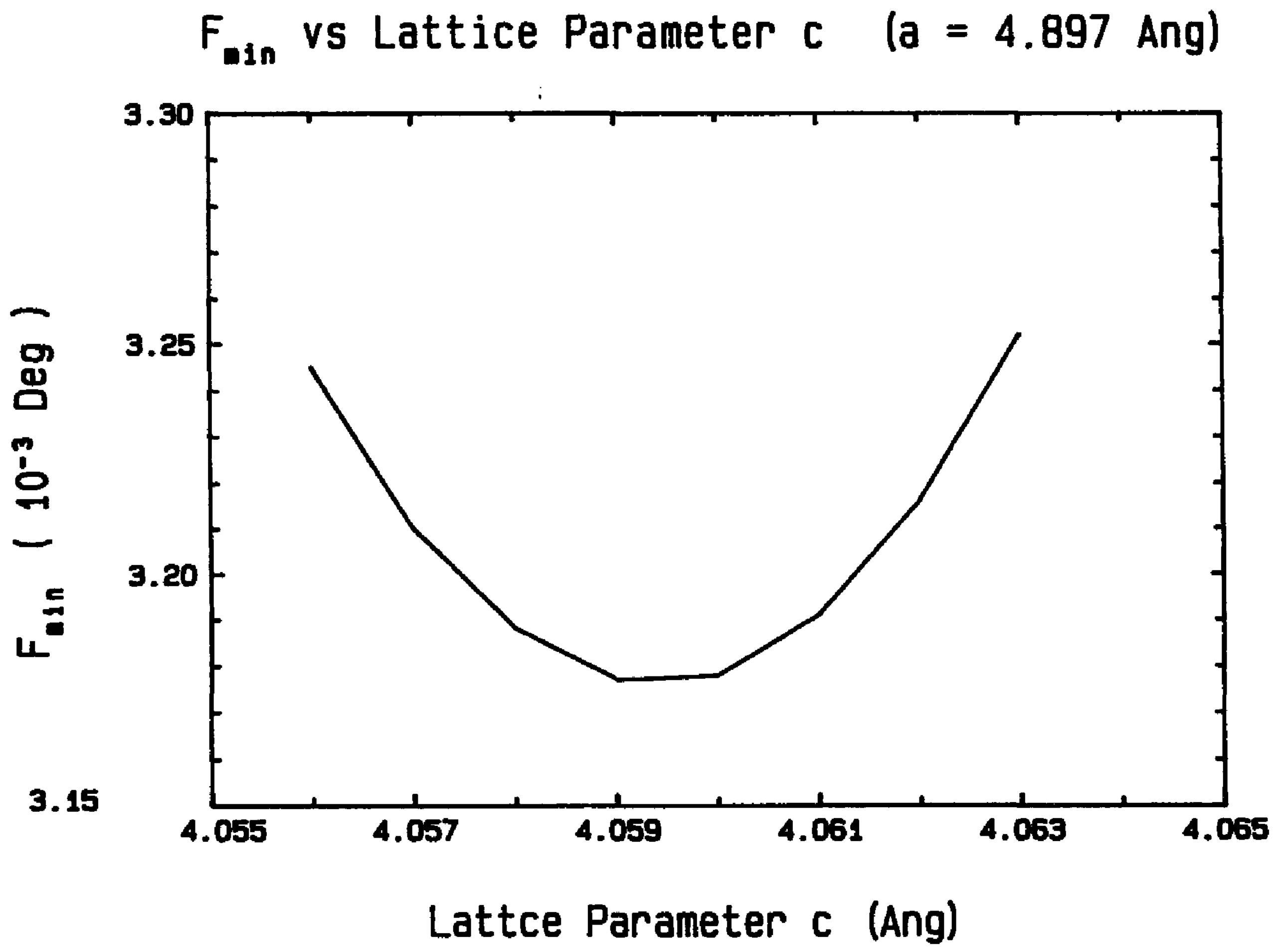
F_{min} vs Lattice Parameter c (a = 4.897 Ang)
3.30
3.25
3.20
3.15
F_{min} (10^{-3} Deg)
4.055
4.057
4.059
4.061
4.063
4.065
Lattce Parameter c (Ang)

Figure 11

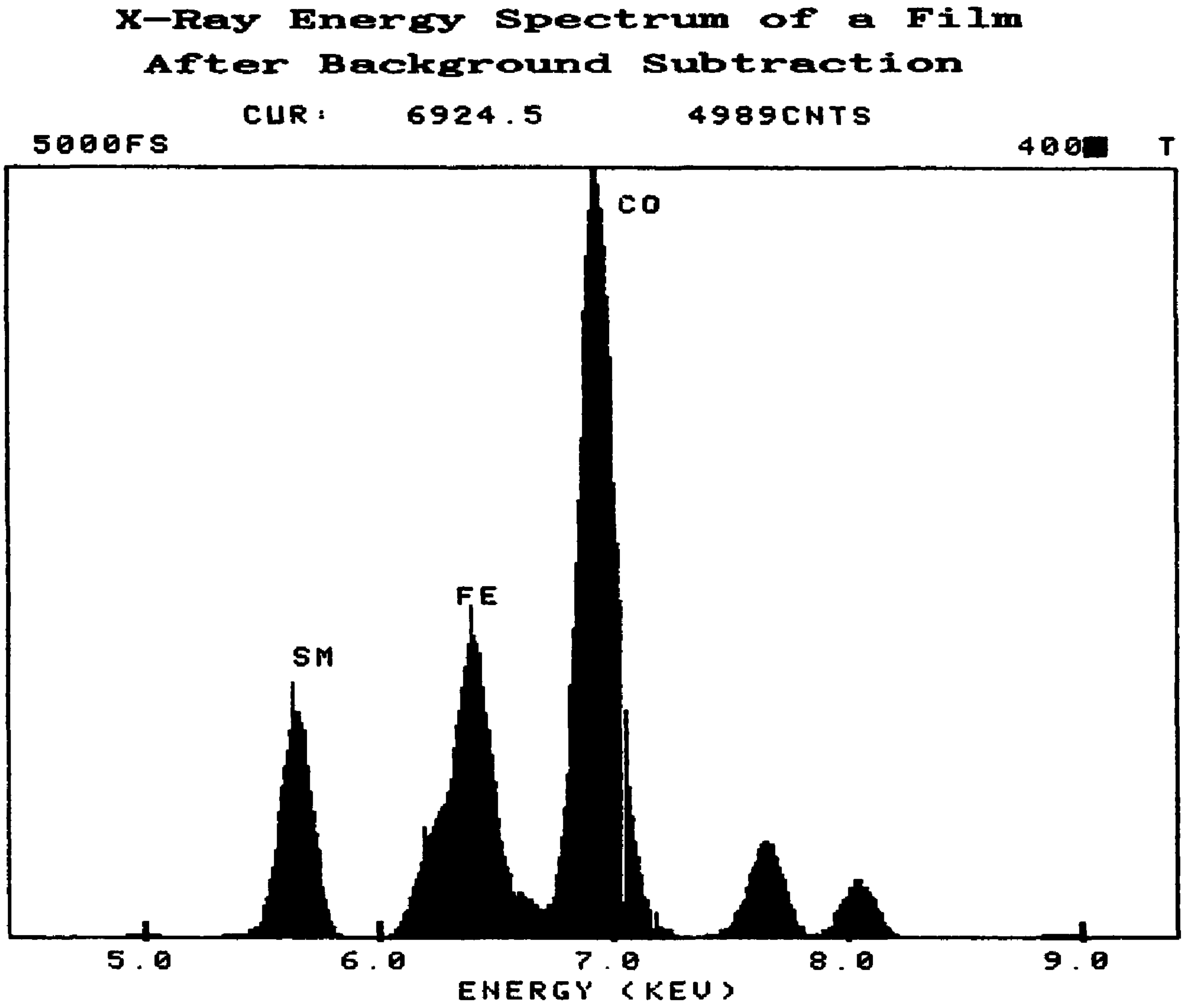
X-Ray Energy Spectrum of a Film
After Background Subtraction
CUR: 6924.5 4989CNTS
5000FS
400 T
CO
FE
SM
5.0
6.0
7.0
8.0
9.0
ENERGY (KEV)

Figure 12

X-Ray Powder Pattern of $Sm_2(CoFeCuZr)_{17}$ Target

Rhombohedral Structure

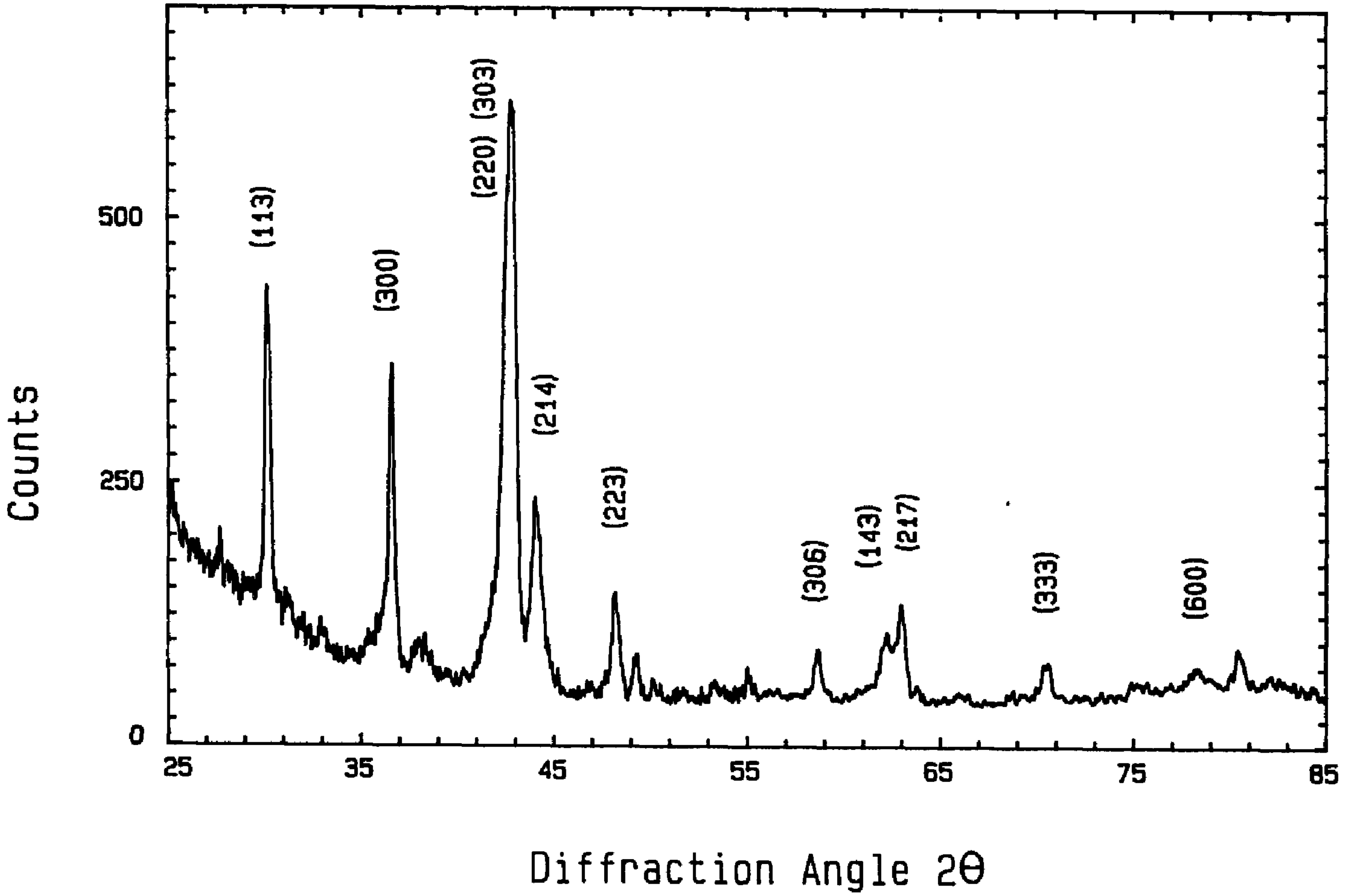

Figure 13

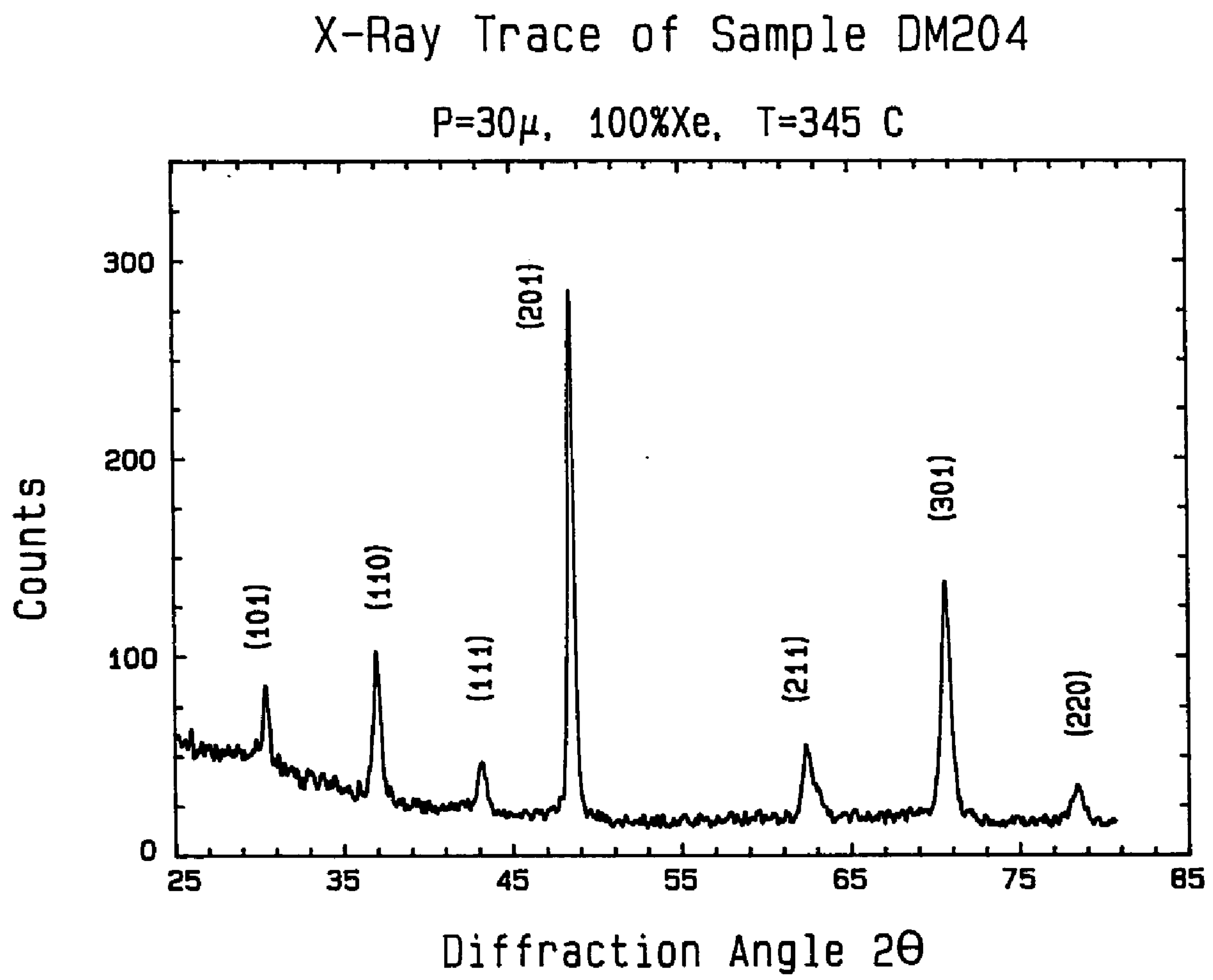
X-Ray Trace of Sample DM204
P=30μ, 100%Xe, T=345 C
Counts
0
100
200
300
25
35
45
55
65
75
85
Diffraction Angle 2Θ
(101)
(110)
(111)
(201)
(211)
(301)
(220)

Figure 14

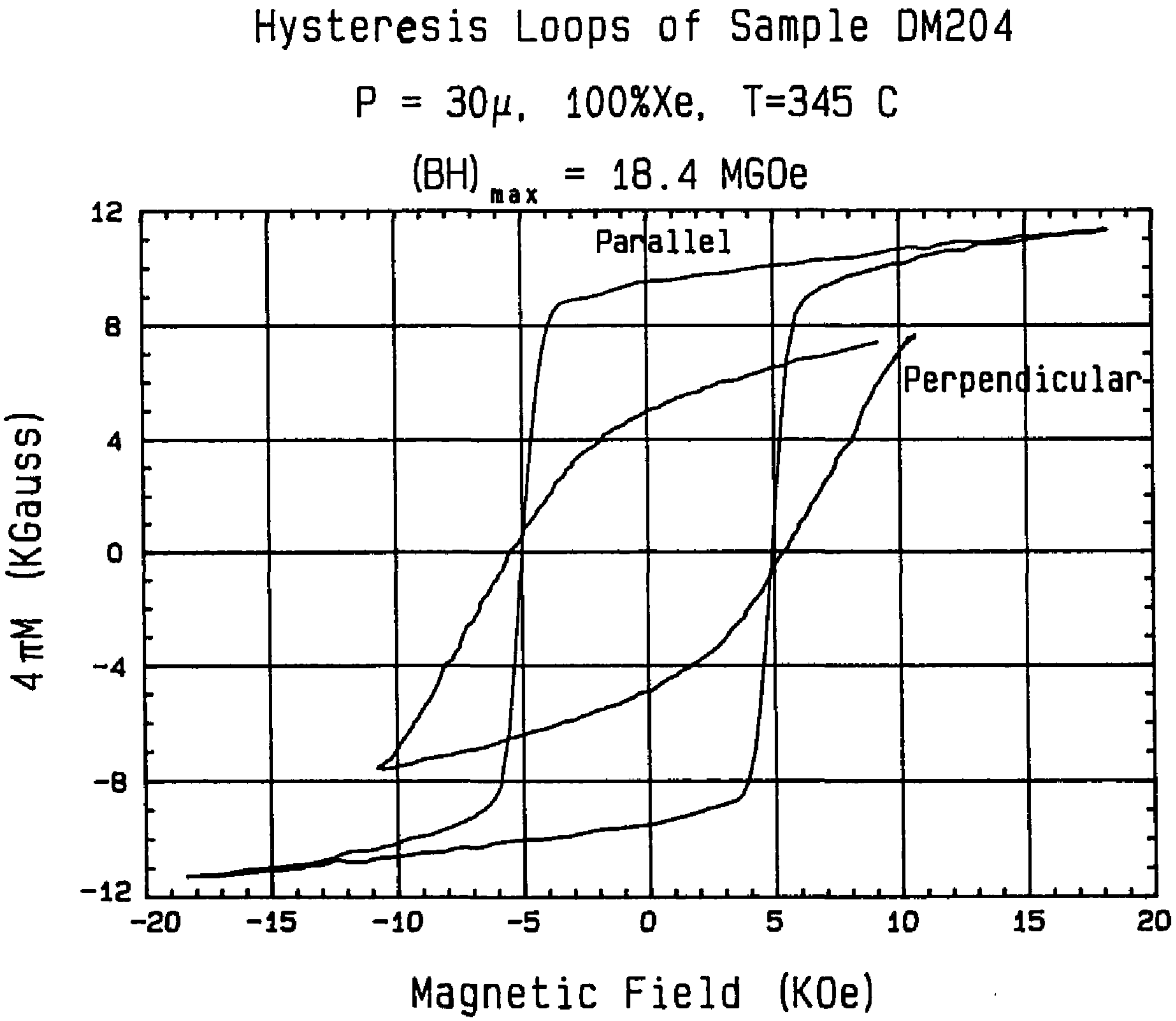
Hysteresis Loops of Sample DM204
P = 30μ, 100%Xe, T=345 C
(BH)max = 18.4 MGOe
Parallel
Perpendicular
4πM (KGauss)
12
8
4
0
-4
-8
-12
-20
-15
-10
-5
0
5
10
15
20
Magnetic Field (KOe)

Figure 15

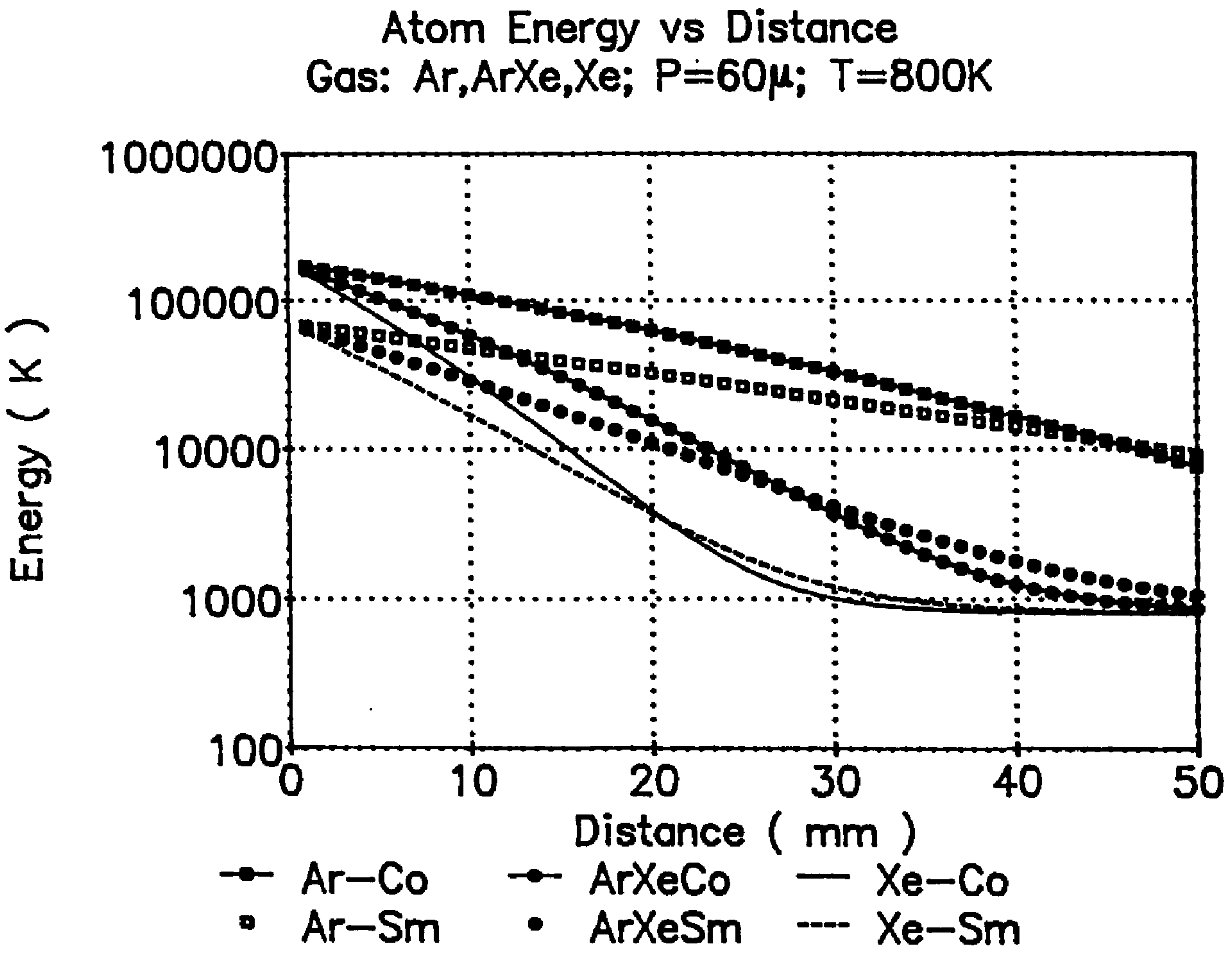
Atom Energy vs Distance
Gas: Ar,ArXe,Xe; P=60μ; T=800K
1000000
100000
10000
1000
100
Energy (K)
0
10
20
30
40
50
Distance (mm)
Ar–Co
ArXeCo
Xe–Co
Ar–Sm
ArXeSm
Xe–Sm

Figure 16

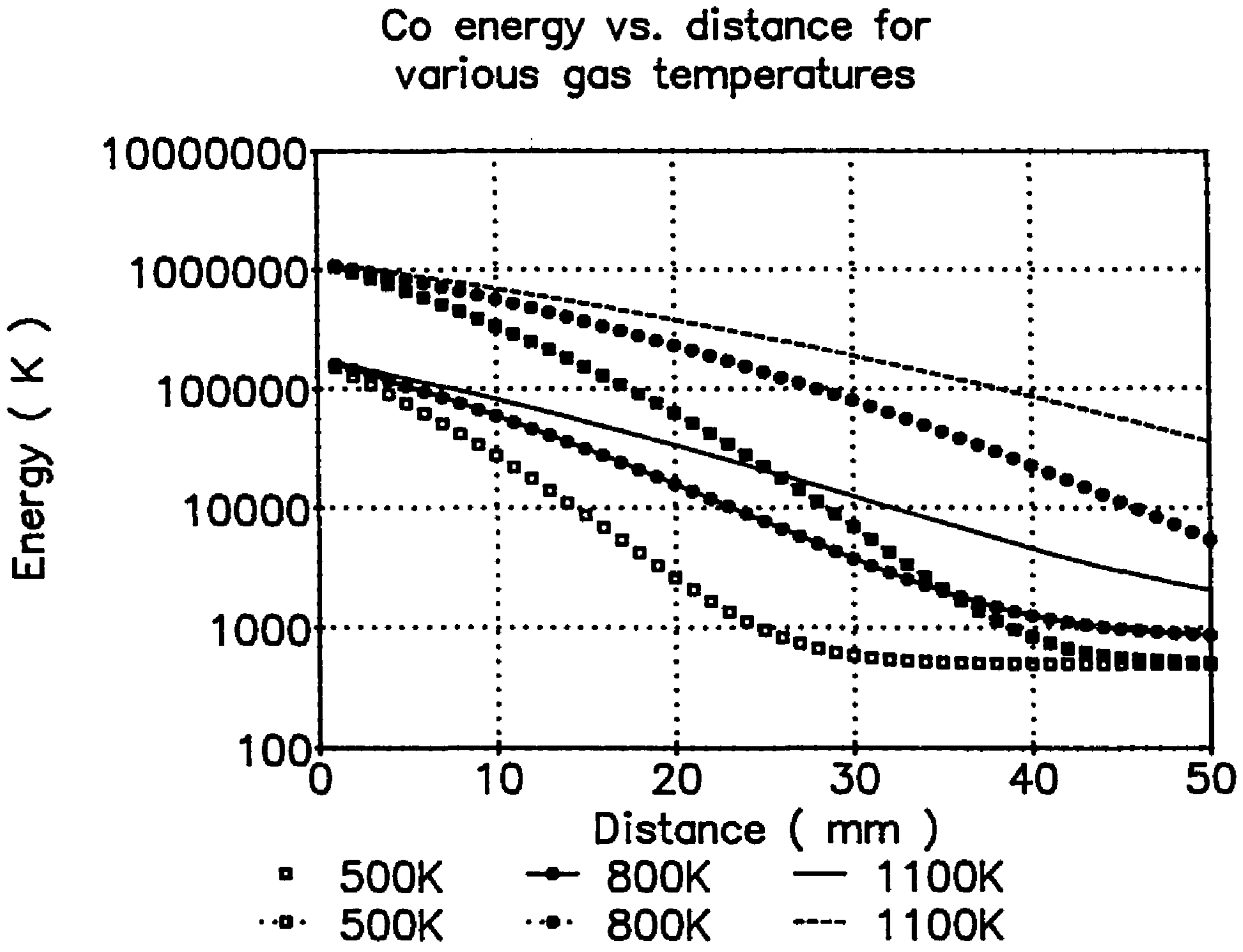
Co energy vs. distance for various gas temperatures
10000000
1000000
100000
10000
1000
100
Energy (K)
0
10
20
30
40
50
Distance (mm)
500K
800K
1100K
500K
800K
1100K

Figure 17

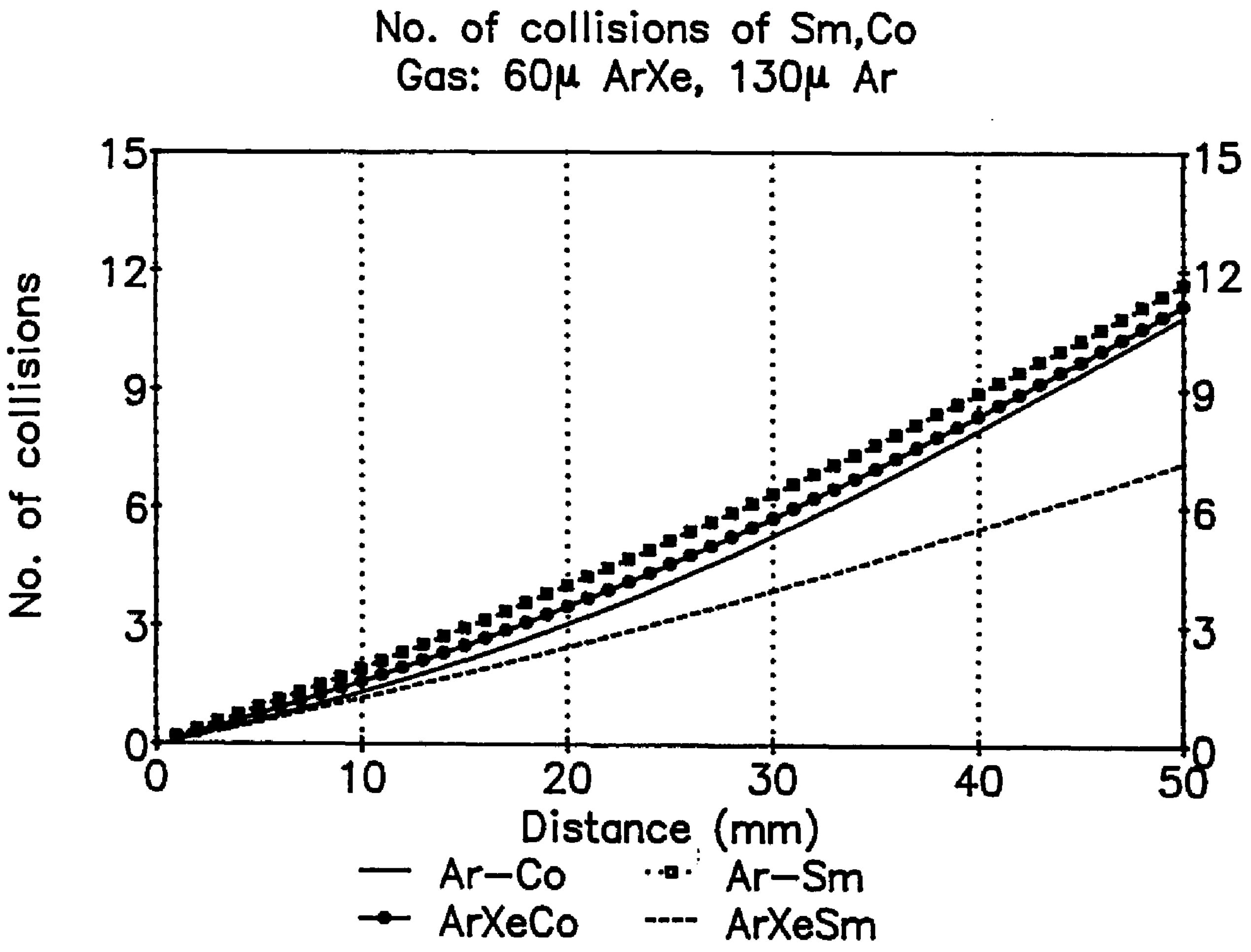
No. of collisions of Sm,Co
Gas: 60μ ArXe, 130μ Ar
No. of collisions
0
3
6
9
12
15
0
10
20
30
40
50
Distance (mm)
Ar–Co
Ar–Sm
ArXeCo
ArXeSm

Figure 18

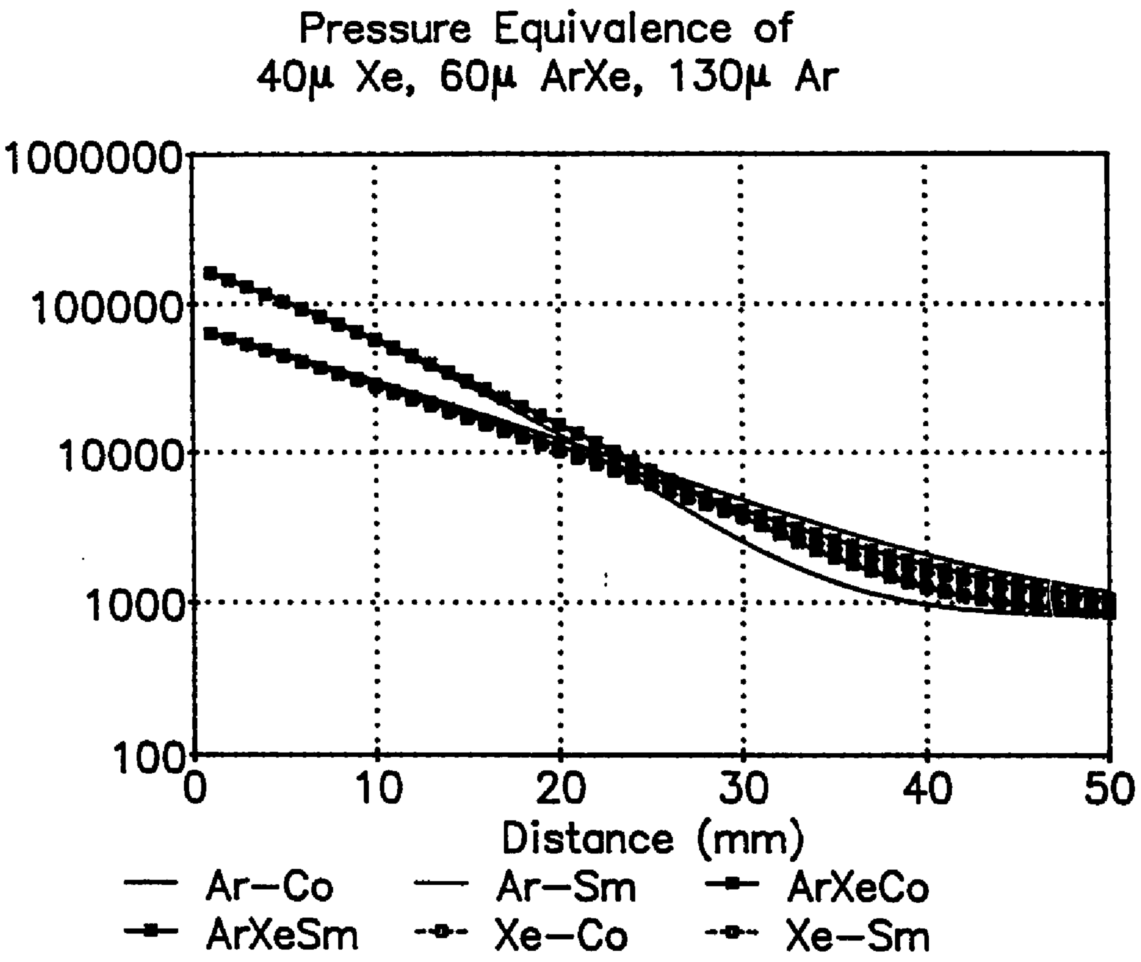
Pressure Equivalence of
40µ Xe, 60µ ArXe, 130µ Ar
Energy (K)
1000000
100000
10000
1000
100
0
10
20
30
40
50
Distance (mm)
Ar–Co
Ar–Sm
ArXeCo
ArXeSm
Xe–Co
Xe–Sm

Figure 19

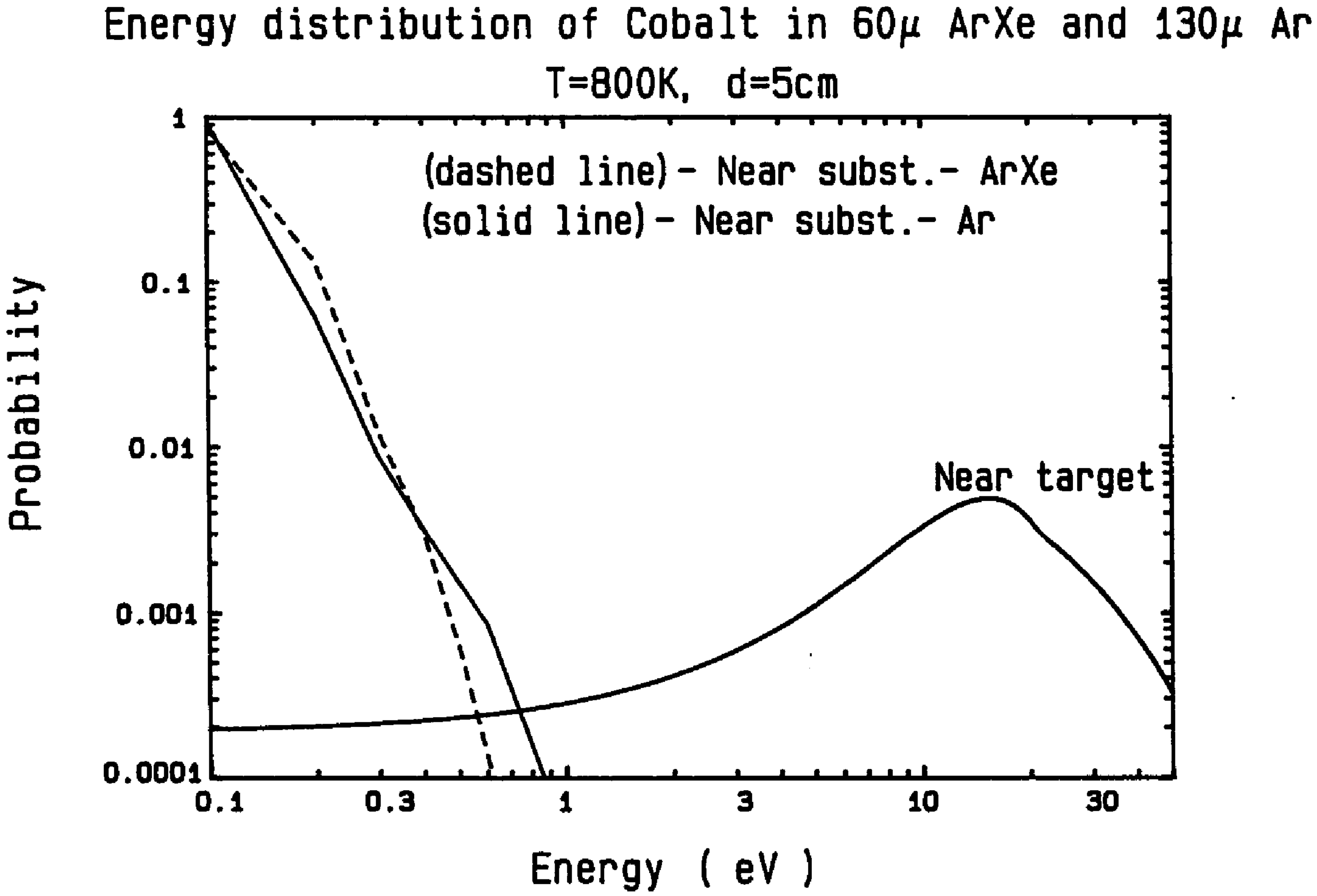
Energy distribution of Cobalt in 60μ ArXe and 130μ Ar
T=800K, d=5cm
(dashed line) - Near subst.- ArXe
(solid line) - Near subst.- Ar
Near target
Probability
1
0.1
0.01
0.001
0.0001
0.1
0.3
1
3
10
30
Energy (eV)

Figure 20(a)

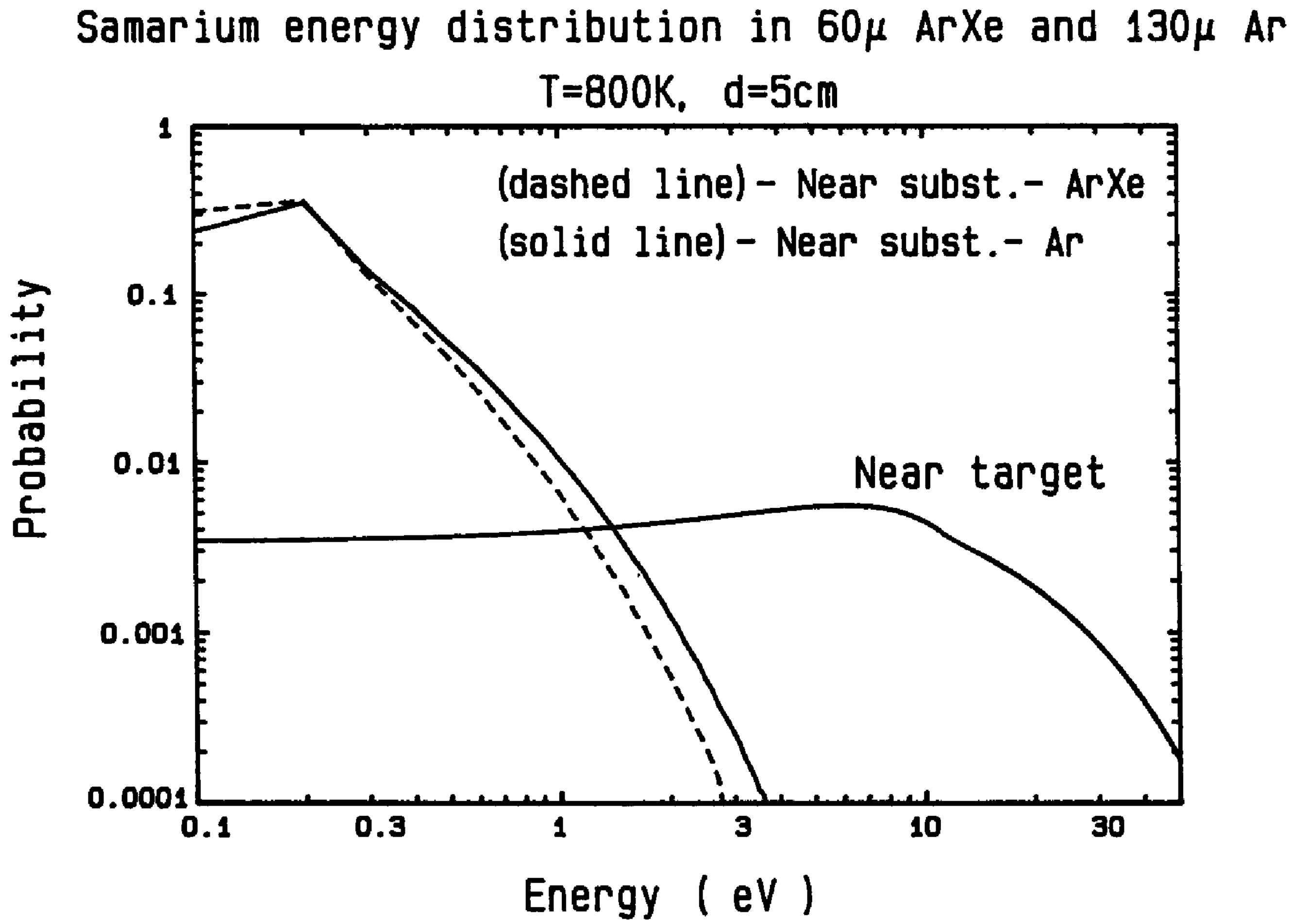

Samarium energy distribution in 60μ ArXe and 130μ Ar
T=800K, d=5cm
(dashed line) - Near subst.- ArXe
(solid line) - Near subst.- Ar
Near target
Probability
1
0.1
0.01
0.001
0.0001
0.1
0.3
1
3
10
30
Energy (eV)

Figure 20(b)

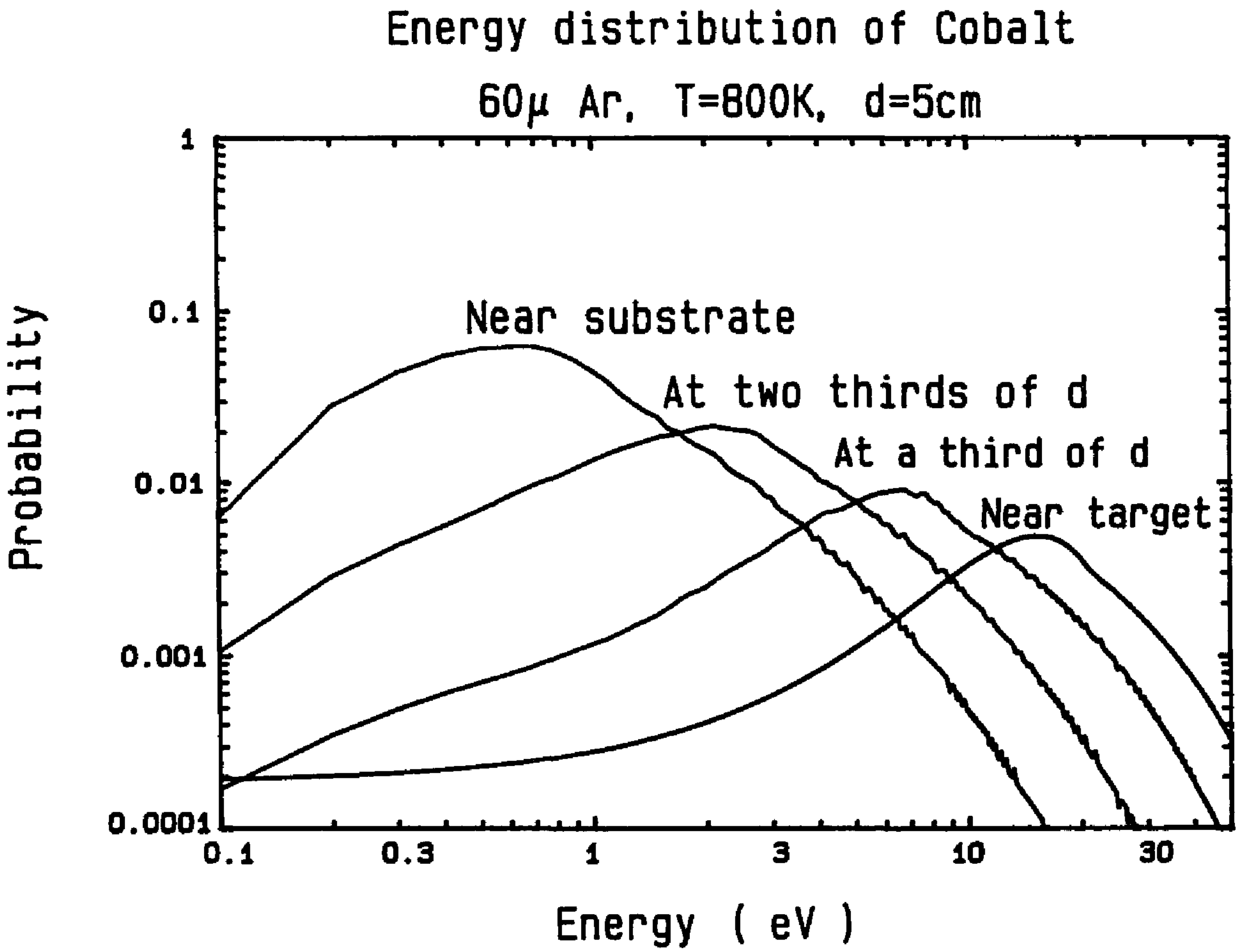
Energy distribution of Cobalt
60μ Ar, T=800K, d=5cm
Probability
1
0.1
0.01
0.001
0.0001
0.1
0.3
1
3
10
30
Energy (eV)
Near substrate
At two thirds of d
At a third of d
Near target

Figure 21(a)

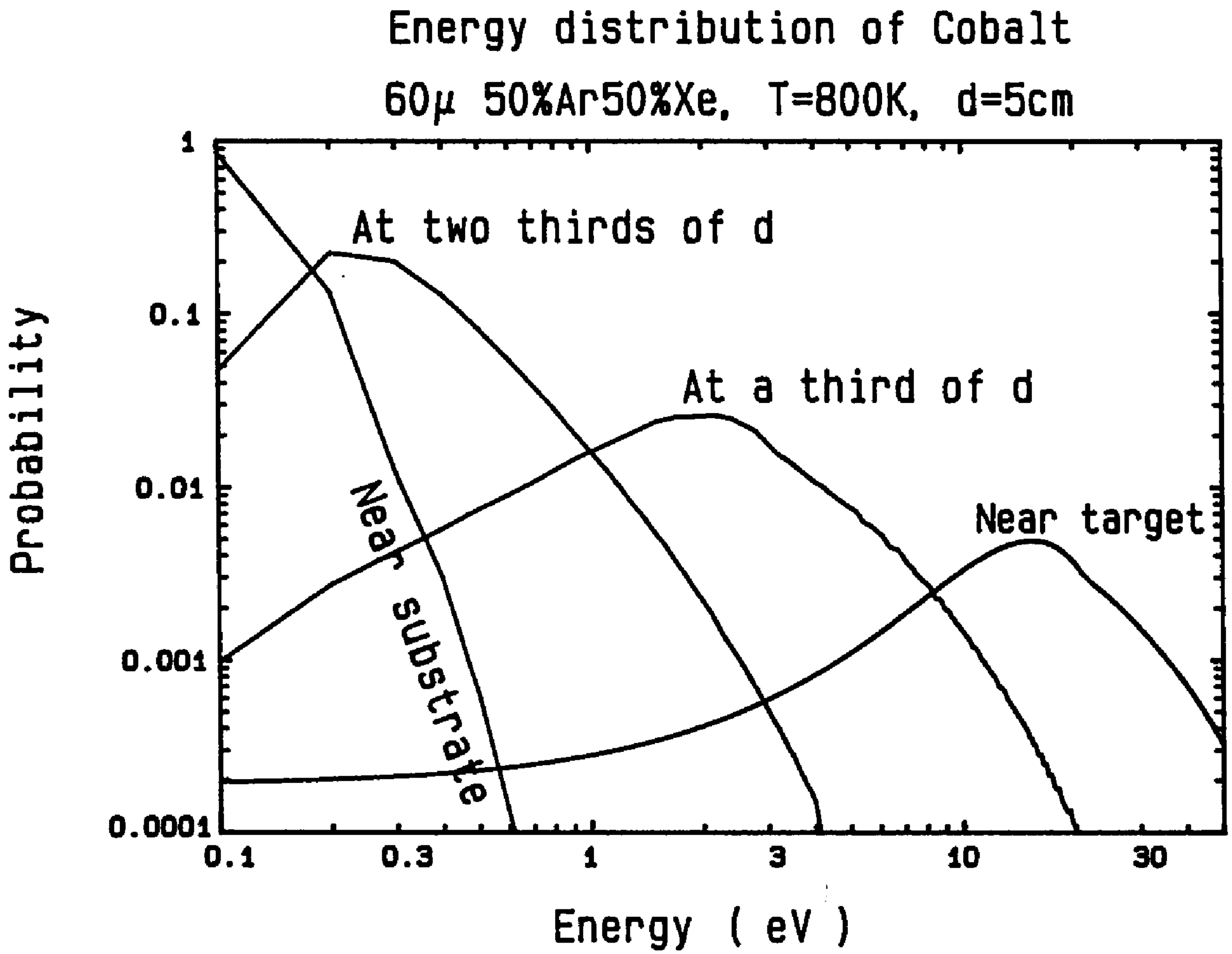
Energy distribution of Cobalt
60μ 50%Ar50%Xe, T=800K, d=5cm
Probability
1
0.1
0.01
0.001
0.0001
0.1
0.3
1
3
10
30
Energy (eV)
At two thirds of d
At a third of d
Near target
Near substrate

Figure 21(b)

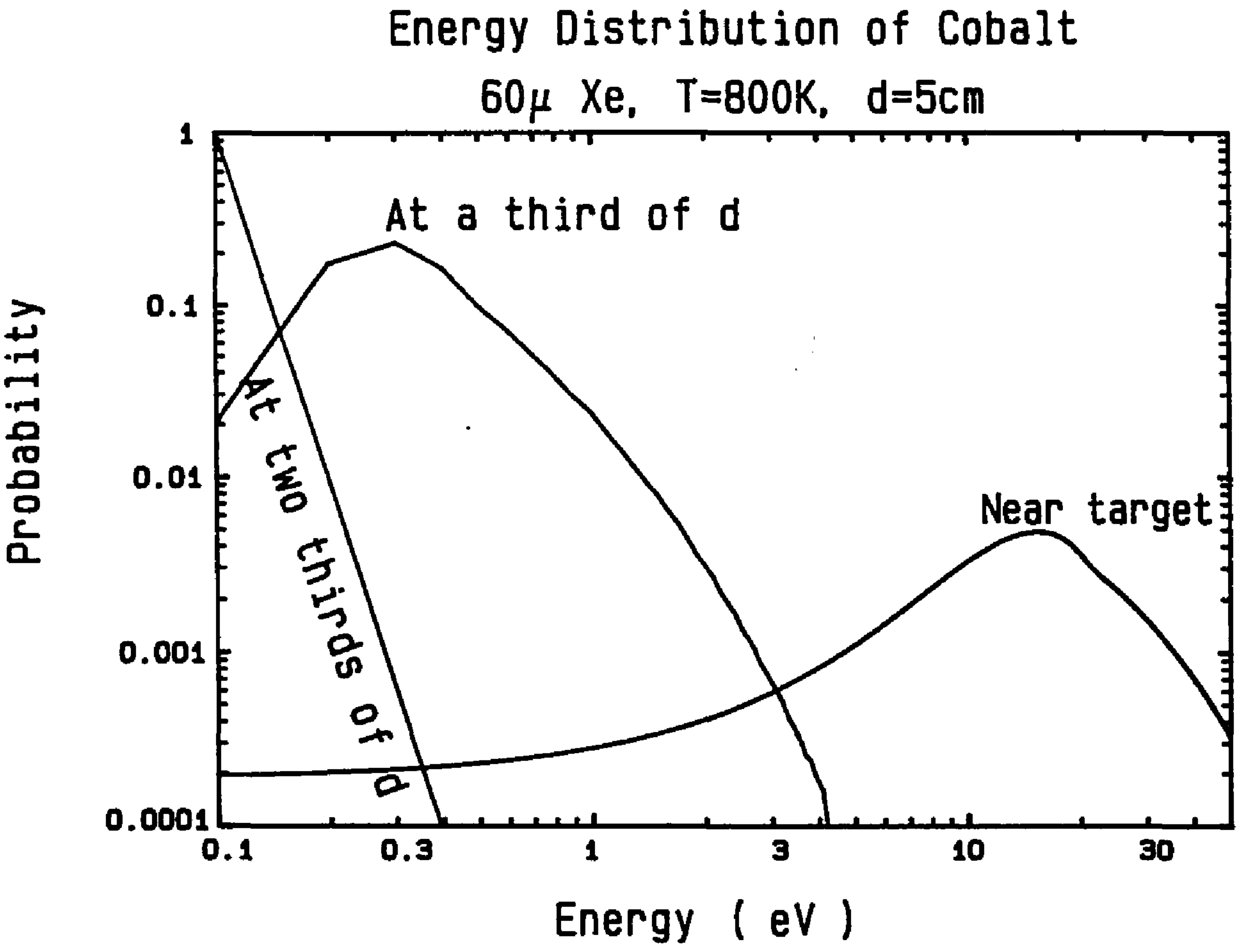
Energy Distribution of Cobalt
60μ Xe, T=800K, d=5cm
At a third of d
At two thirds of d
Near target
Probability
1
0.1
0.01
0.001
0.0001
0.1
0.3
1
3
10
30
Energy (eV)

Figure 21(c)

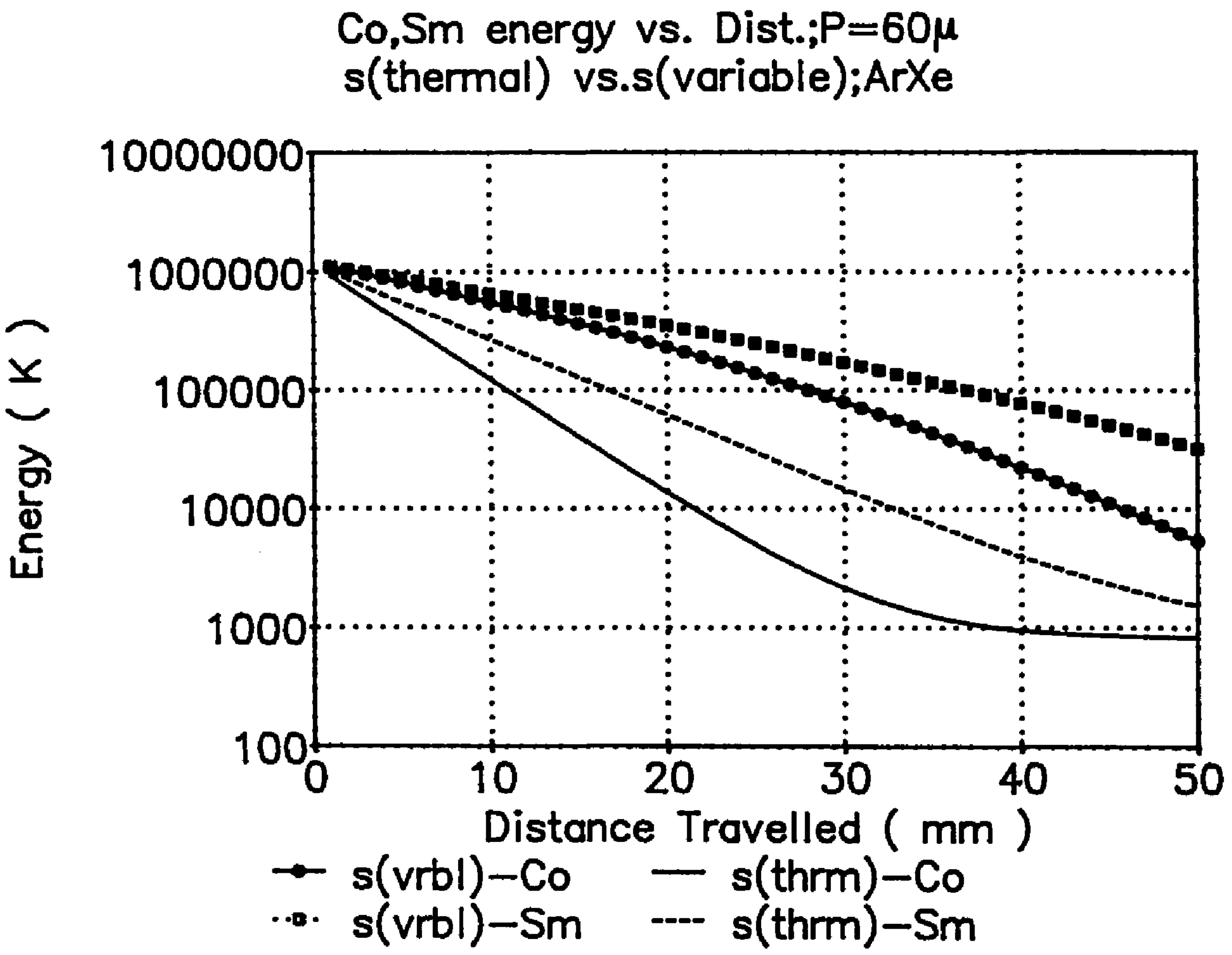
Co,Sm energy vs. Dist.;P=60μ
s(thermal) vs.s(variable);ArXe
Energy (K)
10000000
1000000
100000
10000
1000
100
0
10
20
30
40
50
Distance Travelled (mm)
s(vrbl)–Co
s(vrbl)–Sm
s(thrm)–Co
s(thrm)–Sm

Figure 22(a)

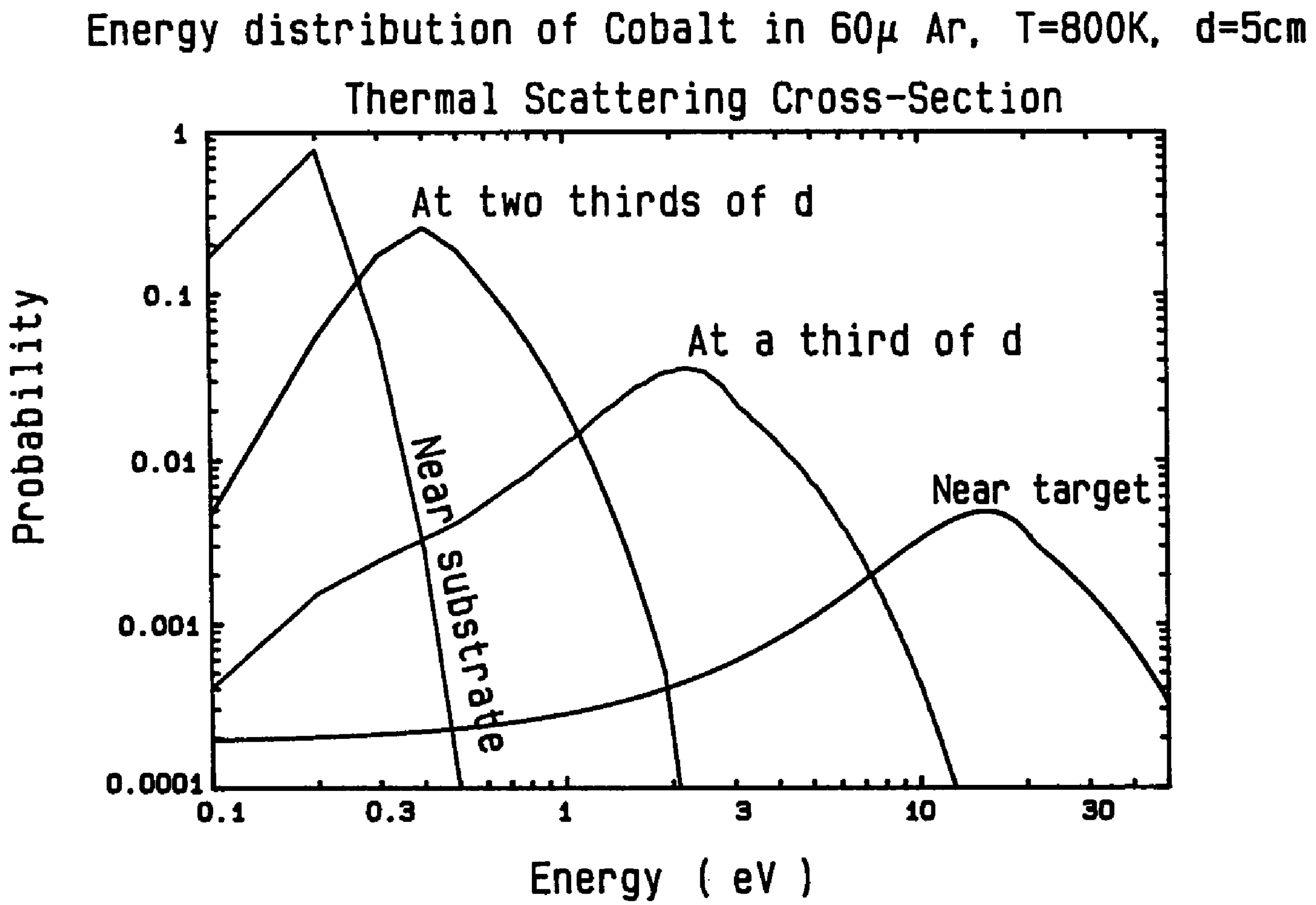
Energy distribution of Cobalt in 60μ Ar, T=800K, d=5cm

Thermal Scattering Cross-Section

Figure 22(b)

Figure 23

RENORMALIZATION PROCEDURE

WINDOW SIZE 0.1eV

Initial Distribution		Distribution at 34mm			
Energy Window	Prob. x100	Modified Energy Window	Modified Prob. x100	Prob. for 0.1eV Wind. x100	New Energy Window
≈ 2.1 ≈ 14.9	≈ 0.0432 ≈ 0.4881	≈ 2.088	≈ 0.4472		
15.0	0.4886	2.109	0.4485	2.253	2.1
15.1	0.4890	2.130	0.4496		
15.2	0.4892	2.151	0.4507		
15.3	0.4893	2.173	0.4516		
15.4	0.4892	2.194	0.4523		
15.5	0.4891	2.215	0.4530	2.240	2.2
15.6	0.4888	2.237	0.4535		
15.7	0.4883	2.258	0.4539		

Modified Probability = N * Initial Probability / $(2\theta/\pi)$
where N = 1 / Σ(Modified Probability)

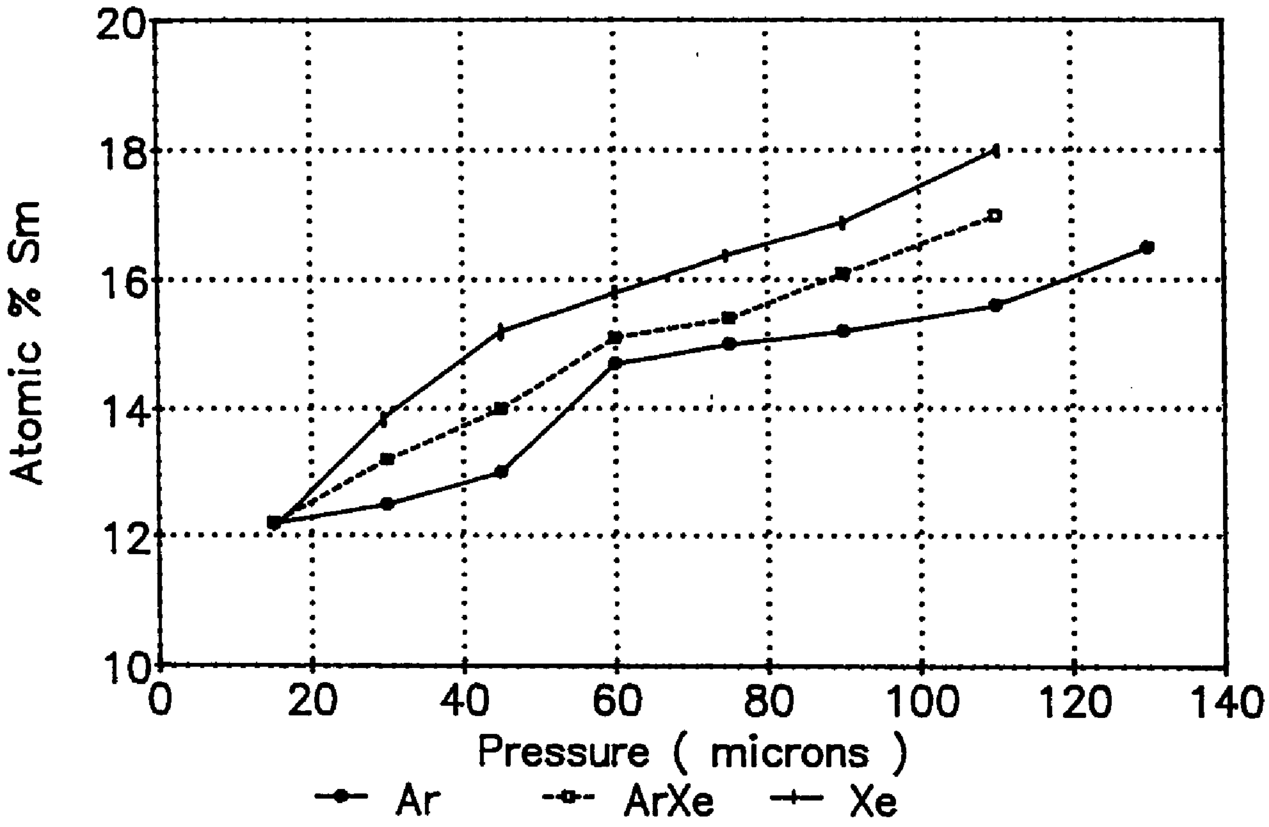

Sm content vs Pressure for
Ar, ArXe and Xe; Sbst.Temp.345C

Figure 24

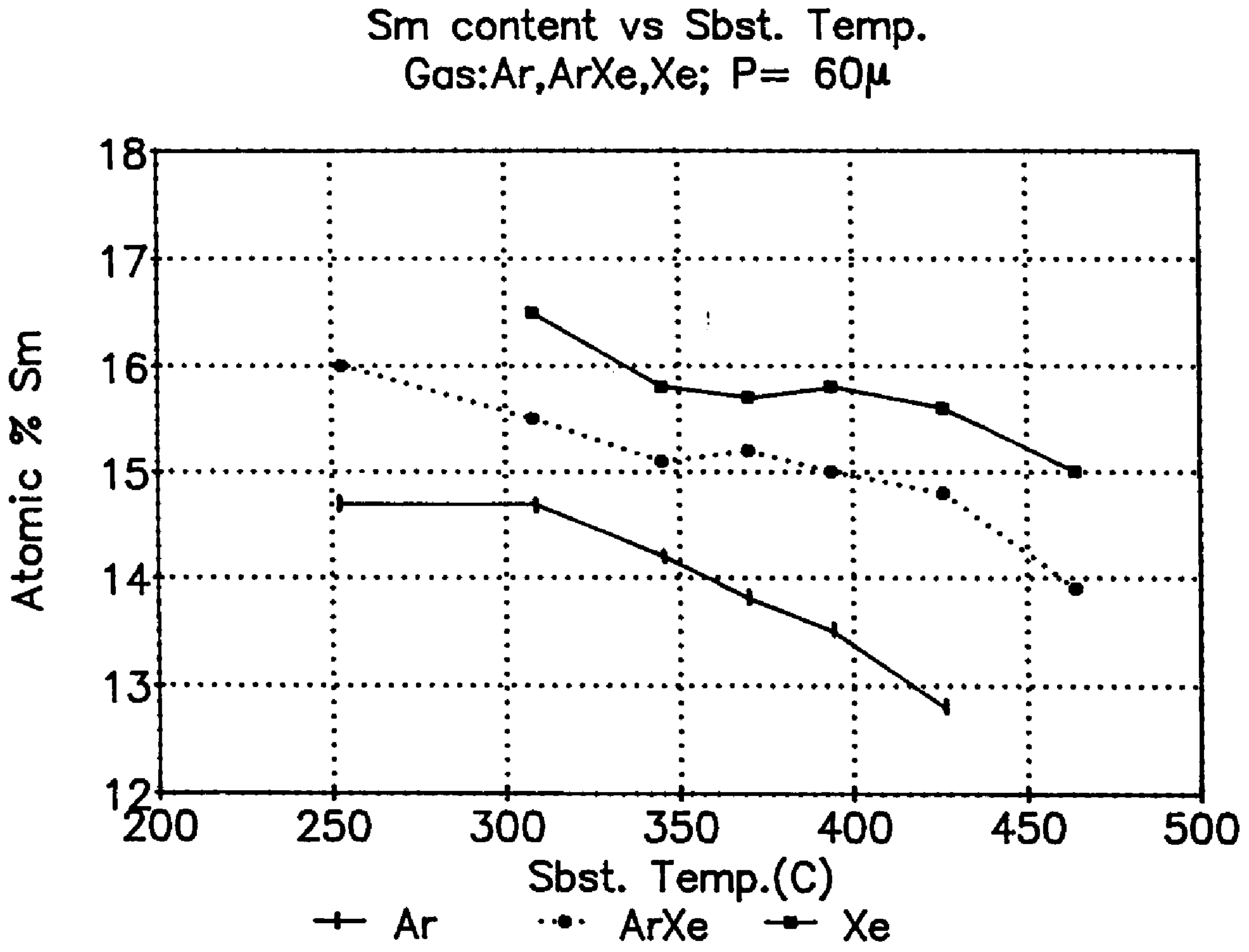
Sm content vs Sbst. Temp.
Gas:Ar,ArXe,Xe; P= 60µ
18
17
16
15
14
13
12
200
250
300
350
400
450
500
Atomic % Sm
Sbst. Temp.(C)
Ar
ArXe
Xe

Figure 25

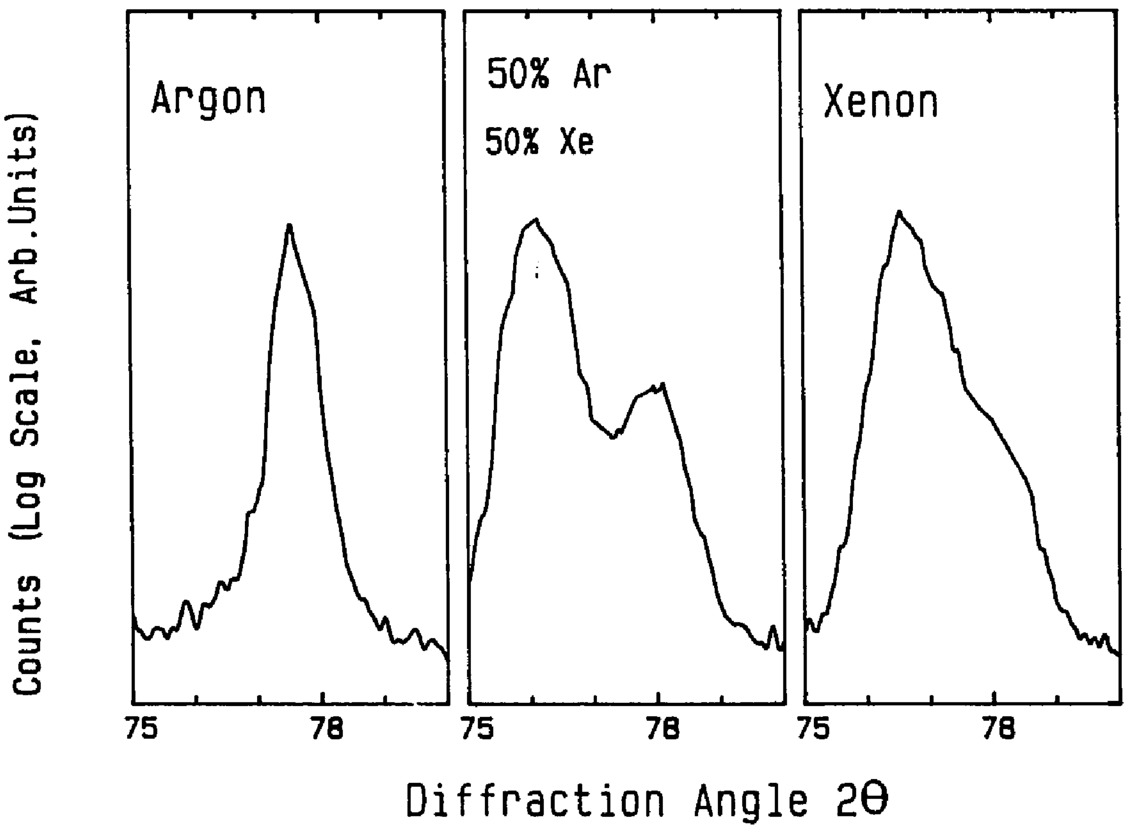

High Angle X-Ray Peaks of Samples Sputtered Using Different Gas Species

P = 90μ, T=345 C

Figure 26

Figure 27

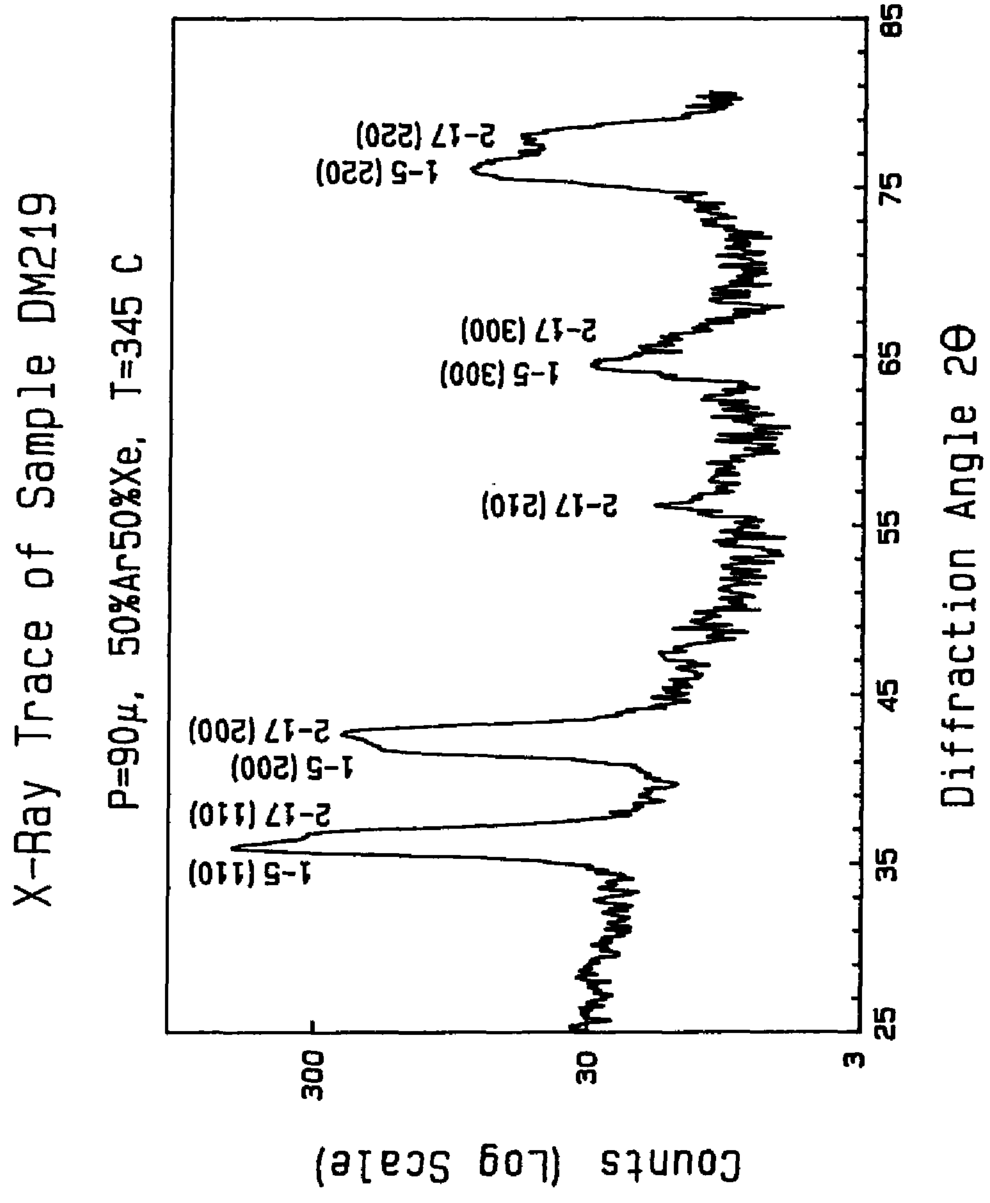
X-Ray Trace of Sample DM219
P=90μ, 50%Ar50%Xe, T=345 C
Counts (Log Scale)
3
30
300
Diffraction Angle 2Θ
25
35
45
55
65
75
85
1-5 (110)
2-17 (110)
1-5 (200)
2-17 (200)
2-17 (210)
1-5 (300)
2-17 (300)
1-5 (220)
2-17 (220)

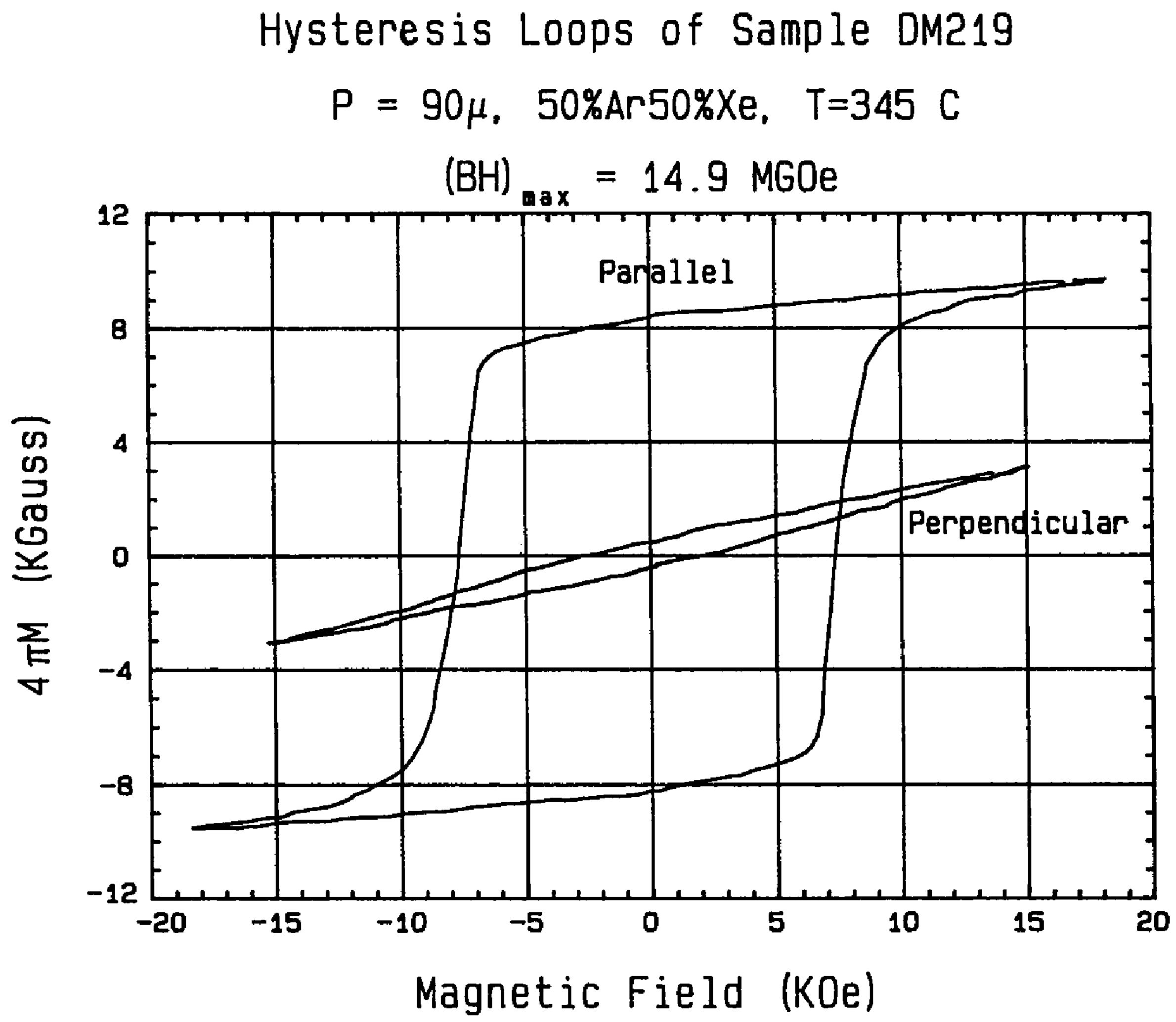
Hysteresis Loops of Sample DM219
P = 90μ, 50%Ar50%Xe, T=345 C
(BH)max = 14.9 MGOe
Parallel
Perpendicular
4πM (KGauss)
12
8
4
0
-4
-8
-12
-20
-15
-10
-5
0
5
10
15
20
Magnetic Field (KOe)

Figure 28

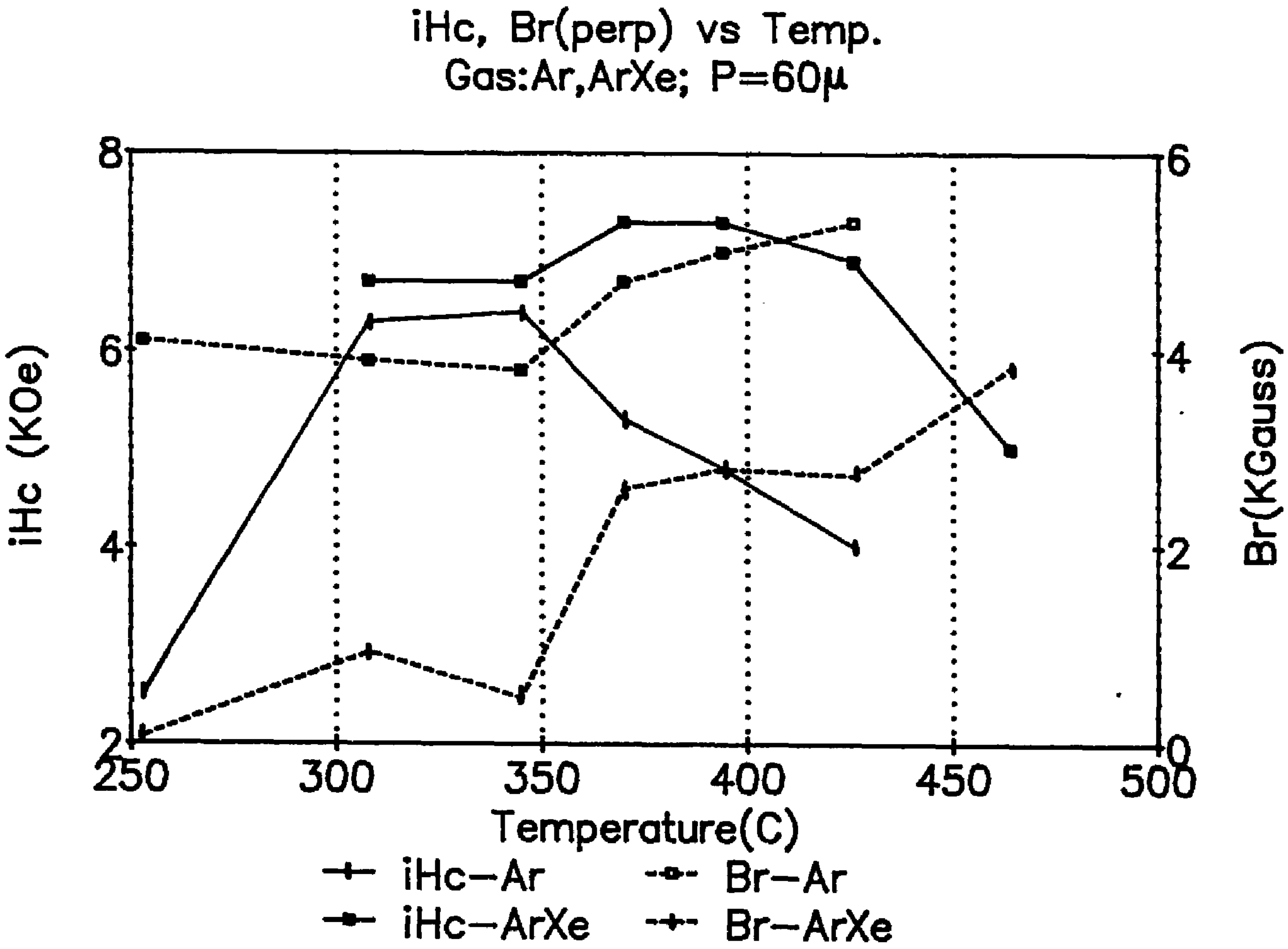
iHc, Br(perp) vs Temp.
Gas:Ar,ArXe; P=60μ
iHc (KOe)
Br(KGauss)
Temperature(C)
2
4
6
8
0
2
4
6
250
300
350
400
450
500
iHc–Ar
iHc–ArXe
Br–Ar
Br–ArXe

Figure 29

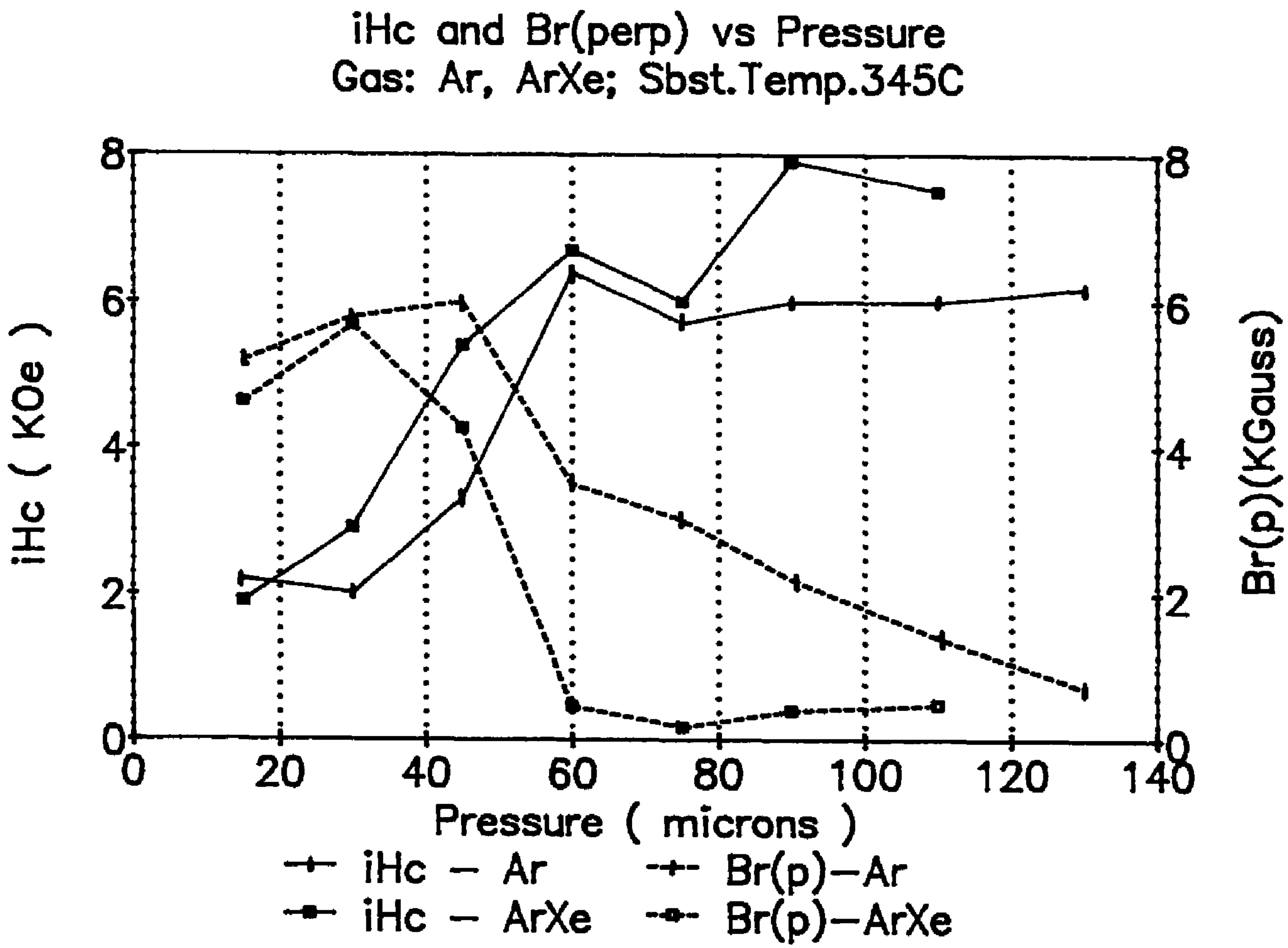
iHc and Br(perp) vs Pressure
Gas: Ar, ArXe; Sbst.Temp.345C
iHc (KOe)
Br(p)(KGauss)
0
2
4
6
8
0
20
40
60
80
100
120
140
Pressure (microns)
iHc – Ar
iHc – ArXe
Br(p)–Ar
Br(p)–ArXe

Figure 30

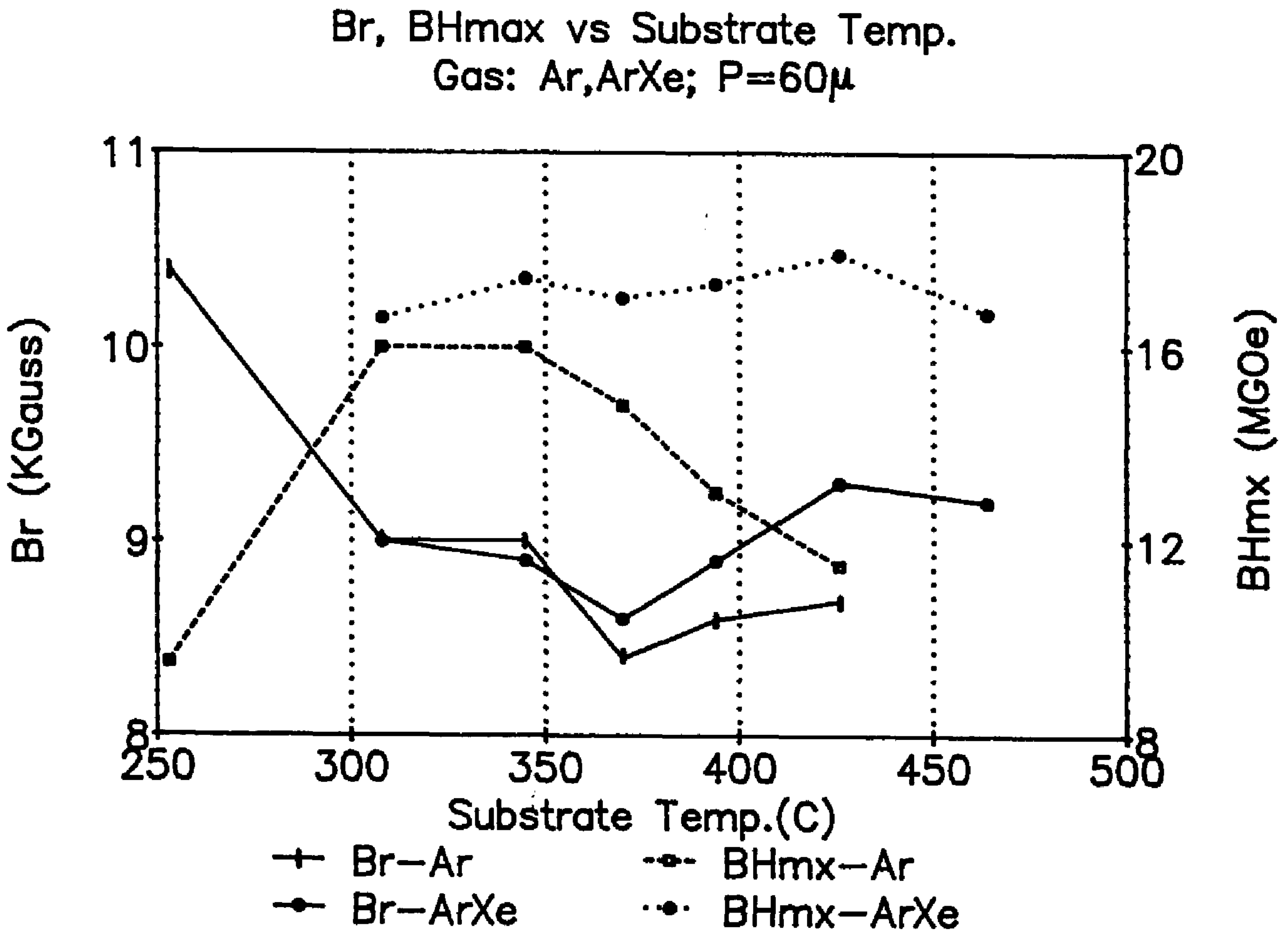
Br, BHmax vs Substrate Temp.
Gas: Ar,ArXe; P=60μ
Br (KGauss)
8
9
10
11
BHmx (MGOe)
8
12
16
20
250
300
350
400
450
500
Substrate Temp.(C)
Br–Ar
Br–ArXe
BHmx–Ar
BHmx–ArXe

Figure 31

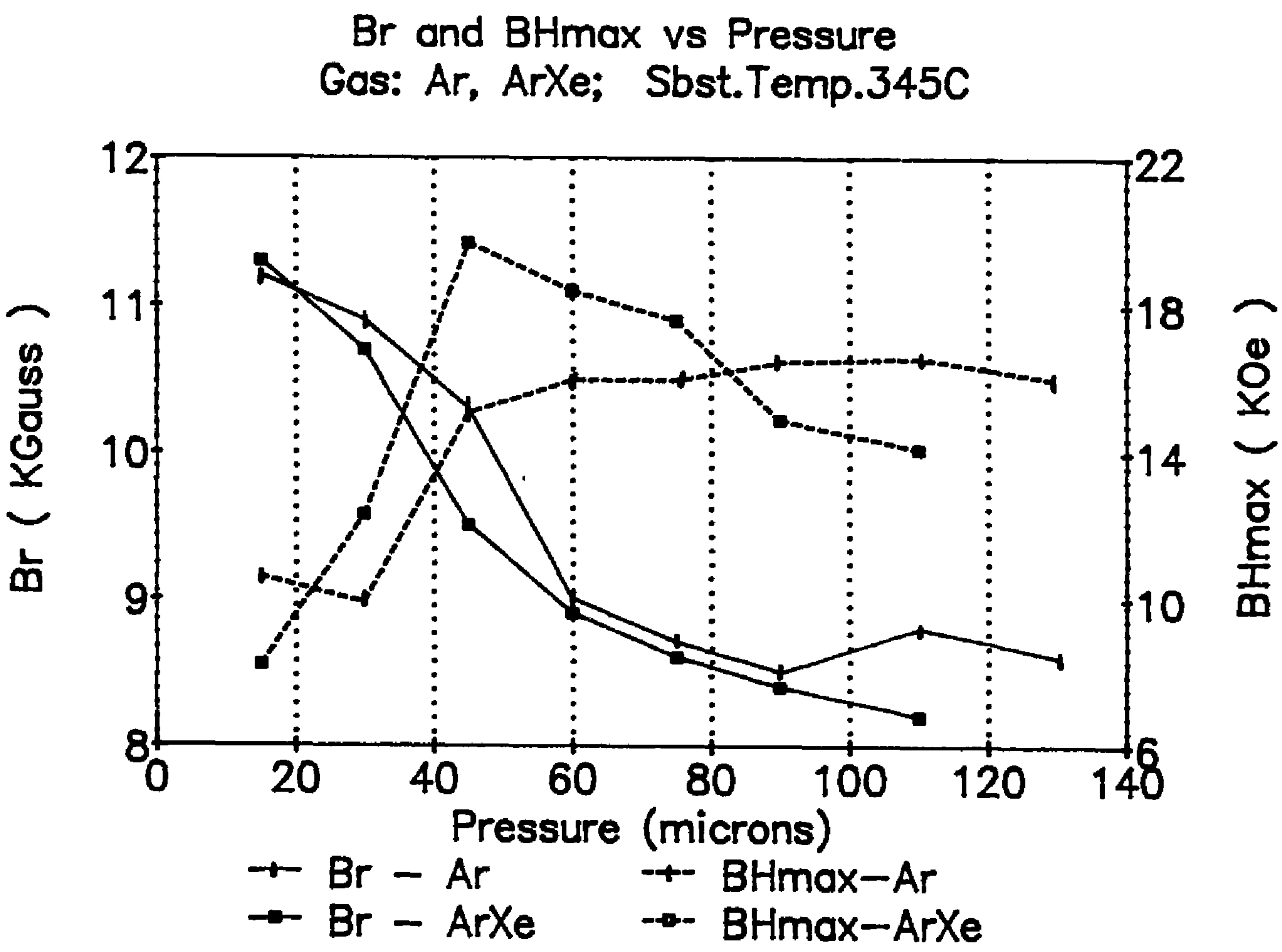
Br and BHmax vs Pressure
Gas: Ar, ArXe; Sbst.Temp.345C
Br (KGauss)
12
11
10
9
8
BHmax (KOe)
22
18
14
10
6
0
20
40
60
80
100
120
140
Pressure (microns)
Br – Ar
Br – ArXe
BHmax–Ar
BHmax–ArXe

Figure 32

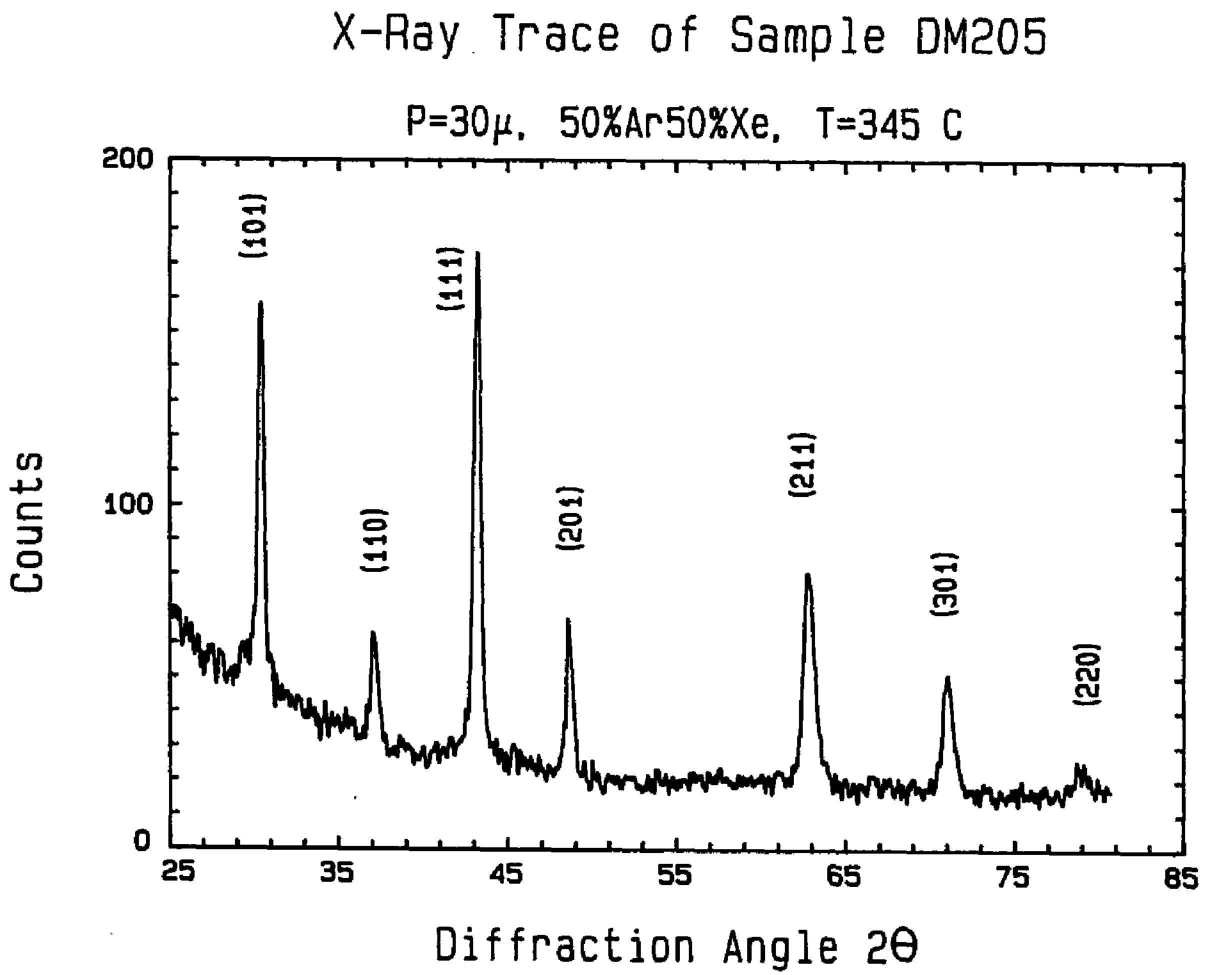
X-Ray Trace of Sample DM205

P=30μ, 50%Ar50%Xe, T=345 C

Figure 33

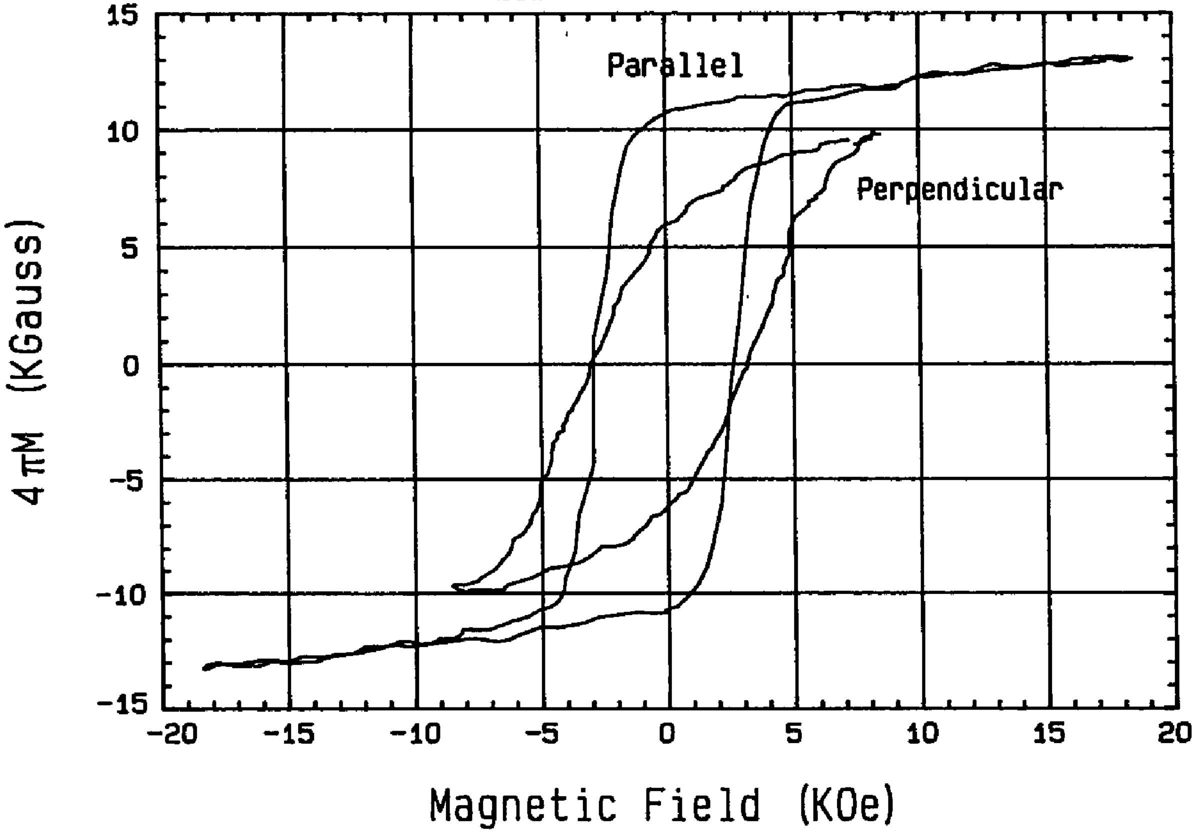

Hysteresis Loops of Sample DM205

P = 30μ, 50%Ar50%Xe, T=345 C

$(BH)_{max}$ = 12.3 MGOe

Figure 34

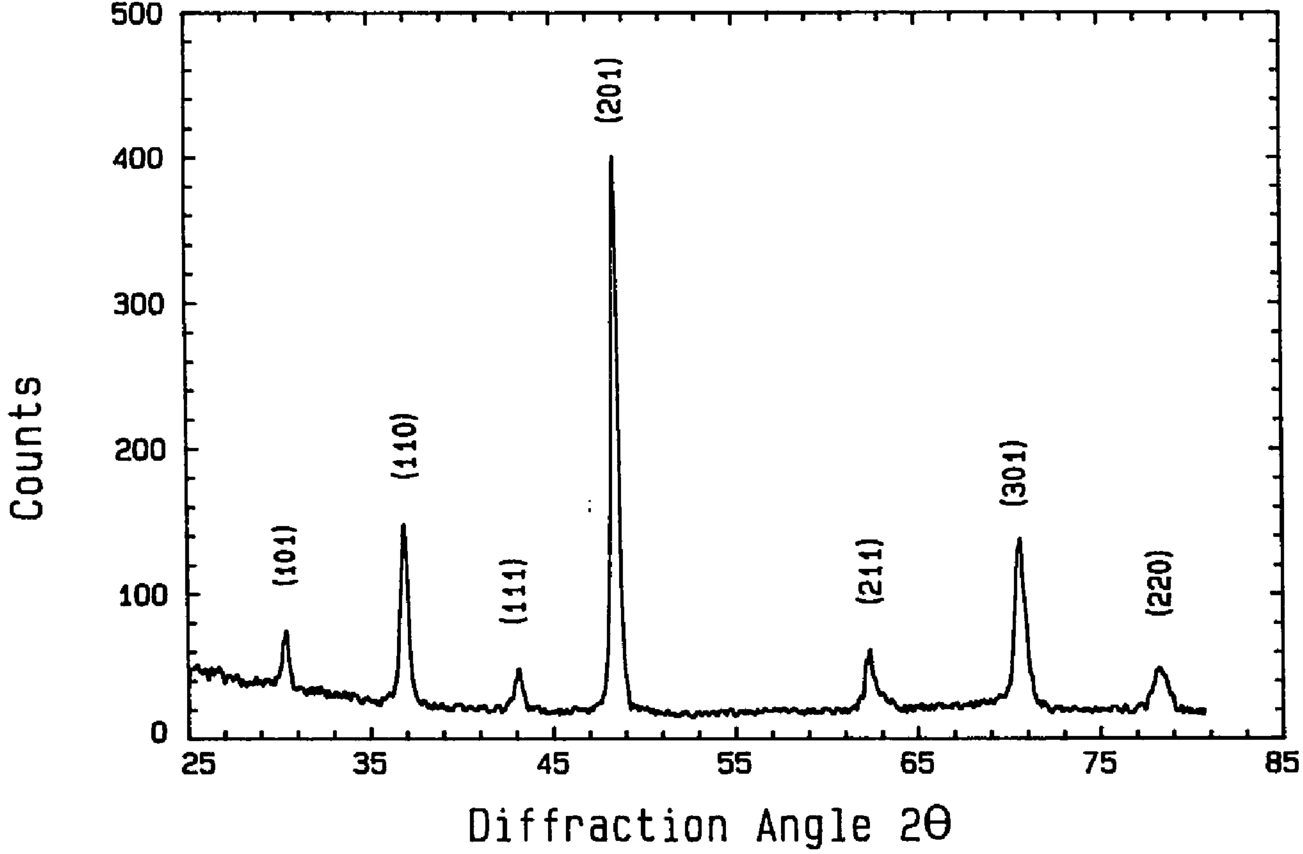

X-Ray Trace of Sample DM201

P = 45μ, 50%Ar 50%Xe, T=345 C

Figure 35

Hysteresis Loops of Sample DM201

P = 45μ, 50%Ar 50%Xe, T=345 C

$(BH)_{max}$ = 19.7 MGOe

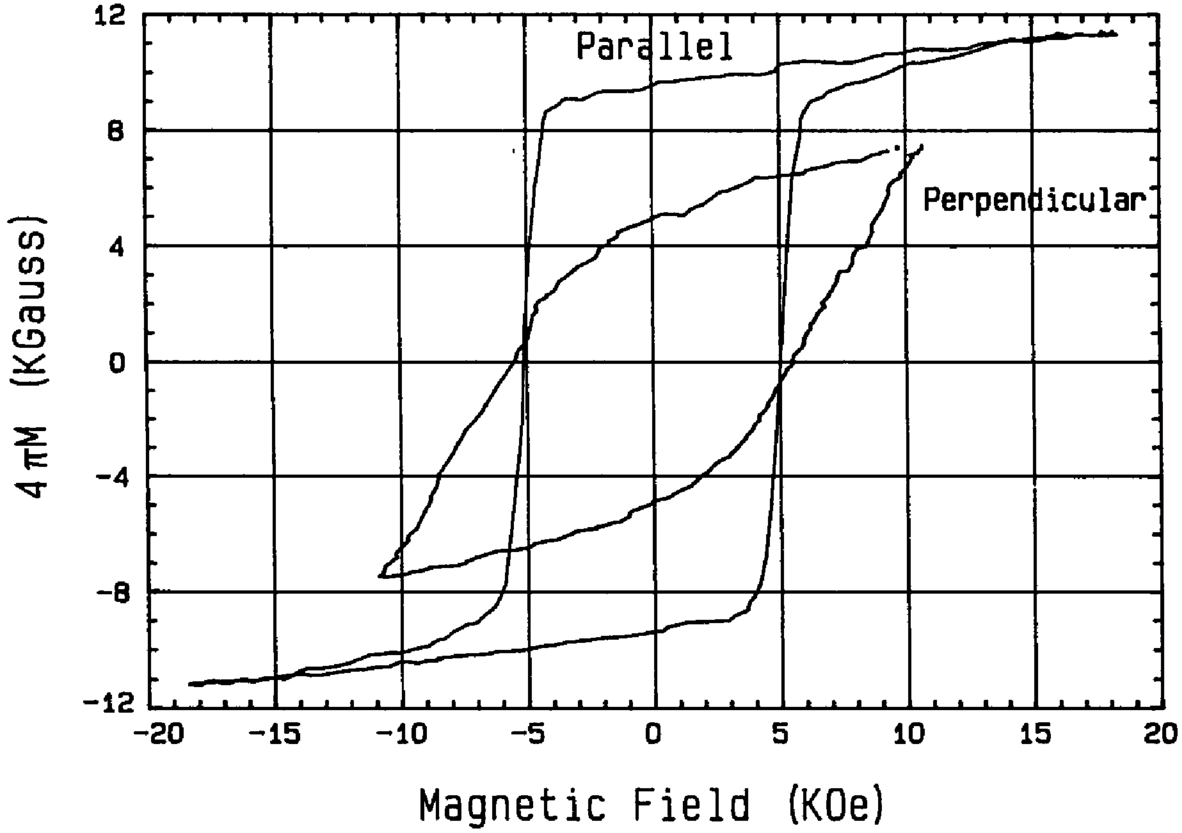

Figure 36

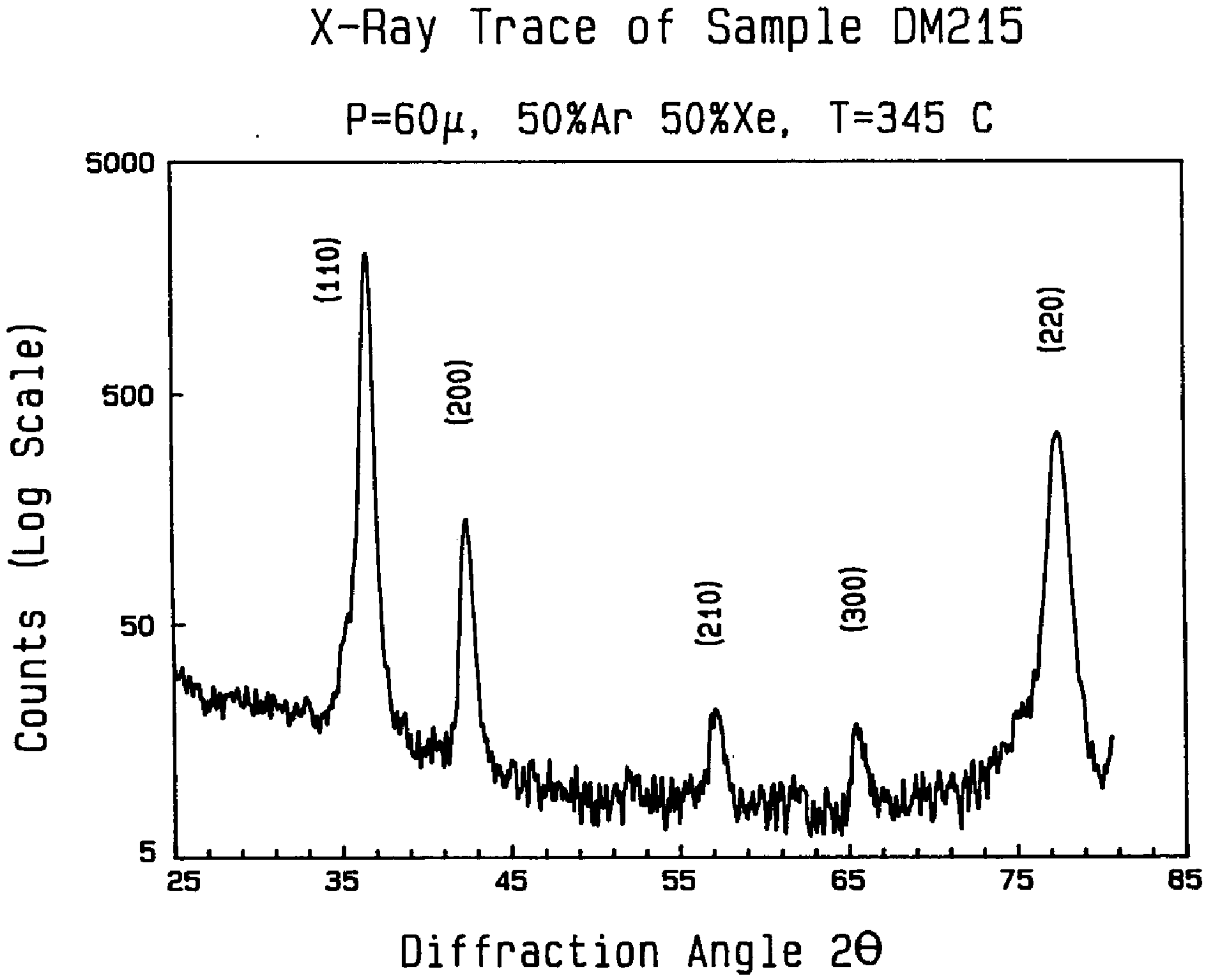
X-Ray Trace of Sample DM215
P=60μ, 50%Ar 50%Xe, T=345 C
Counts (Log Scale)
5000
500
50
5
(110)
(200)
(210)
(300)
(220)
25
35
45
55
65
75
85
Diffraction Angle 2Θ

Figure 37

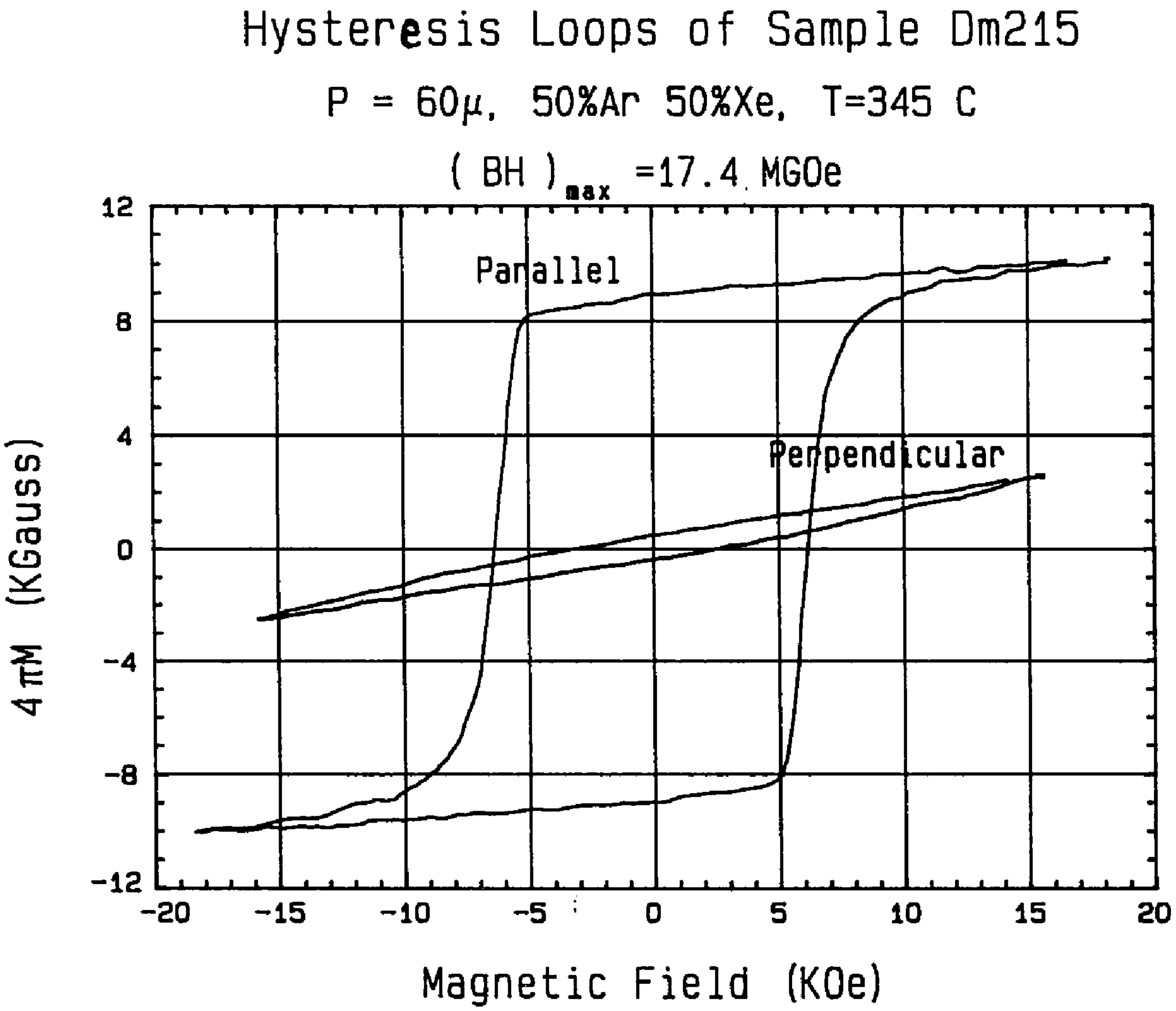

Hysteresis Loops of Sample Dm215

P = 60μ, 50%Ar 50%Xe, T=345 C

$(BH)_{max}$ =17.4 MGOe

Figure 38

Figure 39

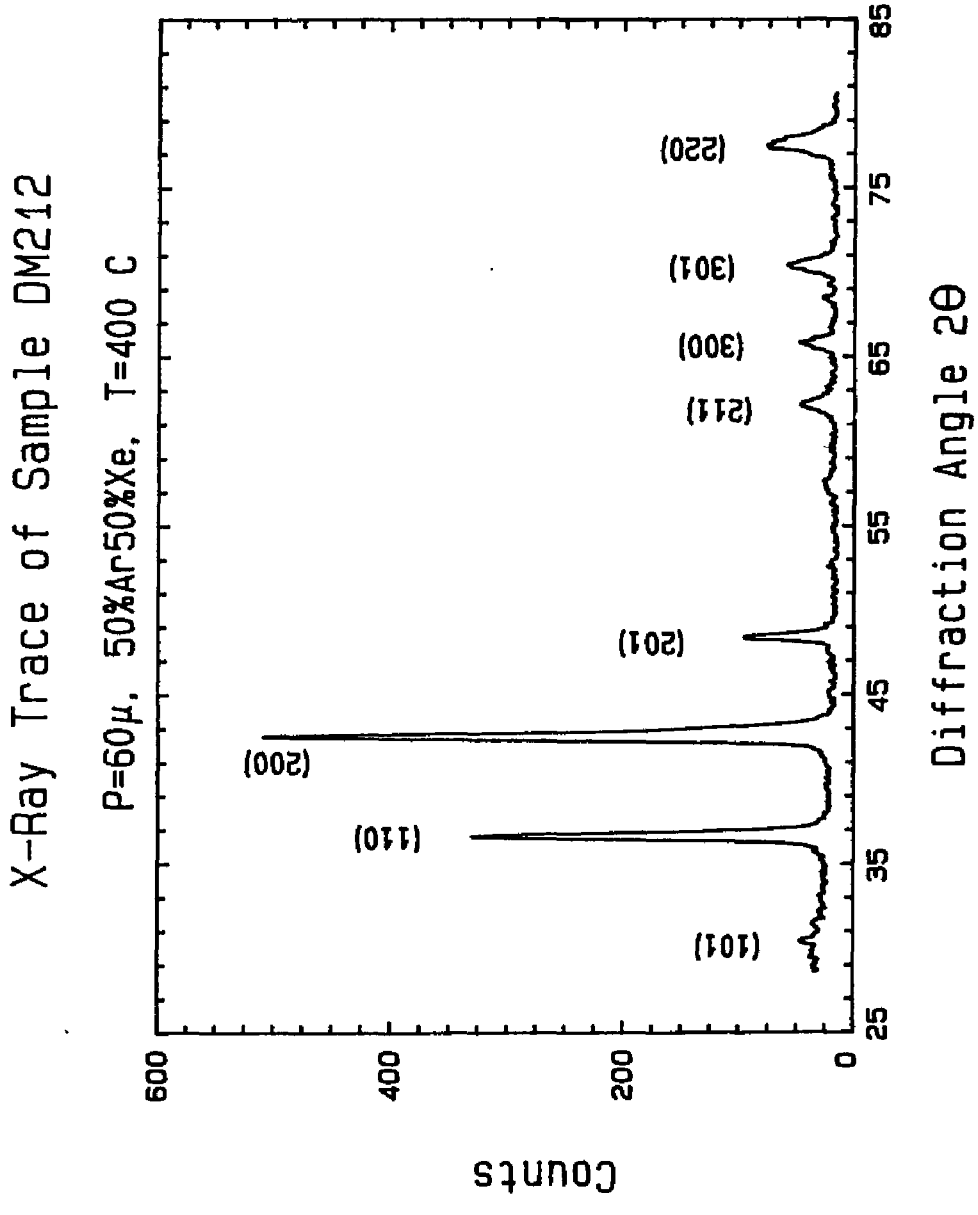
X-Ray Trace of Sample DM212
P=60μ, 50%Ar50%Xe, T=400 C
Counts
0
200
400
600
Diffraction Angle 2Θ
25
35
45
55
65
75
85
(101)
(110)
(200)
(201)
(211)
(300)
(301)
(220)

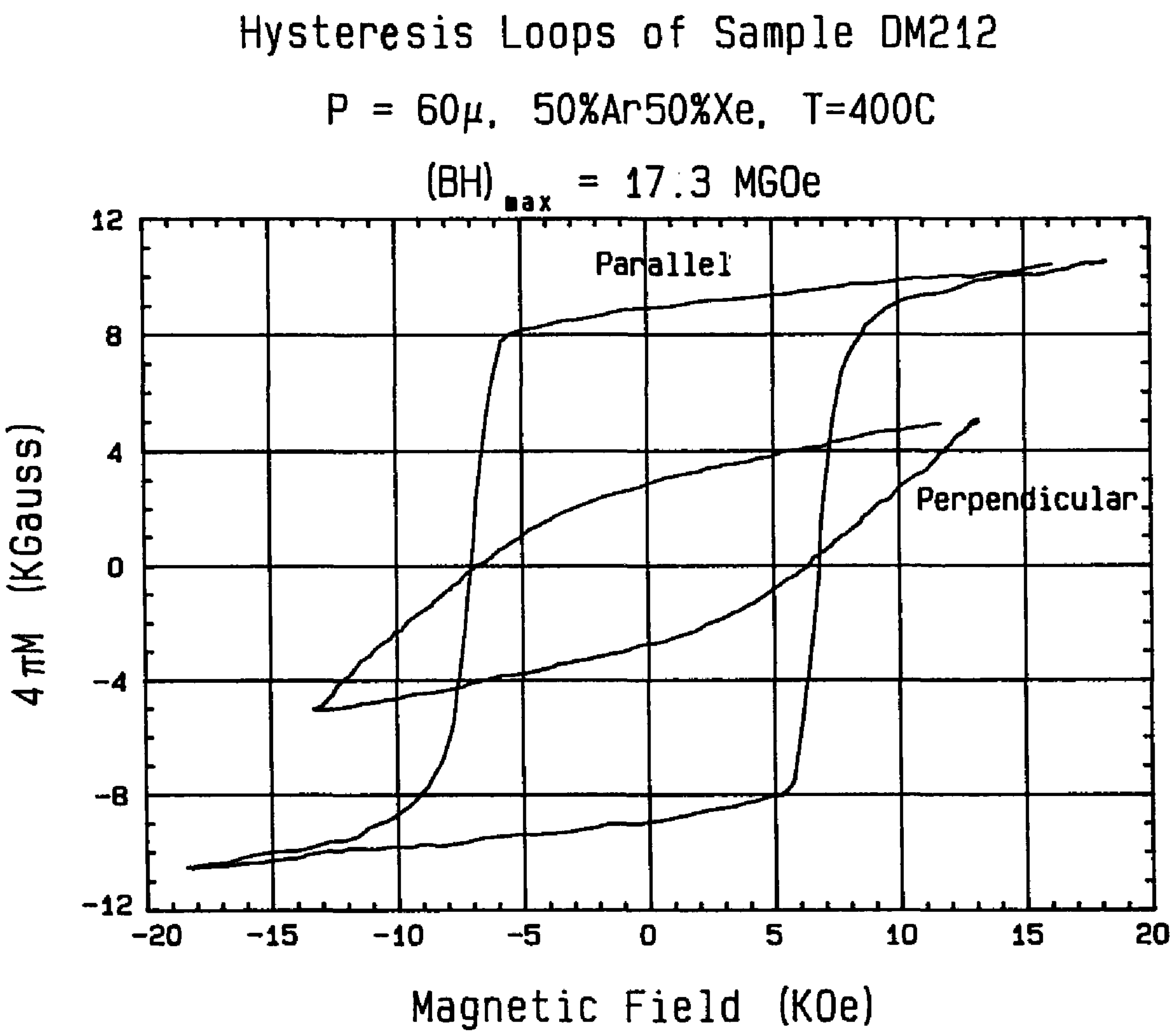
Hysteresis Loops of Sample DM212
P = 60μ, 50%Ar50%Xe, T=400C
(BH)max = 17.3 MGOe
Parallel
Perpendicular
4πM (KGauss)
12
8
4
0
-4
-8
-12
-20
-15
-10
-5
0
5
10
15
20
Magnetic Field (KOe)

Figure 40

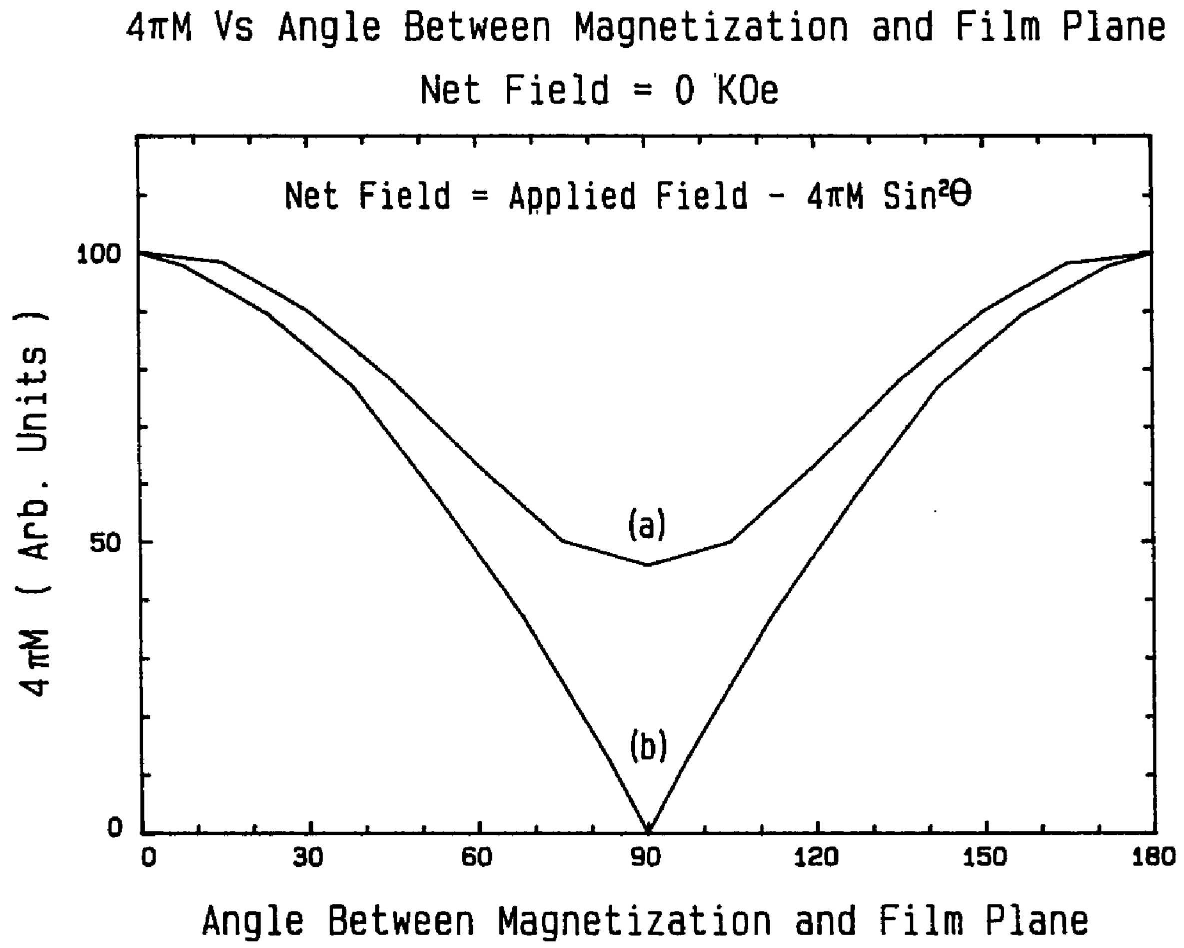

(a) Film with Partial inplane c-axes Alignment
(b) Film with Full inplane c-axes Alignment

Figure 41

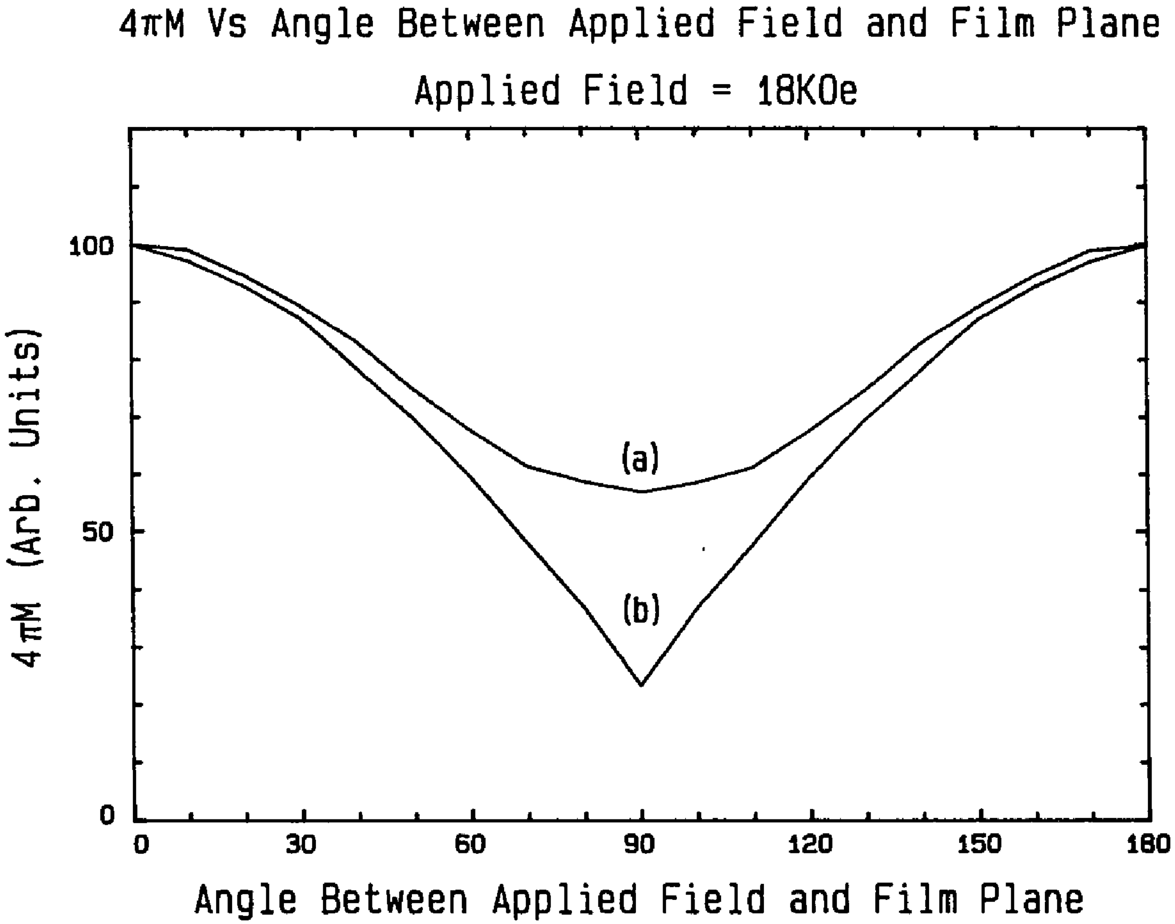

(a) Film with Partial Inplane c-axes Alignment
(b) Film with Full Inplane c-axes Alignment

Figure 42

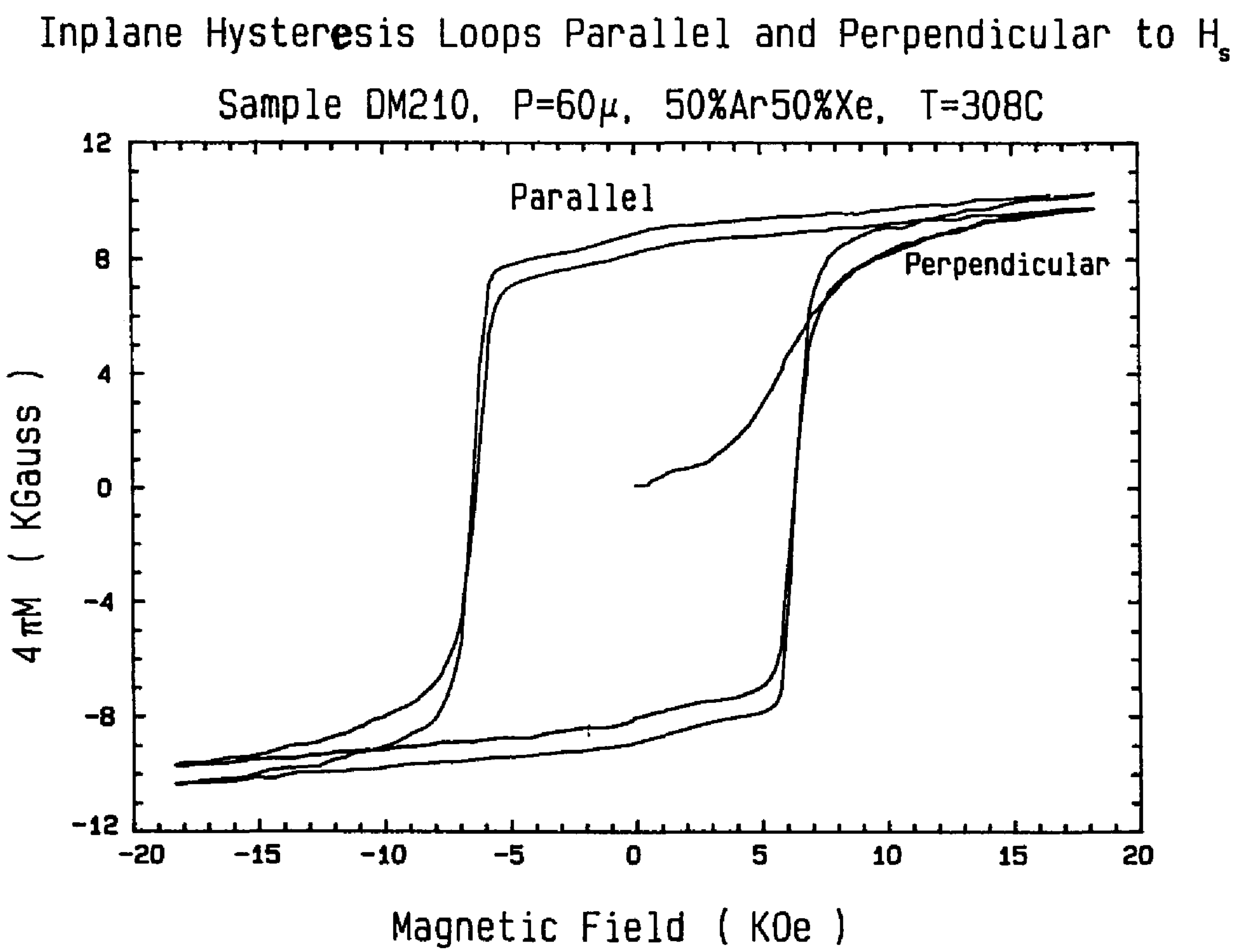

Inplane Hysteresis Loops Parallel and Perpendicular to H_s

Sample DM210, P=60μ, 50%Ar50%Xe, T=308C

Figure 43

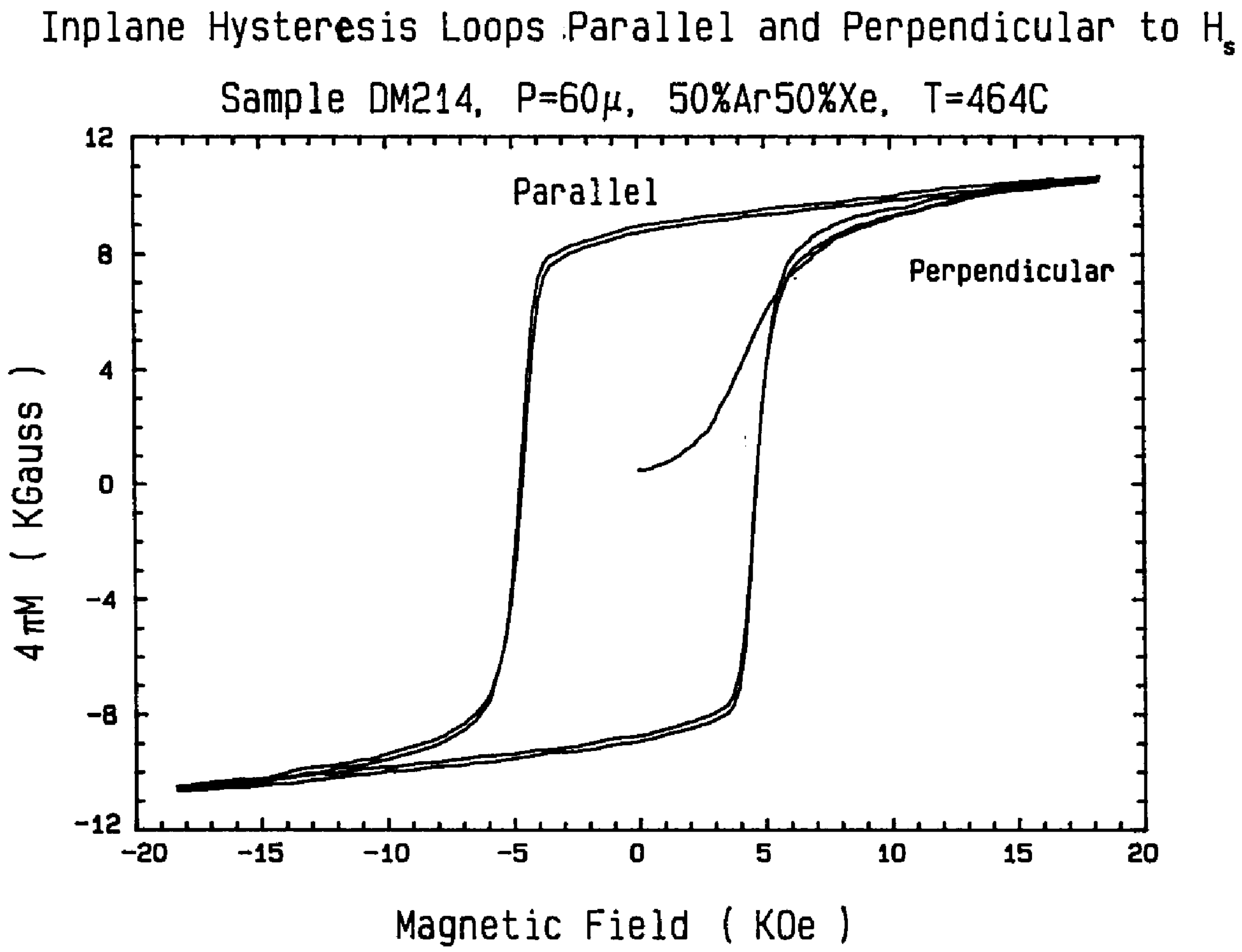

Inplane Hysteresis Loops Parallel and Perpendicular to H_s

Sample DM214, P=60μ, 50%Ar50%Xe, T=464C

Figure 44

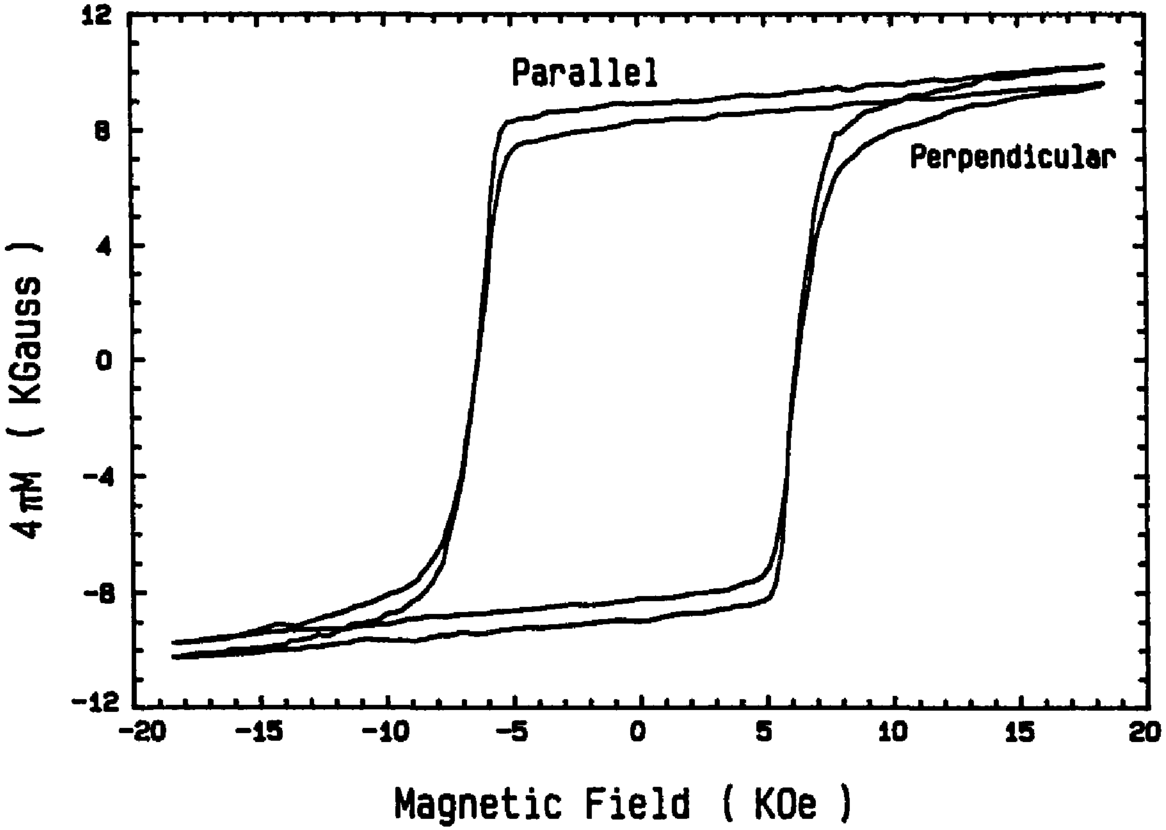

Inplane Hysteresis Loops Parallel and Perpendicular to H_s

Sample DM215, P=60μ, 50%Ar50%Xe, T=345C

Figure 45

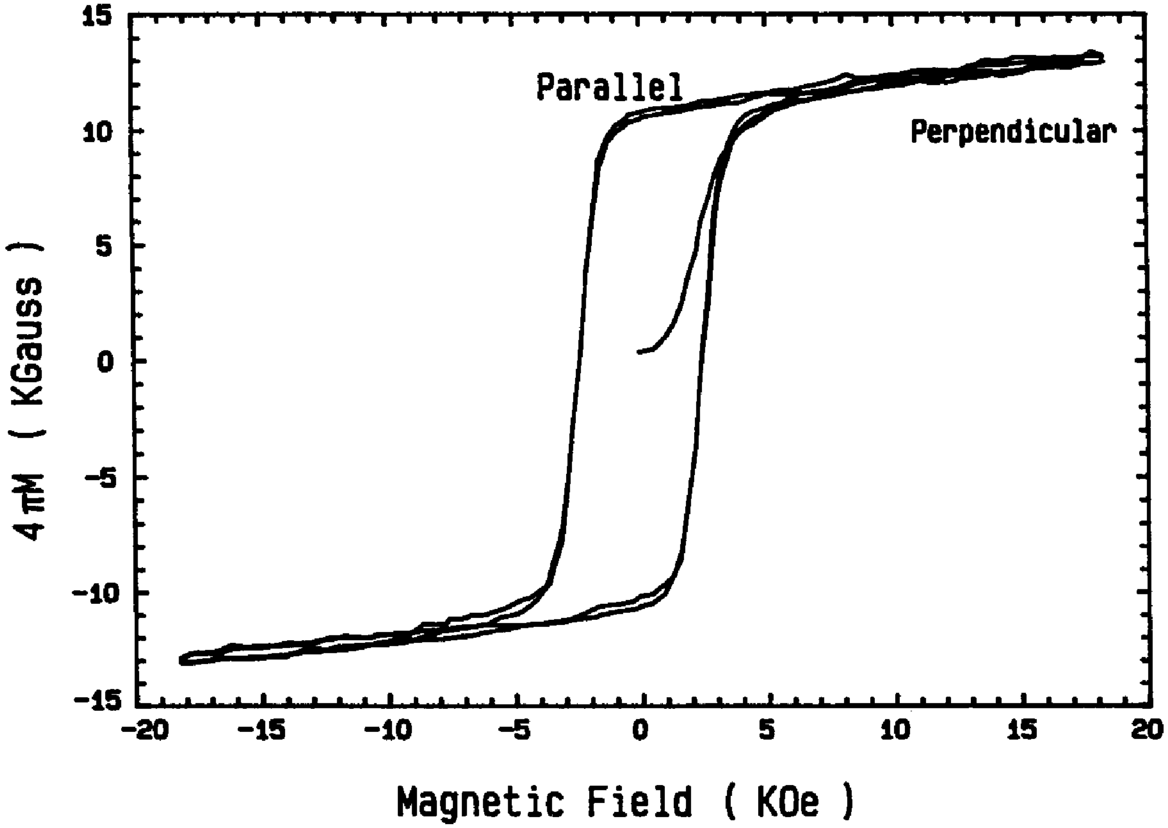
Inplane Hysteresis Loops Parallel and Perpendicular to H_s

Sample DM205, P=30μ, 50%Ar50%Xe, T=345C

Figure 46

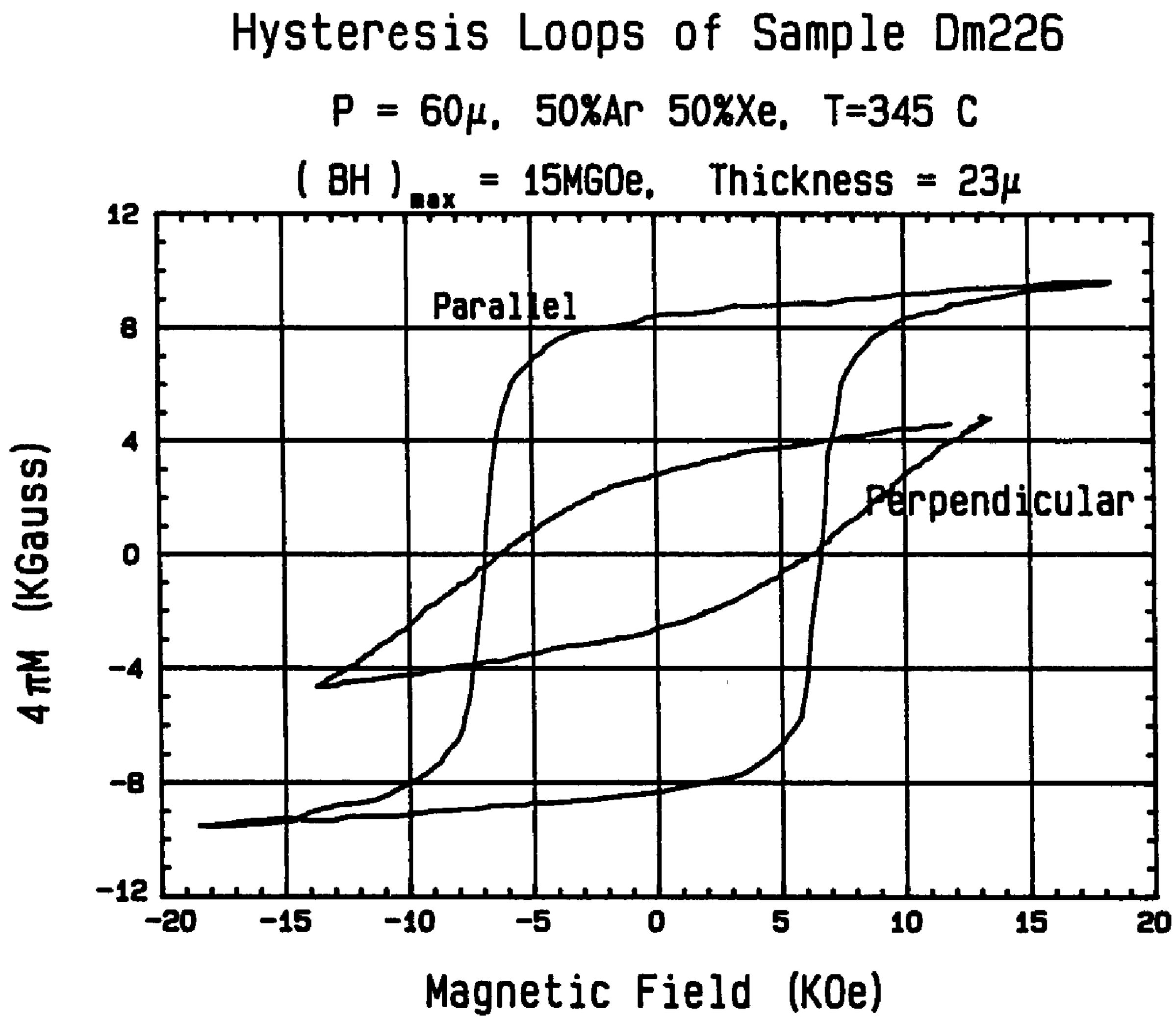
Hysteresis Loops of Sample Dm226
P = 60μ, 50%Ar 50%Xe, T=345 C
(BH)max = 15MGOe, Thickness = 23μ
Parallel
Perpendicular
12
8
4
0
-4
-8
-12
-20
-15
-10
-5
0
5
10
15
20
4πM (KGauss)
Magnetic Field (KOe)

Figure 47

REFERENCES

1. G.Hoffer and K.J.Strnat, IEEE Trans. Magn. MAG-2, 487 (1966)
2. K.J.Strnat, A.E.Ray, J.D.Livingston, and K.S.V.L.Narasimhan in Soft and Hard Magnetic Materials with Applications, Ed. by J.A.Salsgiver (ASM, Metals Park, OH, 1986)
3. F.J.Cadieu, T.D.Cheung, L.Wickramasekara, N.Kamprath, H.Hegde and N.C.Liu, J.Appl.Phys, 57, 4152 (1985)
4. F.J.Cadieu, T.D.Cheung and L.Wickramasekara, J. Appl. Phys., 57, 3598 (1985)
5. F.J.Cadieu, T.D.Cheung, L.Wickramasekara and S.H.Aly, J. Appl. Phys., 55, 2611 (1984)
6. E.Potenziani, H.A.Leupold, J.P.Clark and A.Tauber, J. Appl. Phys., 57, 4152 (1985)
7. F.J.Cadieu, J. Appl. Phys., 61, 4105 (1987)
8. F.J.Cadieu, H.Hegde and K.Chen, IEEE Trans. Magn., MAG-25, 3788 (1989)
9. F.J.Cadieu, H.Hegde and K.Chen, 34th Conf. on Magnetism and Magnetic Materials, Boston, 1989 (to be published in J. Appl. Physics)
10. F.J.Cadieu, H.Hegde and K.Chen, Presented at the 8th International Thin Film Conference, San Diego, April 1990 (to be published in J. Vac. Sci. Technol)
11. F.J.Cadieu and N.Chencinski, IEEE Trans. Magn., MAG-11, 227 (1975)
12. W.E.Wallace, Rare Earth Intermetallics (Academic, New York, 1973)
13. R.M.White and T.H.Geballe, Long Range Order in Solids (Academic, New York, 1979)
14. K.H.J.Buschow, Phys. Status Solidi, A7, 199 (1971)

15. W.B.Pearson, The Crystal Chemistry of Lattice Spacing and Physics of Metals and Alloys (Willey Interscience, New York, 1972)

16. K.H.J.Buschow and A.S.Van der Goot, J. Less-Commmon Metals, 37, 174 (1974)

17. W.E.Wallace, Prog. Rare Earth Sci. Tech., 3, 1 (1968)

18. J.J.Becker, J. Appl. Phys., 41, 1055 (1970)

19. B.Barbara, D.Gignoux, D.Givord, F.Givord and R.Lemaire, Int. J. Magn., 4, 77 (1973)

20. Szpunar and Korazeski, Phys.Status Solidi (b), 82, 449, (1977)

21. I.A.Campbell, J. Phys., F: Metal Phys., 22, 47 (1972)

22. M.J.Besnus, P.Bauer and J.M.Genin, J. Appl. Phys. F.8, 191 (1978)

23. B.D.Cullity, Introduction to Magnetic Materials (Addison-Wesley, New York, 1972)

24. A.S.Ermolenko, IEEE Trans. Magn., MAG-12, 992 (1976)

25. H.P.Klein and A.Menth, AIP Conf. Proc., 18, 1177 (1974)

26. G.Asti, F.Balzoni, D.Melville and S.Rinaldi, IEEE Trans. Magn., MAG-11, 1437 (1975)

27. J.Deportes, D.Givord, R.Lemaire, H.Nagai and Y.T.Yang, J. Less-Common Metals, 44, 273 (1976)

28. A.E.Ray and K.J.Strnat, IEEE Trans. Magn. MAG-8, 516 (1972)

29. R.Friedberg and D.I.Paul, Phys. Rev. Lett., 34, 1234 (1975)

30. B.Chapman, Glow Discharge Processes, (Wiley Interscience, 1980)

31. Thin Film Processes, Ed. by J.L.Vossen and Werner Kern (Academic Press, 1978)

32. R.W.Hoffman, Surface Interface Anal. 3, 62 (1981)

33. M.R.James and J.B.Cohen in Treatice on Material Science and Technology, Vol.19 (Academic Press , 1980)

34. S.Foner and E.J.McNiff, Rev. Sci. Instrum., 39, 171 (1968)

35. B.D.Cullity, Elements of X-Ray Diffraction, Sec. Ed. (Addison-Wesley, 1978)

36. L.S.Birks, X-Ray Spectrochemical Analysis, (Interscience Publisher, New York, 1969)

37. NBS Technical Note 1106, FRAMEC (Superintendent of Documents, U.S. Government Printing Office Washington, D.C.)

38. E.P.Bertin, Principles and Practice of X-Ray Spectrometric Analysis, Sec. Ed. (Plenum Press, 1975)

39. D.R.Beaman and J.A.Isasi, Anal. Chem., 42, 1540-68 (1970)

40. JCPDS Card Numbers: 35-1368, 19-359, 26-484, 35-1400

41. A.E.Ray, J.Appl.Phys., 55, 2094 (1984)

42. D.M.Mattox, J. Vac. Sci. Technol.A, Vol 7, 1105 (1989)

43. W.D.Westwood, J. Vac. Sci. Technol., Vol 15, 1 (1978)

44. S.M.Rossnagel, J. Vac. Sci. Technol., Vol A6, 3049 (1988)

45. T.Motohiro, J. Vac. Sci. Technol., Vol A4, 189 (1986)

46. R.S.Robinson, J.Vac.Sci. Technol., Vol 16, 185 (1979)

47. R.E.Somekh, J.Vac. Sci. Technol., Vol 2, 1285 (1984)

48. G.K.Wehner and G.S.Anderson in Handbook of Thin Film Technology, Ed. by L.I.Maissel and R.Gong (McGraw Hill, 1970)

49. P.M.Morse and H.Feshback, Methods of Theoretical Physics, Part Two (McGraw Hill, 1950)

50. S.M.Rossnagel, J. Vac. Sci. Technol.A, Vol 6, 19 (1988)

51. S.M.Rossnagel, J. Vac. Sci. Technol.A, Vol 7, 1025 (1989)

52. M.Gronau, H.Goeke and S.Methfessel, Proc. 4th Int. Conf. on Rapidly Quenched Metals (Sendai, 1981)

53. S.Chikazumi, Physics of Magnetism (John Wiley & Sons, 1964)

54. N.Kamprath, X.R.Qian, H.Hegde and F.J.Cadieu, 34th Conf. on Magnetism and Magnetic Material, Boston, 1989 (to be published in J. Appl. Phys.)

55. J.J.Becker, J. Appl. Phys. 42, 1537 (1971)

56. F.J.Cadieu, T.D.Cheung and L.Wickramasekara, J.Magn. Magn. Mater. 54-57, 535 (1986)

57. M.Sagawa, S.Fujimura, M.Togawa, H.Yamamoto and Y.Matsura, J. Appl. Phys., 55, 2883 (1984)

58. S.Liu and A.E.Ray, IEEE Trans. Magn. MAG-25 (1989)